Physics-Based Flame Dynamics Modeling and Thermoacoustic Instability Mitigation

by

Hürrem Murat Altay

B.S., Middle East Technical University (2003)
S.M., Massachusetts Institute of Technology (2005)

Submitted to the Department of Mechanical Engineering
in partial fulfillment of the requirements for the degree of

Doctor of Philosophy in Mechanical Engineering

at the

MASSACHUSETTS INSTITUTE OF TECHNOLOGY

June 2009

Author . . . .
Department of Mechanical Engineering
May 1, 2009

Certified by . . . .
Ahmed F. Ghoniem
Ronald C. Crane (1972) Professor
Thesis Supervisor

Accepted by . . . .
David E. Hardt
Chairman, Department Committee on Graduate Theses

Physics-Based Flame Dynamics Modeling and Thermoacoustic Instability Mitigation

by

Hürrem Murat Altay

Submitted to the Department of Mechanical Engineering
on May 1, 2009, in partial fulfillment of the
requirements for the degree of
Doctor of Philosophy in Mechanical Engineering

Abstract

The objectives of this work are (i) to investigate the coupled unsteady heat release mechanisms responsible for thermoacoustic instabilities under different flame anchoring configurations, (ii) to develop reduced-order models to predict the dynamic flame response, and (iii) to develop passive instability mitigation strategies by modifying the dynamics of the flame anchoring zone. The two different anchoring configurations investigated were the wake-stabilized flames and the perforated-plate stabilized flames. In order to investigate the wake-stabilized flames, experiments were performed in an atmospheric pressure, backward-facing step combustor. In this configuration, the dynamics are primarily governed by the flame-vortex interactions, whereas the equivalence ratio oscillations have minor impacts. Depending on the equivalence ratio, inlet temperature and the fuel composition, the combustor operates under different dynamic modes. The operating conditions at the transition between different modes were predicted by developing a model based on the acoustic and vortex time scales. A passive control strategy involving injection of steady air flow near the step in the cross-stream or streamwise directions were tested. Both injection configurations were able to suppress the instability under some operating conditions at which the unsteady interactions between the flame and the wake vortex were eliminated. The cross-stream air injection method eliminates these interactions by generating a new, steady recirculation zone upstream of the step. On the other hand, the streamwise air injection method eliminates these interactions by directly stabilizing the flow dynamics in the unsteady recirculation zone. In order to investigate the perforated-plate stabilized flame dynamics, a theoretical model was developed to predict the dynamic heat-release response to inlet velocity oscillations. In this configuration, the dynamics are driven by the coupled effects of the flame-wall interactions and the flame-acoustic wave interactions, generating burning velocity and flame area oscillations. The model predictions under different operating conditions were compared with the experiments and good agreement was obtained. As the heat loss to the plate increases, the plate's surface temperature rises, the flame temperature decreases, and the burning velocity oscillations become more significant. In order to verify and relax some model assumptions, two-dimensional simulations were performed in the same configuration utilizing a detailed chemical kinetic mechanism and allowing the heat transfer between the gas and the perforated-plate. The primary results of the simulations support the conclusions of the theoretical model, and show the significant impact of the heat transfer to the plate on both the steady flame characteristics, and the unsteady dynamic flame response.

Thesis Supervisor: Ahmed F. Ghoniem
Title: Ronald C. Crane (1972) Professor

Acknowledgments

It is difficult to overstate my gratitude to my advisor, Professor Ahmed Ghoniem, for his many years of support, motivation and guidance. I have benefited from his clear thinking and technical intuition, and I am grateful for his patience and trust. I would like to thank the members of my thesis committee – Dr. Anuradha Annaswamy, Professor Douglas Hart, and Professor William Green – for their insight and support. I feel privileged to have involved each of them in my thesis work.

I would like to acknowledge my colleagues: Raymond Speth, for all his practical ideas and for saving me from "any" computer related difficulties; Duane Hudgins for helping me taking most of the experimental data I present in this thesis; Kushal Kedia, for helping me develop the flame dynamics code; Fabrice Schlegel for being a good friend throughout these years; and Wonyong Lee for his constant positive attitude.

I am grateful to my wife – the love of my life – Lütfiye Bulut for her unconditional love, continuous support, motivation and understanding. Without her, none of this would have been possible.

I owe a great deal to my parents Şule - İsmail Altay, my sister Arzu, my grandfather Sabri Yahşi, and my grandaunt Nazmiye Zorba for their encouragement, and emotional and financial support. I would like to express my gratitude to Şükran Mercan for her care and love while raising me to become who I am today. I appreciate the warm family environment provided by my grandmother Feyruze Altay, my uncles Hüseyin and Osman, my aunt Safinaz and my cousins Erhan, Ömer, Dilara and Beyda during our visits to Fair Lawn, New Jersey. I will always remember my grandmother Rukiye Yahşi, who passed away during my graduate work two years ago, and my grandfather Hürrem Altay, with whom I not only share my name, but also my views, ideals and love of positive science. It gives a great honor to follow the same path he started over 60 years ago in University of Leoben, Austria.

I would also like to thank my friends Can Aras, Fatih Yiğitol, Berk Dinçman, and Murat Çetinkaya, for all the good memories and the quality time we spent together.

I dedicate this work to Mustafa Kemal Atatürk (1881-1938) – the founder of the modern, secular Turkish Republic – to whom over 70 million people owe their democratic rights and personal freedom. With this thesis, I feel honored to do my part in "advancing our country to the level of the most prosperous and the most civilized countries of the world" – his assignment to the Turkish nation during his speech on the occasion of the tenth anniversary of the republic in Ankara, on October 29th, 1933.

Mustafa Kemal Atatürk (1881–1938)

Contents

List of Figures

List of Tables

Chapter 1

Introduction

A phenomenon often observed in continuous combustion systems is self-sustained, pressure and flow oscillations forming as a result of the resonant interactions between unsteady heat release mechanisms and the acoustic modes of the system, referred to as the thermoacoustic instability [1, 2]. Thermoacoustic instability occurs under lean burn conditions, where most emissions and efficiency benefits are achieved, or near stoichiometry, where high power density is the objective. Thermoacoustic instability is undesirable since it may cause flame extinction, structural vibration, flame flashback and even structural damage. Several mechanisms appear to be present in a combustor that instigate the unsteady heat release, including: flame-acoustic wave interactions, flame-vortex interactions, equivalence ratio oscillations, flame wall interactions and unsteady stretch rate, all of which may be present individually or simultaneously [3–5], and hence promoting thermoacoustic instability. Trial-and-error methods could be used to design stable combustion systems; however, changing the design to eliminate the instability at one specific operating condition does not guarantee that the instabilities are eliminated at other operating conditions. Trial-and-error design procedure can also be costly and difficult. Physics-based combustion models that can be coupled with detailed acoustic models to simulate the system response under various operating conditions and combustor designs are required to achieve an optimum design while minimizing the trial-and error process; or simple cost-effective control strategies should be developed to suppress the instabilities generated at a desired operating condition.

The instability mechanisms are different for different combustion systems, depending primarily on the flame anchoring strategy. The wake-stabilized flames are typical in large-scale gas turbine combustors, where the power output is large and the flow is strongly turbulent. The flame is anchored in the recirculation zone formed downstream of a sudden expansion/swirler as shown in Fig. 1-1. The most significant instability mechanisms in this configuration are flame-vortex interactions and the equivalence ratio oscillations [6, 7]: (i) *Flame-vortex interactions* – The unsteady interaction between the flame surface and the vortex formed in the wake of the recirculation zone generates significant variations in the flame area; hence the heat-release rate. The periodic heat release oscillations may couple positively with the acoustic field, leading to self-sustained acoustic oscillations [8–16]; (ii) *Equivalence ratio oscillations* – The pressure oscillations in the combustor interact with the fuel supply line, leading to noticeable oscillations in the fuel flow rate. Moreover, the velocity oscillations at the location of the fuel supply modulate the air flow rate. The combined oscillations in the fuel and the air flow rates result in equivalence ratio oscillations at the location of the fuel injector. These oscillations are convected to the flame zone, where it directly effects the burning velocity of the flame and the heat of reaction of the mixture, causing heat-release rate oscillations. If the heat-release rate oscillations couple positively with the acoustic field, self-sustained oscillations are established [17–20].

The perforated-plate stabilized flames are typical in industrial and compact household burners. In these systems several conical flames form downstream of the perforated-plate holes, connected by the planar flames formed downstream of the solid surfaces

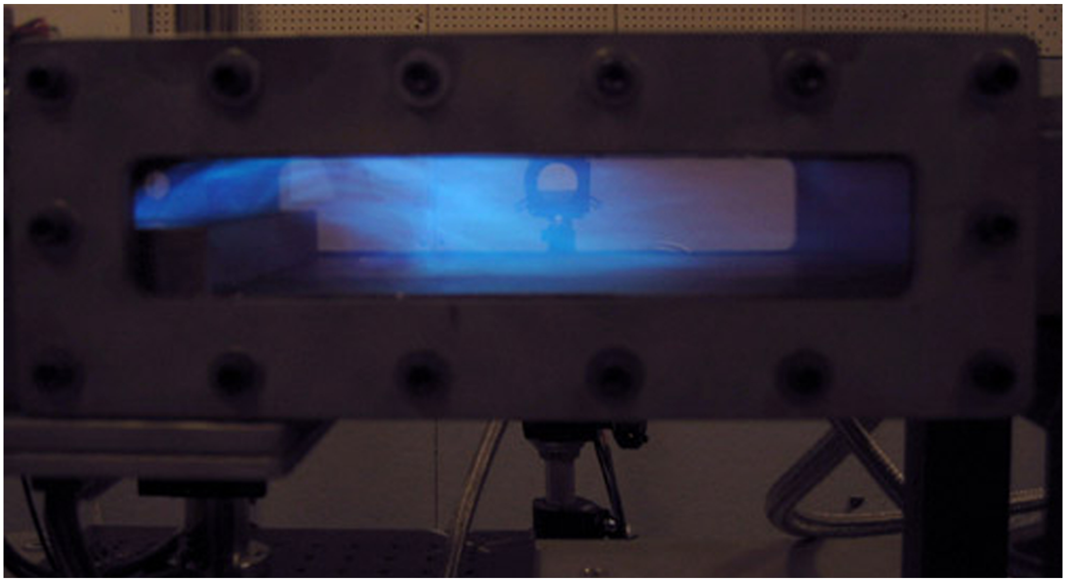

Figure 1-1: A typical wake-stabilized flame.

as shown in Fig. 1-2. The power output is typically low, and the flow is laminar. The most significant instability mechanisms are the flame-acoustic wave interactions and flame-wall interactions [4, 21, 22]: (i) *Flame-acoustic wave interactions* – The flow and pressure oscillations cause the flame surface area and the flame consumption speed to fluctuate, generating heat-release rate oscillations, which might yield to thermoacoustic instabilities, i.e. acoustic wave amplification, if couple positively with the acoustic field [23–25]. The acoustic wave amplification induced by pressure sensitivity of the flame consumption speed is weak. On the other hand, the acoustic wave amplification induced by the flow perturbations, such as through strain and curvature, are large because $u'/\bar{u} >> p'/\bar{p}$ for Low Mach number flows; (ii) *Flame-wall interactions* – When the flame propagates towards a wall, it loses heat to the wall, thus its burning velocity speed drops. When the instantaneous flow velocity exceeds the flame burning velocity, the flame starts to propagate away from the wall, the heat loss decreases, thus the burning velocity increases. The unsteady flame burning velocity generates heat release fluctuations which could yield to thermoacoustic instabilities [26–30].

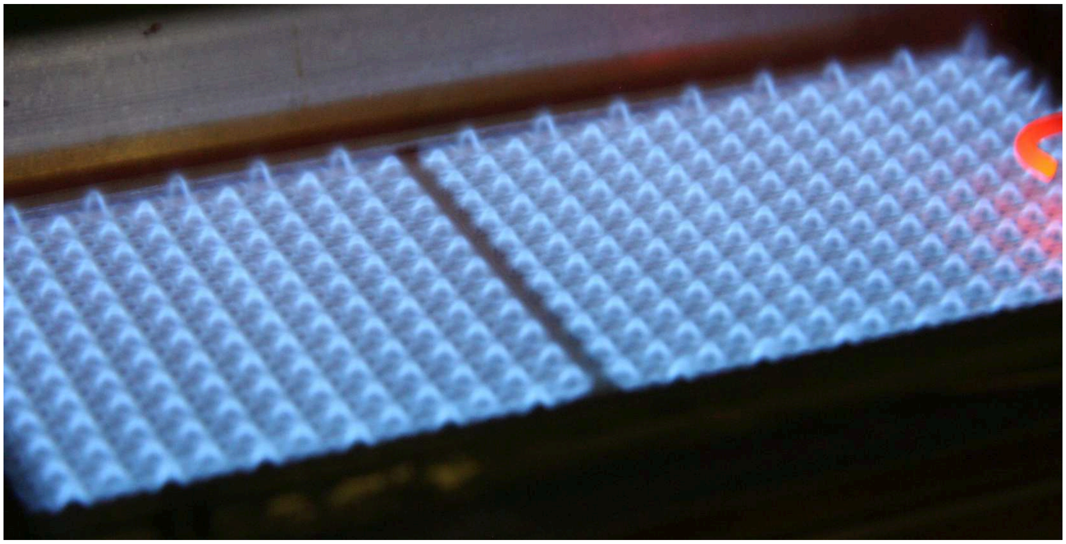

Figure 1-2: A typical perforated-plate stabilized flame.

Recently, in order to broaden the operating range of combustors, hydrogen enriched hydrocarbons have been used as fuels in lean, premixed combustors [31–34]. Hydrogen enrichment allows operation at lower flame temperature, which helps reduce NO_x emissions and the lean blowout limit of the combustor. Observed combustion dynamics and flame structures are also impacted by hydrogen enrichment as a result of its impact on the reaction kinetics. Previous research has shown that in the case of unstrained methane–air flames, hydrogen addition has a relatively small impact on the laminar burning velocity and the lean blowout limit. For methane-hydrogen mixtures with 10% fuel volume of H_2, the increase in burning velocity is typically 5%, over a range of equivalence ratios and [35]. In contrast, hydrogen enrichment has been shown to substantially increase the burning velocity and to inhibit extinction in turbulent and strained flame environments [36–38]. Analytical studies have described the impact of stretch on premixed flames, typically using asymptotic analysis and simplified models of flame structure [39–41]. These studies yield simple expressions for the variation of the burning velocity and the flame temperature from their unstretched values, emphasizing the interaction of stretch with preferential diffusion (e.g. non unity Lewis number) effects. The impact of the inlet temperature on thermoacoustic instabilities, flame structure and blowout limits have also been investigated and noticeable shifts in regions of unstable combustion have been observed [42, 43].

In this thesis, the combustion dynamics of wake-stabilized flames and perforated-plate stabilized flames are investigated in detail. The wake-stabilized flame dynamics are investigated experimentally in an atmospheric pressure, model backward-facing step combustor. I carried out a parametric study by varying the equivalence ratio, the Reynolds number, the inlet temperature, the fuel composition and the location of the fuel injector to examine the flame-vortex interactions and the equivalence ratio oscillations, and the relative contribution of these mechanisms on the dynamics. Extensive instrumentation of the combustor allows monitoring the temporal variations in pressure, heat release, and flow velocity, as well as the temporal and spatial variations in the equivalence ratio. The images of the flame captured by a high speed video camera is used to identify different operating modes. The transitions between different dynamic operating modes observed under different operating conditions are predicted by developing a simple model.

Active combustion control strategies are able to suppress thermoacoustic instabilities in premixed combustors by disrupting the coupling mechanisms that feed these instabilities by using an actuator that modulates the fuel flow rate [44–51], or air flow rate [52]. These strategies are effective in suppressing the instabilities; however, they require high cost, high speed actuators and add significant complexity to the design of the combustors. For this reason, developing simple, passive control strategies directly influencing the flame anchoring zone with minimal complexity are desirable. In this thesis, a passive control strategy by injecting steady air flow near the flame anchoring zone through choked micro-holes is proposed and tested in the backward-facing step combustor.

The perforated-plate stabilized flame response, i.e. the heat release response, to flow oscillations have been modeled extensively in the literature [28, 29]. However, these models are limited to planar flame assumption, which neglects the flame-area oscillations generated by the flame-acoustic wave interactions. As the inlet velocity increases, one needs to include the effect of the flame-area oscillations as well, because the flat flame assumption is no longer valid. In this thesis, I extend the planar perforated-plate stabilized flame models by taking into account the two-dimensionality of the flame surface formed downstream of the perforated-plate holes. The inlet velocity in the model is not limited to a maximum value unlike the planar flame models developed before, which is very important to model burners with high thermal loads. The model captures the effect of the flame-area fluctuations in addition to the flame-wall interactions. The derived heat release-inlet velocity transfer function is compared to the experimental measurements. Finally, two-dimensional reactive flame simulations utilizing a detailed chemical kinetic mechanism are performed to gain more insight on the impact of the operating conditions and the perforated-plate design on the steady flame structure and characteristics, and the dynamic flame response to inlet velocity oscillations.

In Chapters 2–4, the backward-facing step stabilized flame dynamics and in Chapters 5 and 6, the perforated-plate stabilized flame dynamics are investigated. Chapter 2 investigates the flame-vortex interaction driven combustion dynamics by eliminating the equivalence ratio oscillations arriving at the flame zone. In Chapter 3, the equivalence ratio arriving at the flame zone is no longer steady; therefore, the impact of the equivalence ratio oscillations on the flame-vortex interactions are determined. Chapter 4 investigates the passive control approach utilizing steady air injection near the flame anchoring zone. In Chapter 5, the physics-based model predicting the heat release-inlet velocity transfer function in perforated-plate stabilized flames is derived and verified experimentally. Chapter 6, explains the two-dimensional numerical model and investigates the flame structure and characteristics under steady conditions, and the dynamic response of the flame under unsteady (forced inlet flow) conditions. The conclusions are stated in Chapter 7.

Chapter 2

Flame-Vortex Interaction Driven Combustion Dynamics

In this chapter, the flame-vortex interaction driven combustion dynamics of propane-hydrogen mixtures are investigated in an atmospheric pressure, lean, premixed backward-facing step combustor. I systematically vary the equivalence ratio, inlet temperature and fuel composition to determine the stability map of the combustor. Simultaneous pressure, velocity, heat-release rate and equivalence ratio measurements and high-speed video from the experiments are used to identify and characterize several distinct operating modes. When the fuel is injected far upstream from the step, the equivalence ratio entering the flame is temporally and spatially uniform, and the combustion dynamics are governed only by the flame-vortex interactions.

The experiments are performed at Reynolds numbers of 6500 and 8500 based on the step height and mean flow velocity using pure propane or propane enriched with hydrogen by adding 30% by volume (2.0% by mass; 4.8% by LHV) or 50% by volume (4.4% by mass; 10.6% by LHV) hydrogen. The temperature of the inlet mixture is varied from ambient (300 K) to 600 K, in 100 K increments. At each fuel composition, Reynolds number and the inlet temperature, the equivalence ratio of the fuel-air mixture is varied from near the lean blowout limit to a value approaching the flashback limit near stoichiometry. I conducted the experiments with the fuel injector located 93 cm upstream of the step, which ensures that the equivalence ratio reaching the combustion zone is temporally and spatially uniform.

I demonstrate the presence of different regimes in which the flame is impacted by different flow structures depending on the operating parameters. The response curves of the combustor—the pressure amplitude as function of the equivalence ratio—are presented for a range of fuel compositions and inlet temperatures. I use numerical results to collapse the response curves, showing that the transitions between the combustor dynamic modes are correlated with changes in a heat release parameter, which incorporates the effect of strained flame consumption speed and volumetric expansion. The complex interactions between the hydrodynamics and the flames under different operating conditions can approximately be captured using the heat release parameter alone. Formulating a simple theory, the critical values of this parameter at which transitions between different dynamic operating modes take place are determined.

2.1 Combustor Description

Figure 2-1 shows a schematic diagram of the backward-facing step combustor. The combustor consists of a rectangular stainless steel duct with a cross section 40 mm high and 160 mm wide. The air inlet to the combustor is choked. At a location 0.45 m downstream from the choke plate, a 0.15 m long ramp contracts the channel height from 40 mm to 20 mm followed by a 0.4 m long constant area section that ends with a sudden expansion back to 40 mm. The step height is 20 mm. The overall length of the combustor is 5.0 m. A circular exhaust pipe comprises the last 3.0 m of the combustor with a cross sectional area approximately four times

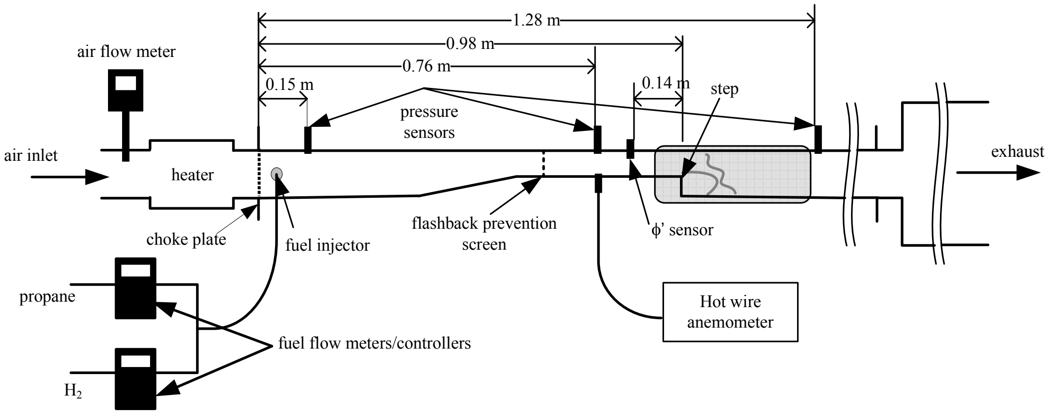

Figure 2-1: Schematic diagram of the backward-facing step combustor.

that of the rectangular section. The exhaust exits to a trench with a large cross sectional area. The combustor is equipped with quartz viewing windows. An air compressor supplies air up to 110 g/s at 883 kPa. A pair of Sierra C100M mass flow controllers allow arbitrary propane/hydrogen mixtures at maximum flow rates of 2.36 g/s for propane and 0.30 g/s for hydrogen. The uncertainty of the flow rates is ±1% of the full scale. Fuel is injected through several spanwise holes in a manifold located 93 cm upstream of the step. Images of the flame are captured at 2000 frames per second using a Phantom v7.1 high-speed camera. Pressure measurements are obtained using Kulite MIC-093 high intensity microphones designed for laboratory investigations. Flow velocity is measured using TSI IFA300 hot wire anemometer. An optical bandpass filter centered at 430 nm is placed in front of a Hamamatsu H9306-02 photosensor module to measure the CH* chemiluminescence emitted by the flame, which is proportional to the instantaneous heat-release rate [53, 54]. More details on CH* chemiluminescence measurement technique can be found in Ref. [55]. Temporal equivalence ratio variations are measured 14 cm upstream of the step using a Hamamatsu P4245 photodiode to detect absorption of a HeNe laser by propane at a wavelength of 3.39 μm. This laser is modulated using a Scitec Instruments 360 OEM optical chopper in order to distinguish between the light emitted by the flame when it flashes back and the laser signal. When the fuel passes through the laser beam, it absorbs some of the laser light, reducing the photodiode signal. The intensity of the light can be related to the fuel concentration using the Beer-Lambert law, as described by Lee et al. in Ref. [18]. Figure 2-2 shows the schematic diagram of the temporal equivalence ratio measurement setup. The spatial concentration/equivalence ratio measurements are performed under non-reacting flow conditions by injecting CO_2 into the combustor as a fuel surrogate and taking point measurements of its concentration using a California Analytical Instruments ZRH CO/CO_2 analyzer. The gas probe automatically traverses the combustor cross section near the location of the step. The spatial concentration measurement setup is shown schematically in Fig. 2-3. The inlet mixture temperature is set using an Osram Sylvania 18 kW inline electric heater with on/off temperature controller. All data are acquired using a National Instruments PCIe-6259 data acquisition board and the Matlab Data Acquisition Toolbox. A custom Matlab code is used to store the data and control the experiment.

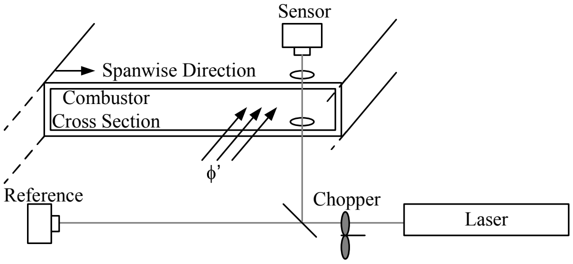

Figure 2-2: Schematic diagram showing the temporal equivalence ratio measurement setup.

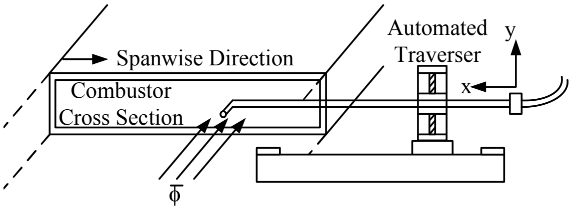

Figure 2-3: Schematic diagram showing the spatial equivalence ratio measurement setup.

2.2 Results

Temporal oscillations of the equivalence ratio, and non-uniformities in the equivalence ratio distribution entering the flame zone can significantly impact the combustion dynamics by impacting the local burning velocity along the flame front as well as the flame structure. Here, because I am interested in investigating only the flame-vortex interaction driven combustion dynamics, I ensure that the equivalence ratio entering the combustion zone is steady, i.e. no temporal variations of the equivalence ratio is present at the combustion zone. Moreover, in order to achieve premixed combustion, the spatial equivalence ratio distribution entering the flame zone should be uniform.

In Fig. 2-4, I show the temporal variation of the equivalence ratio measured 14 cm upstream of the step when the combustor is fired at an equivalence ratio of 0.80 and a Reynolds number of 8500, without hydrogen enrichment, when the fuel injector is located 93 cm upstream of the step. At this location of the fuel injector no temporal variations of the equivalence ratio are observed as a result of two factors: (i) the amplitude of equivalence ratio oscillations established at the fuel injector location are small, since the injector is located near the choke plate where velocity oscillations are small and (ii) the convective time scale, $\tau = L_{inj}/\bar{U}$ is long so that there is enough time for the oscillations to be damped by turbulent mixing before reaching the combustion zone, where L_{inj} is the distance between the fuel injector and the step and $\bar{U}$ is the average flow velocity [4, 19].

Next, the spatial distribution of the equivalence ratio is measured keeping the fuel injector at the same location, under steady, non-reactive conditions using the technique described in the previous section. The measurements are performed at a cross section 2 cm downstream of the step, without hydrogen enrichment, at Re=8500 and mean equivalence ratio of 0.70. The maximum variation of the measured equivalence ratio distribution along the cross section is less than 1%. This indicates uniform spatial equivalence ratio distribution, ensuring premixed combustion.

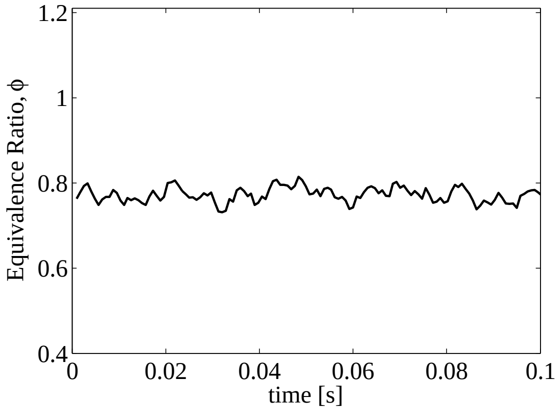

Figure 2-4: Temporal equivalence ratio measurements 14 cm upstream of the step at Re=8500, ϕ =0.80 while injecting the fuel 93 cm upstream of the step.

In the rest of this chapter, in order to investigate flame-vortex interaction driven premixed combustion dynamics, the fuel is introduced 93 cm upstream of the step as suggested by the above results. I conduct a series of experiments in order to: (i) determine the stability map; (ii) investigate the resonant acoustic modes; (iii) distinguish between the flame-vortex interaction dynamics observed under distinct operating modes. Finally, I formulate a theory supported by numerical simulations of one-dimensional, strained flames to predict the transitions between different operating modes of the combustor.

2.2.1 Stability Map

I systematically vary the inlet temperature, fuel composition and the Reynolds number, and measure the response curves of the combustor while varying the equivalence ratio between the lean blowout limit and near stoichiometry. The measured pressure fluctuations are reported in terms of the overall sound pressure level (OASPL) using the pressure sensor located 1.28 m downstream of the choke plate, which is close to the location of the flame. The OASPL in dB is defined as:

$$OASPL = 10\log_{10}\overline{\left[\frac{p(t)-\overline{p(t)}}{p_o}\right]^2} \tag{2.1}$$

where overbars indicate average values, $p(t)$ is the pressure measured in an interval $t_1 < t < t_2$ and $p_o = 2 \cdot 10^{-5}$ Pa.

While performing the tests, I observed that the combustor dynamics were strongly influenced by the history of the operating mode and the conditions. In order to illustrate this history dependence, I plot the OASPL as a function of equivalence ratio for propane flames at Reynolds numbers of 6500 and 8500 and the inlet temperature of 300 K in Fig. 2-5. At each Reynolds number, the equivalence ratio is either increased from the lean blowout limit towards stoichiometry, or decreased from near stoichiometry towards the lean blowout limit. When the equivalence ratio is increased from the lean blowout limit, the transitions in the response curves shown in Fig. 2-5 shift towards higher equivalence ratios at both Reynolds numbers. The dependence of the combustor dynamics on the history, i.e. the presence of hysteresis, is attributed to

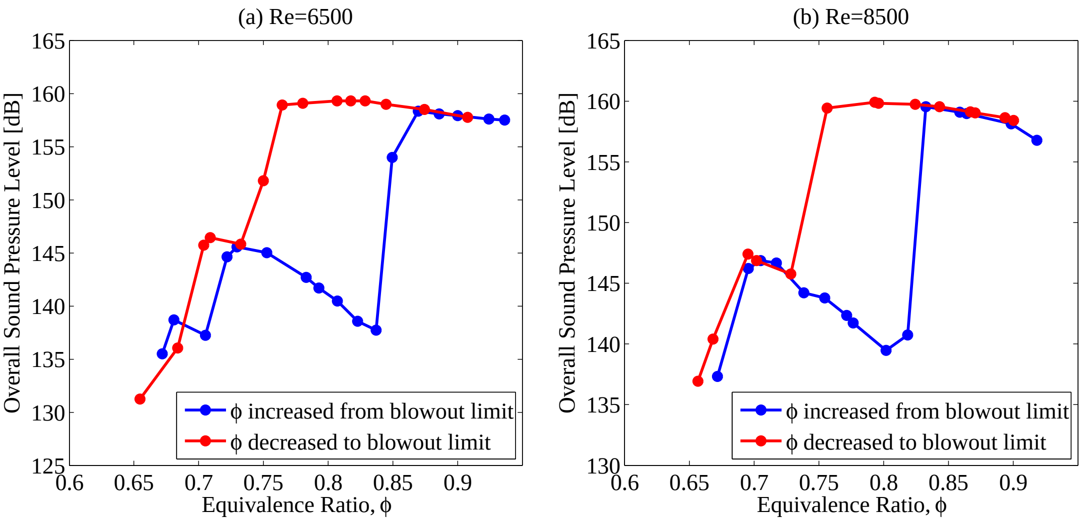

Figure 2-5: OASPL as a function of equivalence ratio without hydrogen enrichment at an inlet temperature of 300 K. The equivalence ratio is either increased from near the blowout limit towards stoichiometry, or decreased from near stoichiometry towards the lean blowout limit for: (a) Re=6500; (b) Re=8500.

the highly non-linear nature of the system. In the rest of this thesis, the data are obtained while decreasing the equivalence ratio from near stoichiometry towards the lean blowout limit.

In Fig. 2-6, I plot the OASPL as a function of the equivalence ratio using pure propane or propane enriched with 50% by volume (4.4% by mass; 10.6% by LHV) hydrogen at Reynolds numbers of 6500 and 8500, and inlet temperatures of 300 K and 500 K. When the inlet temperature is 300 K, I observed three distinct operating modes corresponding to sound pressure levels of 158–160 dB, 145–150 dB and 130–135 dB. The combustor operating modes corresponding to the 158–160 dB bands are referred to as *unstable*, 145–150 dB bands are referred to as *quasi-stable* and OASPL values between 130–135 dB close to the lean blowout are referred to as *stable*. The origin of each characterization will become apparent when I depict the flame images during the corresponding operating modes. When the inlet temperature is raised to 500 K, the OASPL in the unstable region decreases slowly with increasing equivalence ratio and suddenly jumps to much higher values as the equivalence ratio exceeds a certain

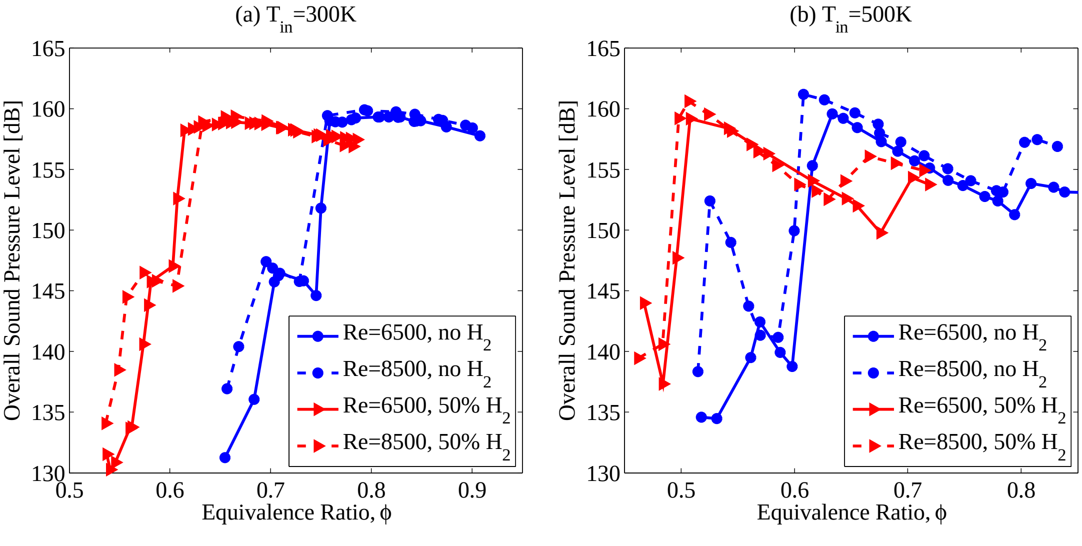

Figure 2-6: OASPL as a function of equivalence ratio using pure propane and propane enriched with 50% by volume hydrogen at Re=6500 and Re=8500 at an inlet temperature of (a) T_{in}=300 K; (b) T_{in}=500 K.

threshold (0.80 without hydrogen enrichment at both Reynolds numbers). This is the *high-frequency unstable* mode, where a higher acoustic mode of the combustor is excited. The impact of the Reynolds number on the stability map is minor. The quasi-stable mode is wider when the Reynolds number is 8500, especially at inlet temperature of 500 K. Enriching propane with hydrogen or increasing the temperature of the inlet mixture lower the lean blowout limit and shift the observed transitions between operating modes to lower equivalence ratios.

I investigate the results in Fig. 2-6 in more detail by showing the combustor's frequency response in Figs. 2-7 and 2-8 for the cases corresponding to Fig. 2-6(a) and Fig. 2-6(b), respectively. These figures show the amplitude of pressure oscillations as a function of the frequency for the ranges of equivalence ratios in Fig. 2-6.

Figure 2-7(a) shows the frequency response for Reynolds number of 6500, inlet temperature of 300 K, without hydrogen enrichment. As the equivalence ratio is dropped from 0.90 to 0.70, the acoustic mode around 40 Hz is excited and the combustor operates in the unstable mode. As the equivalence ratio is reduced just below 0.70, there is a slight increase in the resonant frequency, and a transition to the quasi-stable operating mode. The resonant frequency drops slowly, as the equivalence ratio is decreased further until the lean blowout limit. Similar acoustic response is observed in Fig. 2-7(b), which shows the frequency response for Reynolds number of 8500, inlet temperature of 300 K, without hydrogen enrichment. However, at this Reynolds number, the transition to the quasi-stable mode occurs around the equivalence ratio of 0.73, which is slightly higher than that in the Re=6500 case. When 50% by volume hydrogen is added to propane, the transition to quasi-stable mode occurs at an equivalence ratio of 0.62 at both Reynolds numbers, as shown in Figs. 2-7(c) and 2-7(d). When the inlet temperature is 300 K, only the resonant mode around 40 Hz is dominant for the unstable and the quasi-stable operating modes of the combustor.

When the inlet temperature is raised to 500 K, there are significant changes in the

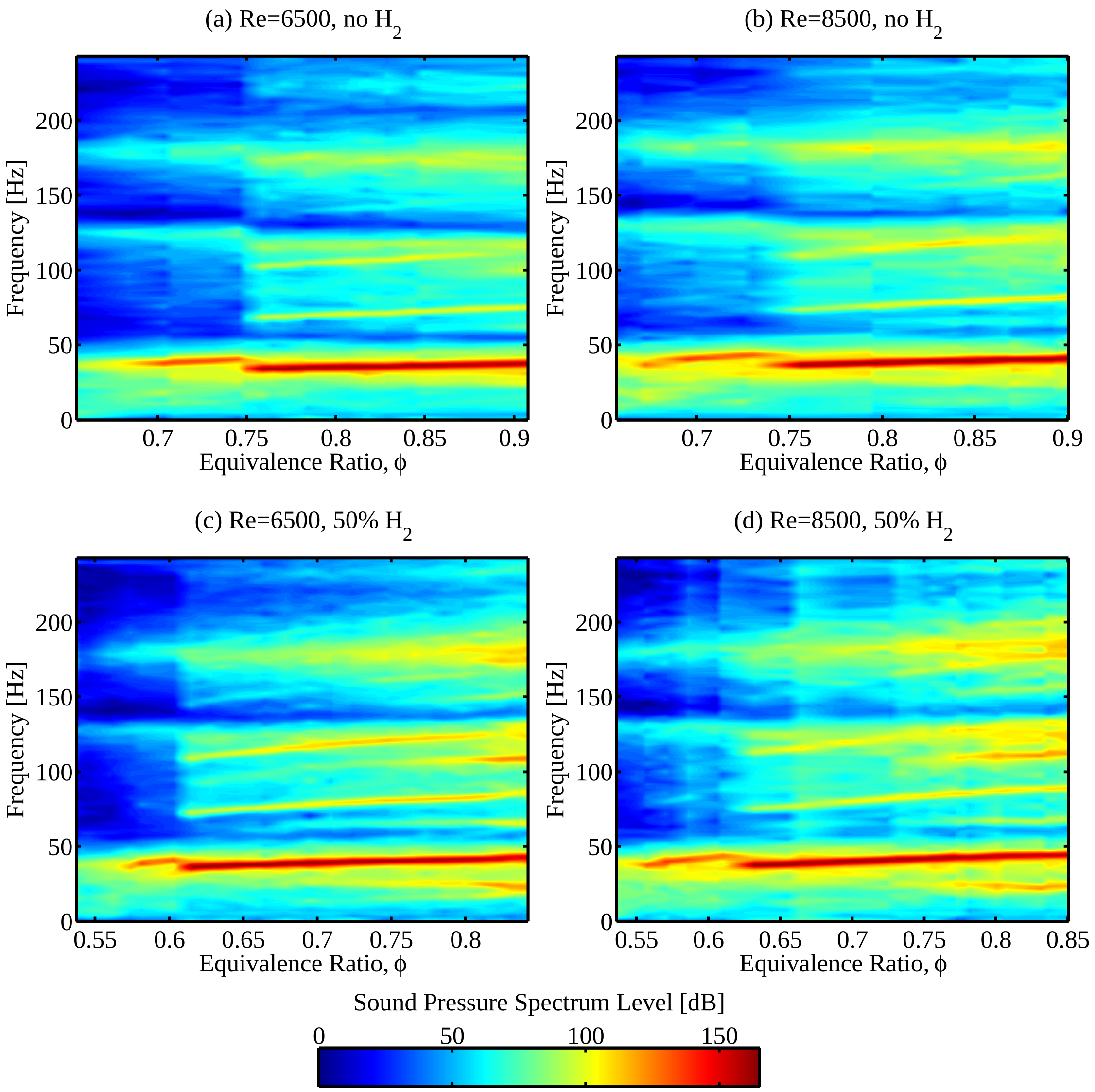

Figure 2-7: Sound pressure spectrum level maps as a function of equivalence ratio at inlet temperature of 300 K for (a) Re=6500, no H_2 enrichment; (b) Re=8500, no H_2 enrichment; (c) Re=6500, 50% by volume H_2 enrichment; (d) Re=8500, 50% by volume H_2 enrichment.

acoustic response of the combustor as shown in Fig. 2-8. Without hydrogen addition, at both Reynolds numbers, as the equivalence ratio drops below 0.85, the combustor resonates around 130 Hz, until the equivalence ratio reaches 0.80, as shown in Figs. 2-8(a) and 2-8(b). These operating bands correspond to OASPLs of 153 dB and 158 dB for Re=6500 and Re=8500, respectively, in Fig. 2-6(b), and are referred to as the high-frequency unstable mode. As the equivalence ratio is reduced further, the 40 Hz band

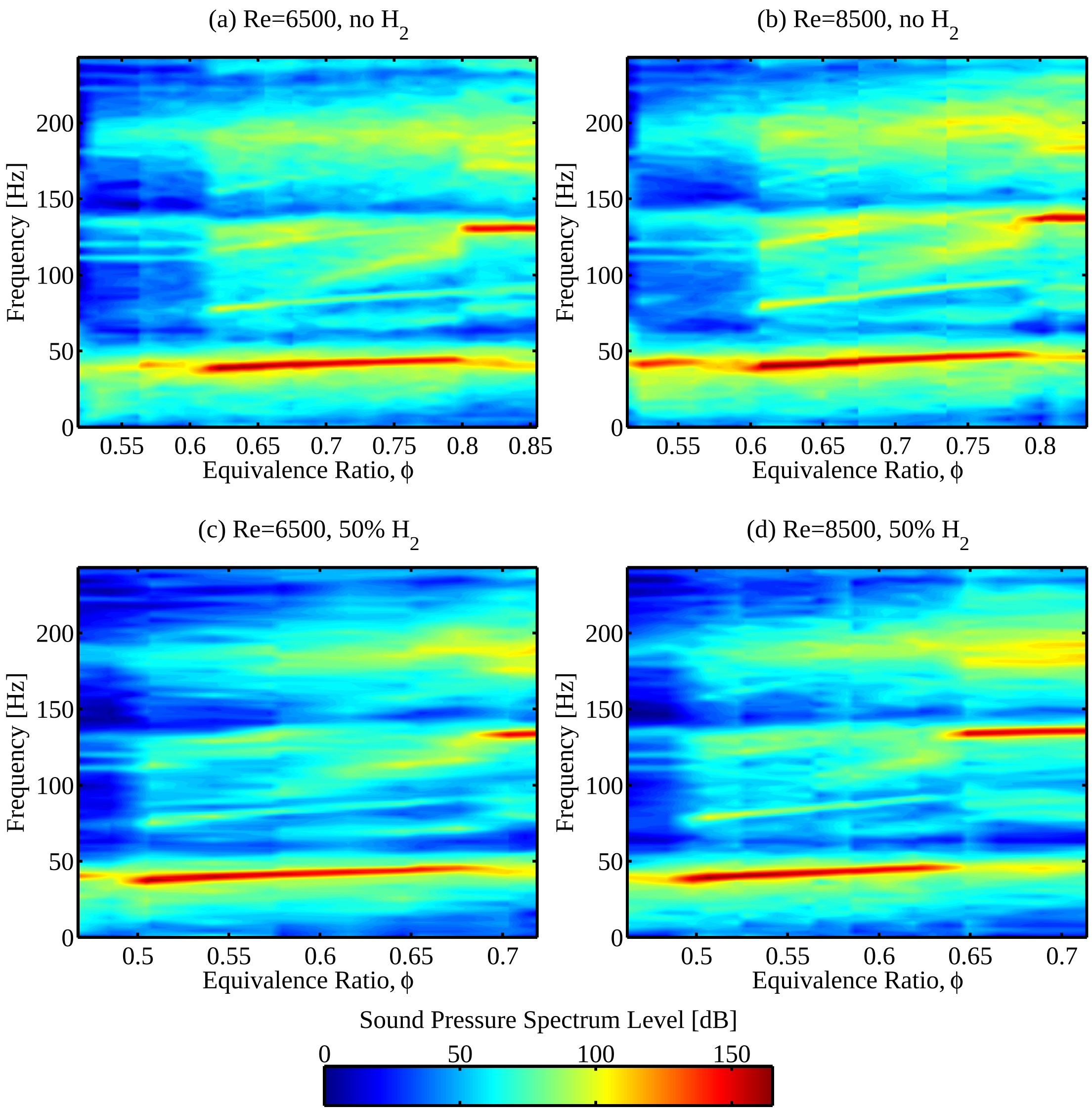

Figure 2-8: Sound pressure spectrum level maps as a function of equivalence ratio at inlet temperature of 500 K for (a) Re=6500, no H_2 enrichment; (b) Re=8500, no H_2 enrichment; (c) Re=6500, 50% by volume H_2 enrichment; (d) Re=8500, 50% by volume H_2 enrichment.

is excited until blowout occurs. However, near ϕ=0.60, at both Reynolds numbers, the OASPL drops significantly, corresponding to the transition from an unstable to a quasi-stable band. The OASPL increases until the equivalence ratio reaches 0.57 for Re=6500 and 0.52 for Re=8500. When 50% by volume hydrogen is added to propane, as the equivalence ratio is reduced from 0.72, the combustor resonates at 130 Hz until the OASPL reaches its local minimum around equivalence ratios of 0.68

for Re=6500 and 0.65 for Re=8500, as shown in Fig. 2-6(b). As the equivalence ratio is reduced further, the 40 Hz band is excited until the combustor shifts from unstable to quasi-stable operating mode around equivalence ratio of 0.49 at both Reynolds numbers.

So far I have demonstrated that changing the hydrogen content in the fuel and the inlet temperature affect the response curves significantly. Changing the Reynolds number has a minor impact. I investigate the impact of hydrogen enrichment and the inlet temperature further by extending the parameter set to include two additional inlet temperatures and one additional hydrogen concentration. In Fig. 2-9, I plot the OASPL as a function of the equivalence ratio at Reynolds number of 6500 for different fuel compositions and inlet temperatures. Figure 2-9 shows that at all inlet temperatures, increasing the hydrogen fraction in the fuel shifts the response curves towards leaner equivalence ratios. Increasing the inlet temperature at constant fuel composition has the same impact on the response curves. With preheating, the OASPL drops as the equivalence ratio increases until the high-frequency unstable mode is excited, as shown in Figs. 2-9(c) and 2-9(d). At the local minimum, which is the transition point between the unstable and the high-frequency unstable modes, the combustor operates in the quasi-stable mode when the inlet temperature is 600 K. Moreover, the distinct quasi-stable band disappears at this inlet temperature. Preheating the inlet mixture allows the excitation of higher frequency modes, impacting the combustion dynamics significantly.

2.2.2 Combustor Acoustics

In the previous section, I showed that two different acoustic modes of the combustor, corresponding to frequencies of 40 Hz and 130 Hz, were excited under different operating conditions. In this section the combustor acoustics are investigated in detail to explain the origin of the observed resonant frequencies.

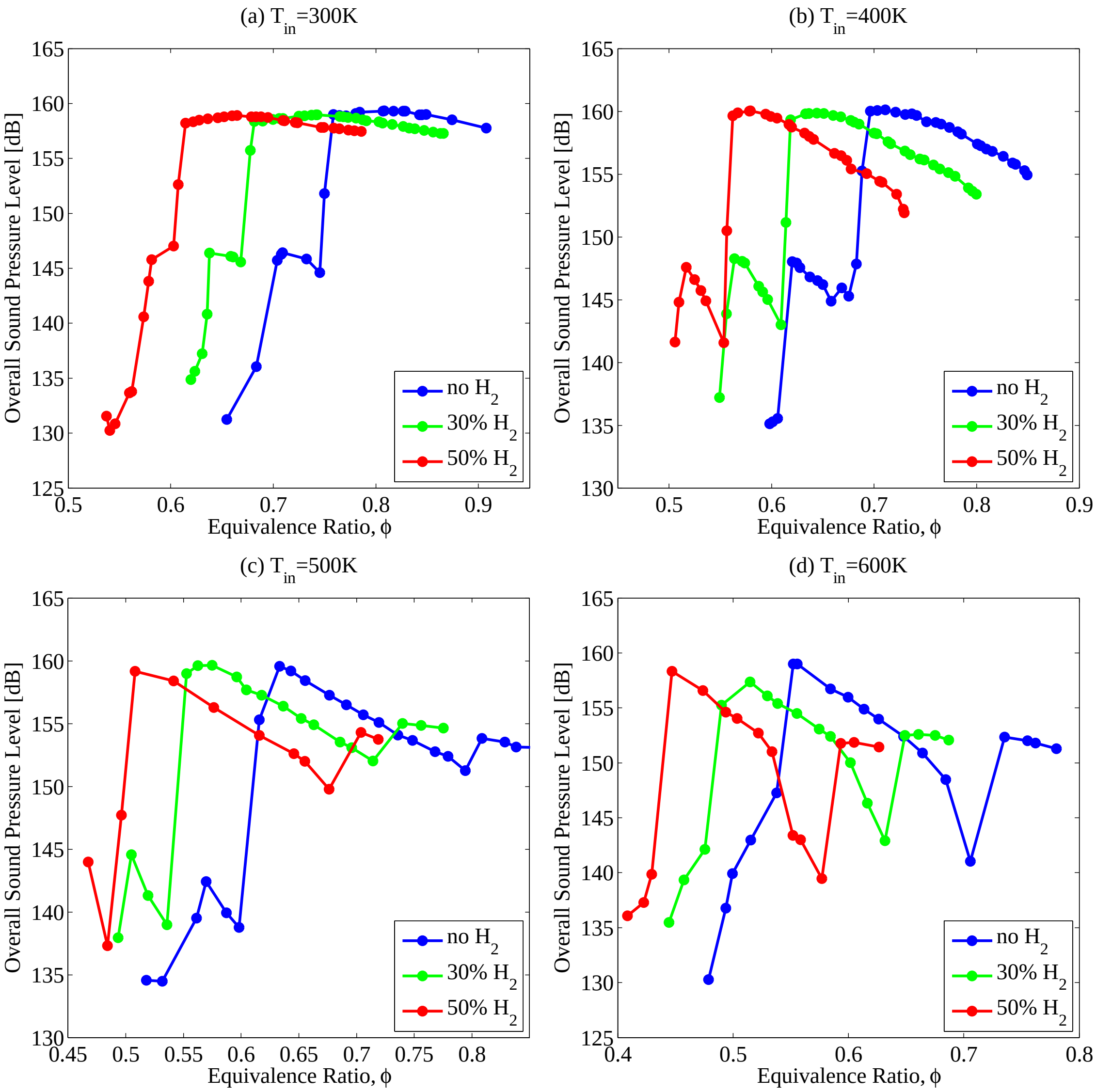

Figure 2-9: OASPL as a function of equivalence ratio at different hydrogen concentration for (a) T_{in}=300 K; (b) T_{in}=400 K; (c) T_{in}=500 K; (d) T_{in}=600 K. Re=6500.

In Fig. 2-10, I plot the simultaneous pressure oscillations measured at four different locations along the length of the combustor corresponding to unstable, high-frequency unstable and quasi-stable modes. For the unstable and quasi-stable modes, the resonant frequency is close to 40 Hz and the pressure oscillations measured at different locations are nearly in phase. This shows that the resonant frequency may correspond to the 1/4 wavemode of the combustor. On the other hand, for the high-frequency

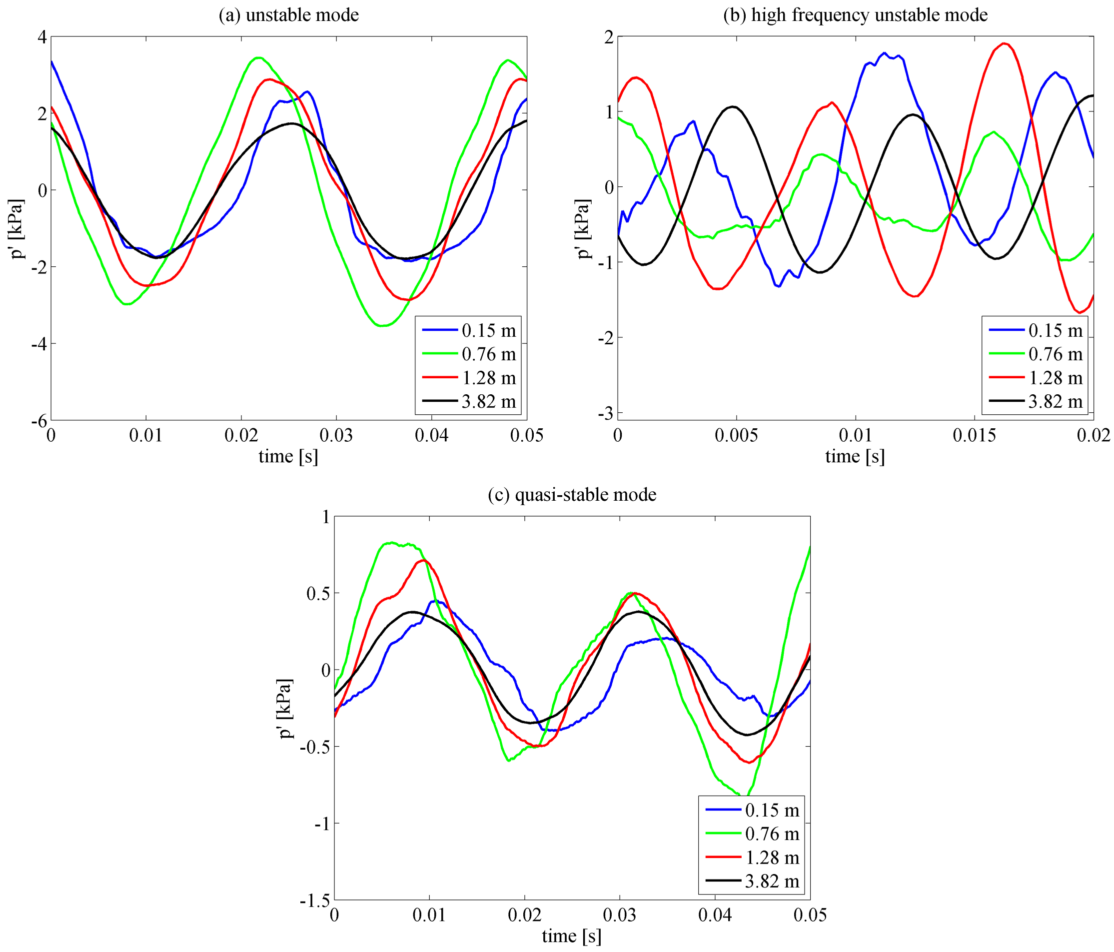

Figure 2-10: Pressure oscillations measured at different locations along the combustor length corresponding to unstable, high-frequency unstable and quasi-stable operating modes.

unstable mode, a pressure node exists between the measurement locations of 0.15 m and 0.76 m (since the pressure measurements are out of phase); and another pressure node exists between measurement locations of 1.28 m and 3.82 m. The presence of two pressure nodes along the length of the combustor suggests that the resonant frequency around 130 Hz may correspond to the 5/4 wavemode. In Fig. 2-11, I plot the pressure modeshapes along the length of the combustor for unstable, high-frequency unstable and quasi-stable modes at the same operating conditions as in Fig. 2-10. The sign of the rms pressure amplitude is reversed whenever measurements at two consecutive locations are out of phase. Figure 2-11 clearly shows that the quasi-stable and

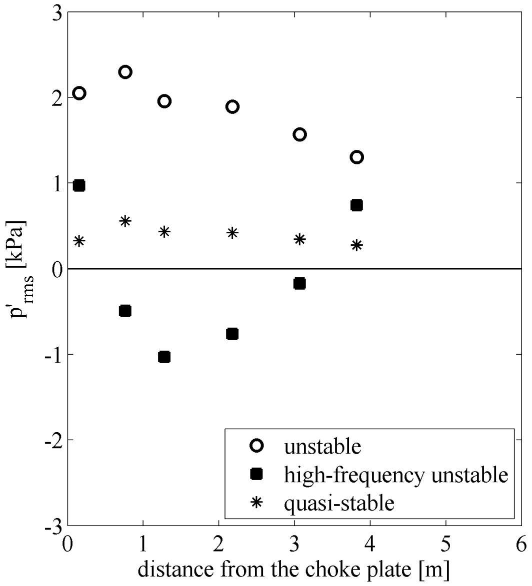

Figure 2-11: Pressure modeshapes corresponding to the unstable, high-frequency unstable and quasi-stable operating modes.

unstable modes correspond to the 1/4 wavemode, and the high-frequency unstable mode corresponds to the 5/4 wavemode of the combustor. The resonant frequency of 130 Hz is much smaller than what I expect for a 5/4 wavemode: 5×40 Hz $= 200$ Hz. Moreover, the pressure oscillations do not satisfy the open boundary condition at the end of the exhaust tube (at 5.0 m) as I expect, suggesting a longer acoustic length. It is also interesting to see that 3/4 wavemode is not excited.

In order to explain the observed resonant frequencies, the combustor acoustics are modeled analytically by solving the linear one-dimensional wave equation while neglecting viscous effects. The Mach number of the flow in our combustor is very low ($\sim$0.02), therefore the effect of the mean flow is neglected. Figure 2-12 shows a schematic diagram of the combustor. The combustor is divided into two regions by the combustion zone. For simplicity, I treat the combustion zone as a thin planar flame located at a fixed axial location. The effect of heat addition at the flame location is neglected for simplicity. The general solution of the homogeneous wave equation can be written in the following form [56]:

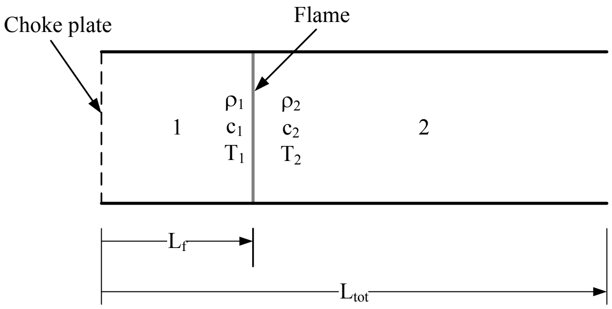

Figure 2-12: Schematic diagram of the combustor used in the acoustic model.

$$p'(x,t) = f(t - x/\bar{c}) + g(t + x/\bar{c}) \tag{2.2}$$

where the functions $f(t)$ and $g(t)$ are arbitrary. From the linearized one dimensional momentum equation, the velocity oscillations are obtained in the following form:

$$u'(x,t) = \frac{1}{\bar{\rho}\bar{c}}\left[f(t - x/\bar{c}) - g(t + x/\bar{c})\right] \tag{2.3}$$

where $\bar{\rho}$ and $\bar{c}$ are the average density and speed of sound, respectively. It is convenient to write $f(t) = Re\left[\hat{f}e^{i\omega t}\right]$ where the circumflex denotes a complex amplitude. Using this notation, I rewrite Eqs. (2.2) and (2.3) as follows:

$$\hat{p}(x) = \hat{f}e^{-i\omega x/\bar{c}} + \hat{g}e^{i\omega x/\bar{c}} \tag{2.4}$$

$$\hat{u}(x) = \frac{1}{\bar{\rho}\bar{c}}\left[\hat{f}e^{-i\omega x/\bar{c}} - \hat{g}e^{i\omega x/\bar{c}}\right] \tag{2.5}$$

In each section of the combustor, Eqs. (2.4) and (2.5) give the pressure and velocity mode shapes. The resonant frequencies follow from the application of the appropriate boundary conditions at the inlet and exit of the combustor and matching the solutions at the flame location.

The solution of the homogeneous wave equation in the upstream section satisfying the choked inlet boundary condition, $\hat{u}_1(0) = 0$ is:

$$\hat{p}_1(x) = A\cos(\omega/\bar{c}_1 x) \tag{2.6}$$

$$\hat{u}_1(x) = -\frac{iA}{\bar{\rho}_1\bar{c}_1}\sin(\omega/\bar{c}_1 x) \tag{2.7}$$

where A is an arbitrary constant. The solution of the homogeneous wave equation in the downstream section satisfying the open exit boundary condition, $\hat{p}_2(L_{tot}) = 0$ is:

$$\hat{p}_2(x) = B\sin[\omega/\bar{c}_2(L_{tot} - x)] \tag{2.8}$$

$$\hat{u}_2(x) = -\frac{iB}{\bar{\rho}_2\bar{c}_2}\cos[(\omega/\bar{c}_2(L_{tot} - x)] \tag{2.9}$$

where B is an arbitrary constant. Matching the velocity and pressure solutions at the location of the flame, $x = L_f$, I obtain the following equation which is solved numerically to calculate the resonant frequencies:

$$\frac{\bar{\rho}_1\bar{c}_1}{\bar{\rho}_2\bar{c}_2} = \tan(\omega/\bar{c}_1 \cdot L_f)\tan[\omega/\bar{c}_2 \cdot (L_{tot} - L_f)] \tag{2.10}$$

Figure 2-13 shows the modeshapes and associated resonant frequencies corresponding to the 1/4, 3/4, 5/4 and 7/4 wavemodes of the combustor. The temperature of the reactants and products are taken as 300 K and 1880 K, respectively, corresponding to a pure propane flame with ϕ =0.70. The speed of sound is 342 m/s in the reactants and 830 m/s in the products. The density of the reactants is 1.194 kg/m^{3}and the density of the products is 0.190 kg/m^3. I assume that the flame is located 8 cm downstream of the dump plane, i.e. L_f=1.06 m. Note that these values change with operating conditions, resulting in small differences in the resonant frequencies shown in Fig. 2-13. The total acoustic length of the combustor, L_{tot}=6.0 m, is consistent

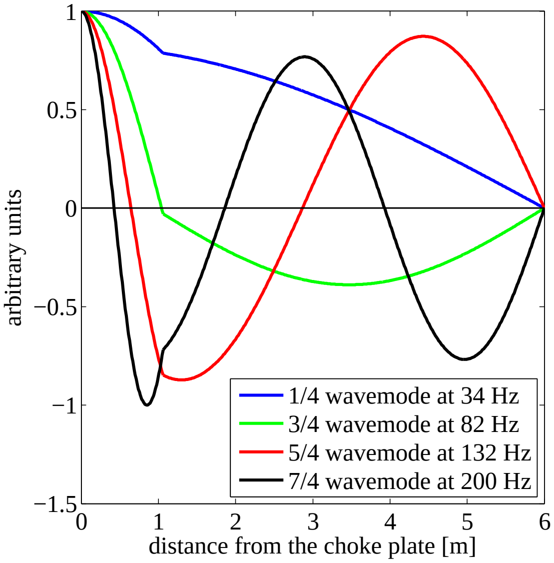

Figure 2-13: Pressure modeshapes calculated from the acoustic model corresponding to the 1/4, 3/4, 5/4 and 7/4 wavemodes.

with the observations in Fig. 2-11, where $p' \approx 0$ around 6 meters downstream of the choke plate.

The observed resonant frequencies as well as the modeshapes are predicted well using the acoustic model. The pressure nodes of the 5/4 wavemode occur around 0.8 m and 2.9 m, which matches closely the experimental measurements shown in Fig. 2-11. These results clearly prove that the unstable and high-frequency unstable operating modes of the combustor correspond to the 1/4 and 5/4 wavemodes, respectively. The resonant frequencies associated with different acoustic modes of the combustor correspond to distinct bands in Fig. 2-7 and Fig. 2-8. However the amplitude is significantly higher at the excited frequencies corresponding to either the 1/4 or the 5/4 acoustic modes depending on the operating conditions.The figure also shows that the location of the flame is very close to a pressure node in the 3/4 wavemode, where the pressure amplitude is very low. This is the reason why the 3/4 wavemode was not excited.

2.2.3 Flame Images

In order to distinguish between the dynamics at different operating modes, I examine flame images extracted from high speed videos of typical unstable, high-frequency unstable, quasi-stable and stable operating modes and describe corresponding unsteady pressure, velocity, heat-release rate and equivalence ratio measurements. The pressure is measured using the sensor located 1.28 m downstream of the choke plate under all operating modes, which is close to the flame location.

Unstable Mode

In Fig. 2-14, a sequence of flame images is shown corresponding to one cycle of the unstable mode taken at ϕ=0.80, Re=8500, T_{in}=300 K, without hydrogen enrichment. Figure 2-15 shows simultaneous heat-release rate, velocity, pressure and equivalence ratio measurements covering the same time period as the images shown in Fig. 2-14. The resonant frequency is 36 Hz, which corresponds to the quarter wave mode of the combustor. Since a hot wire anemometer is used to perform the velocity measurements, I do not have information about the direction of the flow. Therefore, the sign of the hot wire reading is corrected to account for flow reversal. In the unstable mode, a wake vortex is formed in the recirculation zone downstream of the step (1). At this moment, the velocity is rising, and the acceleration and the pressure are at their maxima. As the velocity at the step increases, the vortex convects downstream, while moving towards the upper wall of the combustor. As a result, a packet of unburned reactants forms between the growing vortex and the flame of the previous cycle (2, 3). In addition, the heat-release rate is decreasing following the end of the intense burning from the previous cycle. Between instants 2 and 3, heat-release rate reaches its minimum, and the velocity is near its maximum value. As the velocity drops from its maximum value, the vortex continues to move downstream towards the upper wall of the combustor. The heat-release rate starts to rise as the reactant packet

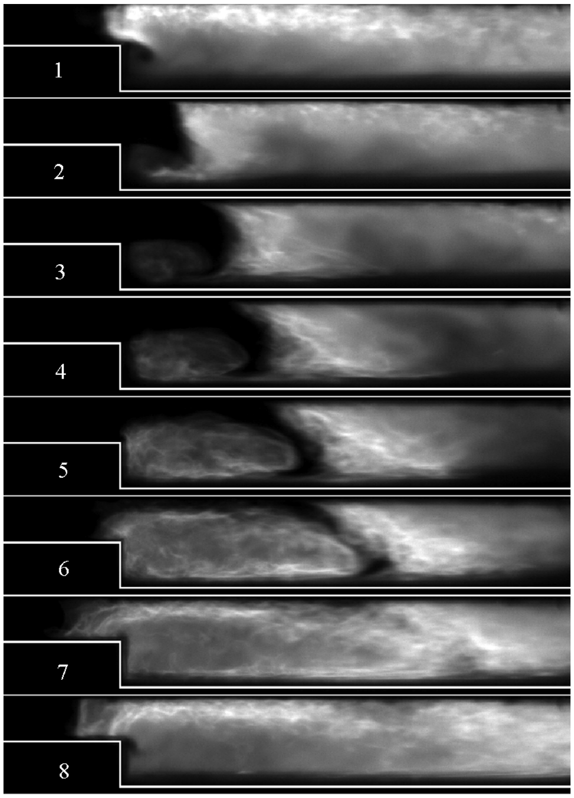

Figure 2-14: Flame images of the unstable mode. ϕ=0.80, Re=8500, T_{in}=300 K, no hydrogen enrichment. The resonant frequency is 36 Hz. The time between the frames is 4 ms.

sandwiched between the flame from the earlier cycle and the flame surrounding the new vortex begins to burn (4-6). As the velocity reaches its minimum value between images 6 and 7, the vortex reaches the upper wall of the combustor, and the reactant packet burns by two "advancing" flames on both sides causing intense burning. As a result, the heat-release rate reaches its maximum near the moment of maximum pressure, resulting in the positive feedback between the unsteady heat-release rate and the pressure, which drives the instability (7). The flame moving upstream of the step indicates very small or negative velocity at the step (6, 7). Next, as the velocity starts to rise again, the heat-release rate starts to drop, fresh reactants enter the flame anchoring zone and the cycle repeats. Since the fuel injector is located far enough from the combustion zone, the equivalence ratio remains nearly constant throughout the cycle. The maximum pressure amplitude is near 3 kPa.

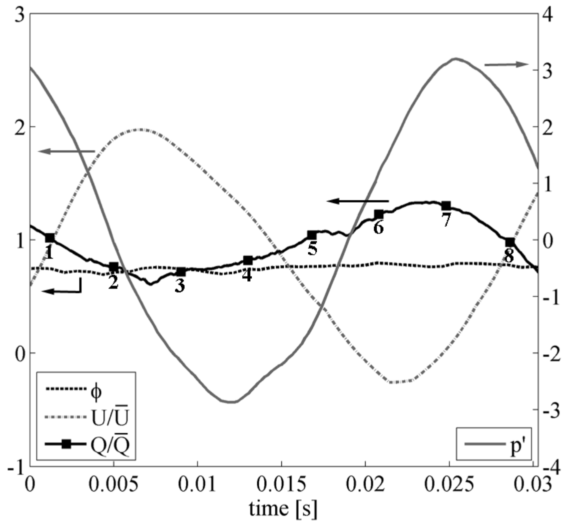

Figure 2-15: Simultaneous heat-release rate, velocity, pressure and equivalence ratio measurements corresponding to the unstable mode shown in Fig. 2-14.

High-Frequency Unstable Mode

When the inlet mixture is preheated to higher temperatures, the instability is observed at higher frequencies. Figure 2-16 shows a sequence of flame images corresponding to one cycle of the high-frequency unstable mode observed at ϕ=0.70, Re=6500, T_{in}=500 K, with 50% by volume hydrogen enrichment. Figure 2-17 shows simultaneous heat-release rate and pressure measurements covering the same time period as the images shown in Fig. 2-16. At elevated inlet temperatures I was not able to do point velocity measurements using the hot wire anemometer. Equivalence ratio measurements are not performed at this operating mode because the quality of the photodiode signal drops significantly as the inlet temperature increases. However, I expect the equivalence ratio to remain temporally constant, because the fuel injector is placed far upstream of the step and as verified at T_{in}=300 K. The resonant frequency is 132 Hz (which corresponds to the 5/4 wavemode of the combustor). The observed combustion dynamics are very similar to the unstable mode described before, except that the unsteady flame dynamics are faster in this case. In this operating mode, the vortex forms at the step when the pressure is at a minimum. Since the step is

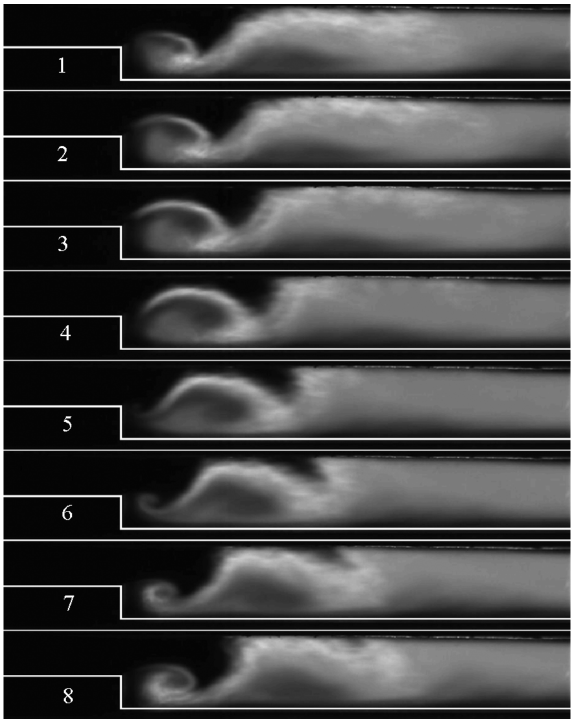

Figure 2-16: Flame images of the high-frequency unstable mode. ϕ=0.70, Re=6500, T_{in}=500 K, with 50% by volume hydrogen enrichment. The resonant frequency is 132 Hz. The time between the frames is 1.1 ms.

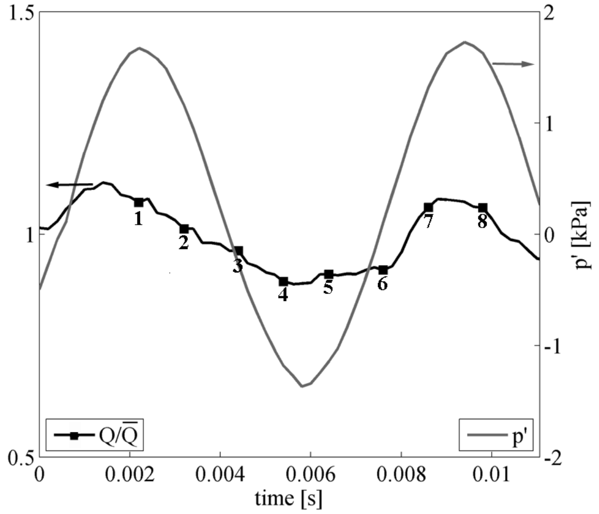

Figure 2-17: Simultaneous heat-release rate and pressure measurements corresponding to the high-frequency unstable mode shown in Fig. 2-16.

located between a pressure node and a pressure antinode (see Fig. 2-13), u' leads p' by 90 degrees. That instant again corresponds to the moment of maximum acceleration, similar to the unstable case. As a result of the higher frequency, the flame is more compact and the wake vortex reaches the upper wall of the combustor closer to the step. The heat-release rate and pressure oscillations are nearly in phase, resulting in the observed instability. The more compact flame causes smaller variations in the flame surface area, resulting in smaller amplitude heat-release rate oscillations compared to the unstable case. The unsteady pressure amplitude is also lower than the unstable case as a result of the smaller amount of energy supplied to the acoustic field due to heat release. The maximum pressure amplitude is around 1.5 kPa.

Quasi-stable mode

When the equivalence ratio is reduced while the combustor is operating in the unstable mode, the noise from the combustor decreases significantly as the equivalence ratio drops below a certain threshold, depending on the operating conditions. This is the quasi-stable operating mode of the combustor, which corresponds to the 140–150 dB plateau observed in Fig. 2-9. In Fig. 2-18, a sequence of flame images is shown corresponding to the quasi-stable mode observed at ϕ=0.70, Re=8500, T_{in}=300 K, without hydrogen enrichment. Figure 2-19 shows simultaneous heat-release rate, velocity, pressure and equivalence ratio measurements covering the same time period as the images shown in Fig. 2-18. The resonant frequency is 38 Hz, corresponding to the 1/4 wavemode of the combustor. A vortex forms at the edge of the step near the moment of maximum acceleration (1). The vortex convects downstream, forming a packet of reactants (4-8). The vortex does not reach the top wall, and the reactant packet is not pinched off by the vortex. Burning is concentrated near the reactant pocket. The burning of the pocket is not sudden and produces weak heat-release rate fluctuations as shown in Fig. 2-19. This results in significantly lower OASPLs

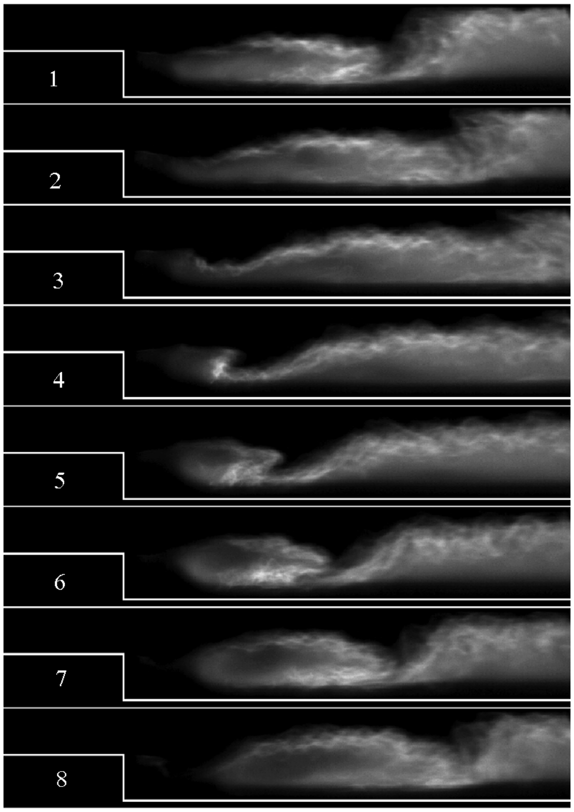

Figure 2-18: Flame images of the quasi-stable mode. ϕ=0.70, Re=8500, T_{in}=300 K, without hydrogen enrichment. The resonant frequency is 38 Hz. The time between the frames is 3.8 ms.

compared to the unstable mode. The maximum pressure amplitude is 0.6 kPa.

Stable mode

Near the lean blowout limit, the combustor operates in the stable mode, resulting in nearly silent burning. As the inlet temperature increases, the stable mode becomes narrower as shown in Fig. 2-9. In Fig. 2-20, a sequence of flame images is shown corresponding to the stable mode observed at ϕ=0.57, Re=6500, T_{in}=300 K, with 50% by volume hydrogen enrichment. Figure 2-21 shows simultaneous heat-release rate and pressure measurements covering the same time period as the images shown in Fig. 2-20. In this case, small vortices are shed from the step at high frequencies. The vortex shedding frequency does not correspond to one of the low frequency modes

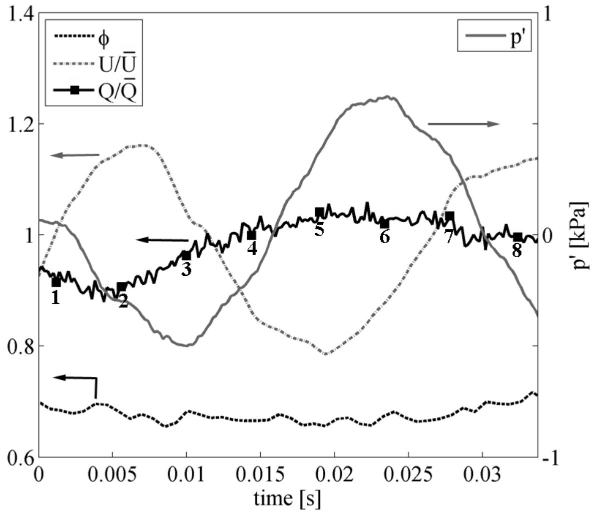

Figure 2-19: Simultaneous heat-release rate, velocity, pressure and equivalence ratio measurements corresponding to the quasi-stable mode shown in Fig. 2-18.

of the combustor. Thus, there is no coupling between the heat-release rate and the pressure as shown in Fig. 2-21. The heat-release rate is steady, and the pressure oscillates at very small amplitude and high frequency, corresponding to the vortex shedding frequency.

2.2.4 Theory

In this section I develop a theory to predict the conditions at which the sudden transition between different dynamics operating modes take place. The high speed flame images of the unstable and high-frequency unstable operating modes revealed that during an unstable cycle, the flame is convoluted around a vortex forming in the wake of the step. Moreover, careful inspection of the results in Figs. 2-14 and 2-16 show that as the wake vortex reaches the upper wall of the combustor, the heat-release rate reaches its maximum value. For both operating modes, the vortex forms at the moment of maximum acceleration. I define the time elapsed between the moment of vortex formation and the moment when the vortex reaches the upper wall (moment of maximum heat-release rate) as τ_{vor}. I assume that the vortex moves towards the

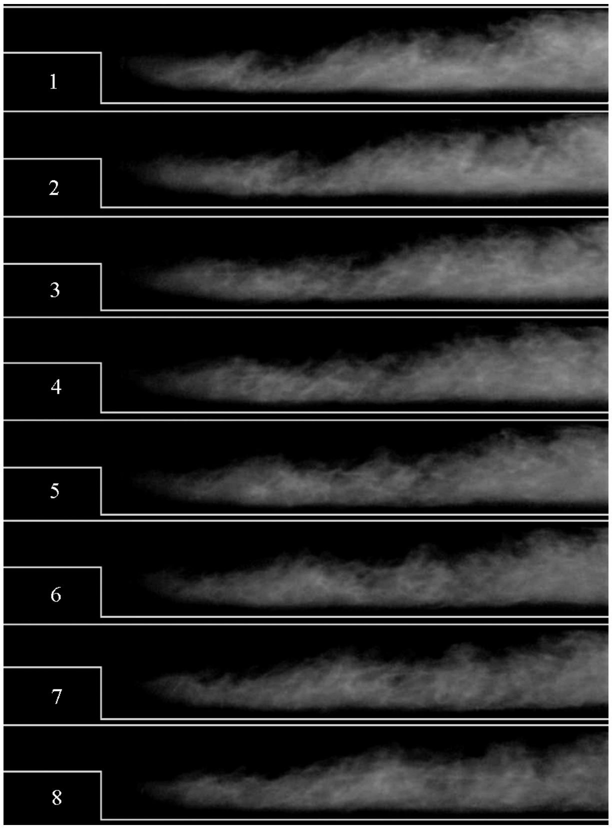

Figure 2-20: Flame images of the stable mode. ϕ=0.57, Re=6500, T_{in}=300 K, with 50% by volume hydrogen enrichment. The time between the frames is 4 ms.

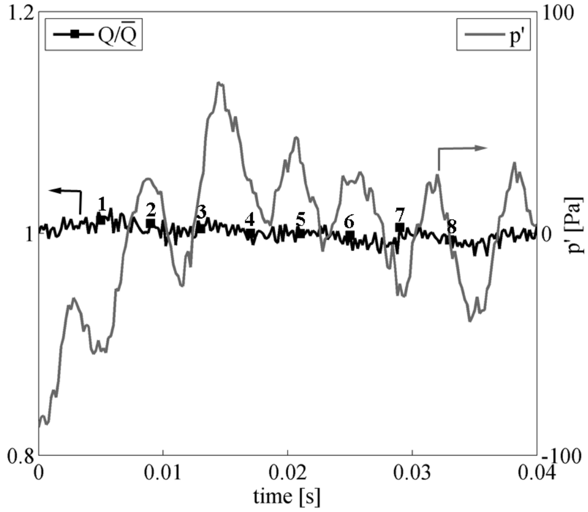

Figure 2-21: Simultaneous heat-release rate and pressure measurements corresponding to the stable mode shown in Fig. 2-20.

wall predominantly as a result of the expansion velocity in the vertical direction. The expansion velocity is proportional to the heat-release rate parameter $S_T(\rho_u/\rho_b - 1)$ where S_T is the turbulent burning velocity and ρ_u and ρ_b are the unburned and burned mixture densities [25]. Assuming a linear relationship between the turbulent and laminar burning velocities, the vertical velocity of the vortex, v_{vor}, is:

$$v_{vor} = \frac{S_L}{c}(\rho_u/\rho_b - 1) \tag{2.11}$$

where S_L is the laminar burning velocity of the mixture. The constant of proportionality between the expansion velocity and the heat-release rate parameter, and the proportionality between the turbulent and laminar burning velocities are represented by an arbitrary constant c. Representing the vertical distance between the corner of the step where the vortex forms and the upper wall as H, I obtain $\tau_{vor} = H/v_{vor}$. Substituting v_{vor} from Eq. (2.11):

$$\tau_{vor} = \frac{cH}{S_L(\rho_u/\rho_b - 1)} \tag{2.12}$$

In Fig. 2-22, I schematically show τ_{vor}, and the time between the maximum heat-release rate and maximum pressure, τ_{qp} , for the unstable and high-frequency unstable cases. The quasi-stable to unstable, and unstable to high-frequency unstable transitions occur when the pressure and heat-release rate oscillations become in phase, that is $\tau_{pq} = NT$, where N is an integer and T is the oscillation period. According to Fig. 2-22, the quasi-stable to unstable transition takes place when (for $N = 1$)

$$\tau_{vor} = \frac{1}{f_{1/4}} \tag{2.13}$$

and the unstable to high-frequency unstable transition takes place when

$$\tau_{vor} = \frac{3}{2}\frac{1}{f_{5/4}} \tag{2.14}$$

(a) Unstable mode

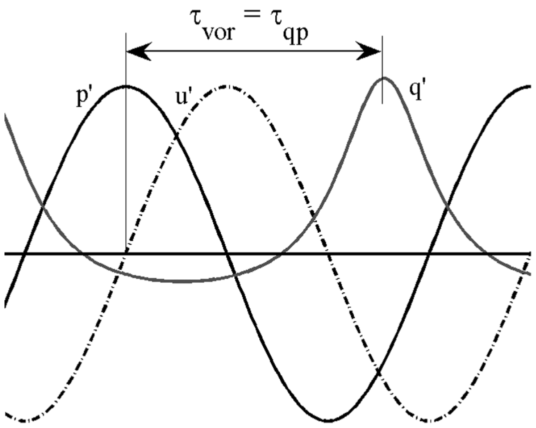

(b) High-frequency unstable mode

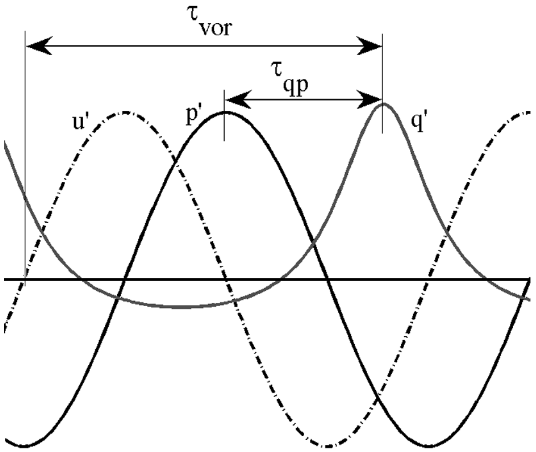

Figure 2-22: Schematic diagram showing pressure, velocity and heat-release rate oscillations in a typical cycle corresponding to the (a) unstable; (b) high-frequency unstable operating modes.

where $f_{1/4}$ and $f_{5/4}$ are the resonant frequencies corresponding to unstable and high-frequency unstable modes. Using Eqs. (2.12) and (2.13), for the quasi-stable to unstable transition (qs→u):

$$S_L(\rho_u/\rho_b - 1)|_{\mathrm{qs}\rightarrow\mathrm{u}} = cHf_{1/4} \tag{2.15}$$

Similarly, using Eqs. (2.12) and (2.14), for the unstable to high-frequency unstable transition (u→hfu):

$$S_L(\rho_u/\rho_b - 1)|_{\mathrm{u}\to\mathrm{hfu}} = \frac{2}{3}cHf_{5/4} \tag{2.16}$$

The left-hand sides of Eqs. (2.15) and (2.16), i.e. the heat release parameters at transition, depend on the operating conditions (ϕ, fuel composition and $\mathrm{T_{in}}$). For a set of operating conditions satisfying Eqs. (2.15) or (2.16), I expect quasi-stable to unstable, or unstable to high-frequency unstable transitions to take place, respectively.

In order to test this hypothesis, I regenerate the response curves of the combustor—the OASPL as function of the equivalence ratio—shown in Fig. 2-9 by plotting the OASPL against the heat release parameter. Since, the dependence on all the operating conditions are represented by this parameter alone, the response curves should collapse onto a global curve independent of the operating conditions. However, attempting to collapse the data using the laminar burning velocity did not produce satisfactory results. For this reason, I focused my attention in modifying the laminar burning velocity by including the role of strain on laminar flames over the same range of equivalence ratios, fuel compositions and inlet temperatures. Especially with different fuel compositions, strain significantly impacts the burning velocity [57].

The effect of strain is investigated by simulating a laminar flame stabilized in a planar stagnation flow. Reactants are supplied on one side, the equilibrium state products of the reactants are supplied on the other, and the flame stabilizes in the vicinity of the stagnation point. The corresponding potential flow velocity field is characterized by the time-varying strain rate parameter a. The one dimensional governing equations for the flame structure are found by using a boundary layer approximation across the flame thickness. The governing equations are discretized using an implicit finite-difference method. The solution is obtained using a preconditioned inexact Newton-Krylov method. Cantera [58] is used to evaluate the chemical source terms and the various physical properties. Because of its strong influence on the diffusion of hydrogen, the Soret contribution to diffusive fluxes is included. Details of the numerical method may be found in Refs. [59, 60]. A reduced chemical kinetic-mechanism for propane combustion developed at the UCSD Center of Energy Research is used [61].

There are many possible ways to define a flame speed for a strained flame. Here, I use the consumption speed, S_c, found by integrating the energy equation across the flame. The consumption speed is defined as

$$S_c = \frac{\int_{-\infty}^{\infty} q'''/c_p dy}{\rho_u \left(T_b - T_u\right)} \tag{2.17}$$

where q''' is the volumetric heat-release rate, c_p is the specific heat of the mixture, y is the coordinate normal to the flame, ρ_u is the unburned mixture density, and T_u and T_b are the unburned and burned temperature, respectively. As the strain rate parameter a approaches 0, the consumption speed approaches the laminar burning velocity.

To understand the effects of strain on propane-hydrogen flames, a comprehensive set of numerical simulations were performed covering the fuel compositions, equivalence ratios and inlet temperatures used in Fig. 2-9, and strain rates ranging from 10 to 6000 s^{-1}. In all cases, the oxidizer was air and the pressure was atmospheric.

The laminar burning velocity, i.e. at $a = 0$, as a function of equivalence ratio for each fuel composition considered in the experiment and inlet temperatures of 300 K and 500 K is shown in Fig. 2-23. The laminar burning velocity is determined by extrapolating the consumption speed to a strain rate of zero, analogous to the commonly-employed technique for determining laminar burning velocity from experimentally-observed strained flames. The burning velocity rises substantially with inlet temperature as expected. For the equivalence ratios considered here, increasing hydrogen concentration raises the burning velocity despite the negligible change in the adiabatic flame temperature as shown in Figure 2-24. Clearly, the impact of hydrogen enrichment is physical and not chemical.

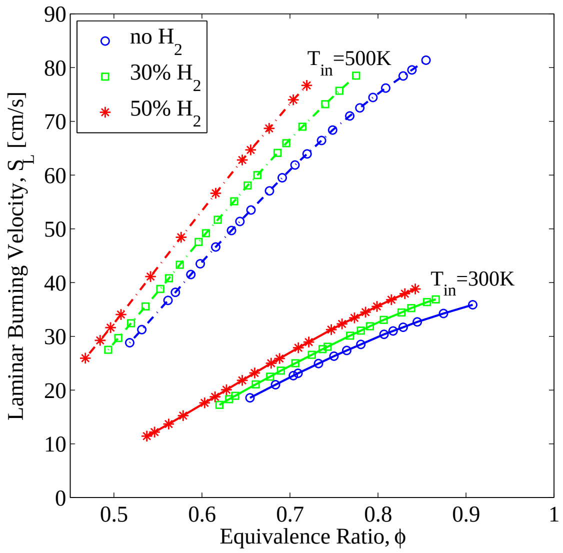

Figure 2-23: Laminar burning velocities of propane-hydrogen flames as a function of equivalence ratio, fuel composition and inlet temperature.

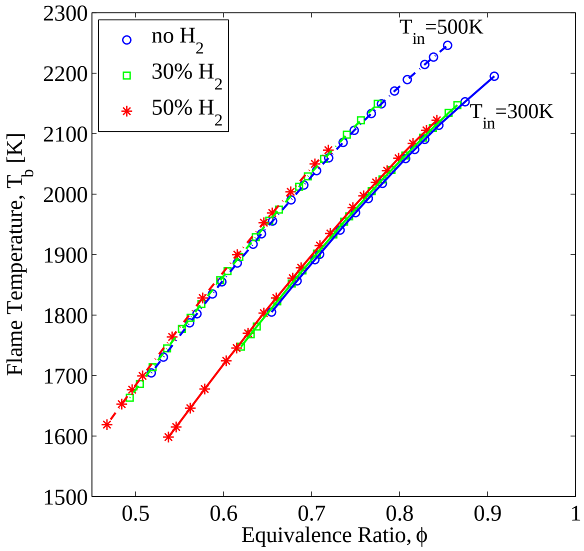

Figure 2-24: Adiabatic flame temperatures of propane-hydrogen flames as a function of equivalence ratio, fuel composition and inlet temperature.

Figure 2-25 shows the effect of strain rate on flames with equivalence ratio $\phi = 0.70$ for each of the fuel compositions considered in the experiment, and inlet tempera-

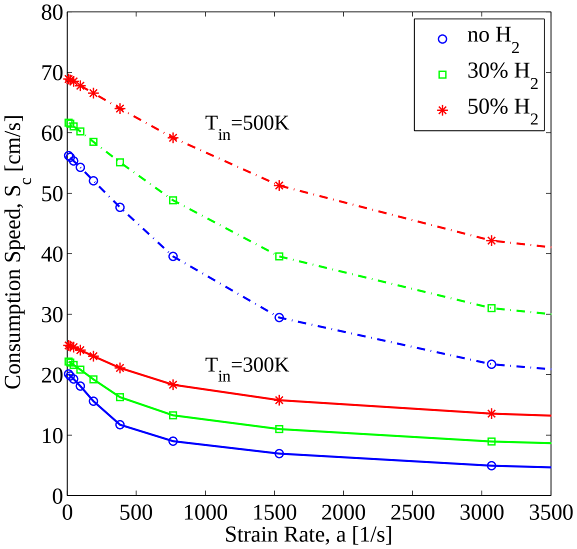

Figure 2-25: Effect of strain rate on consumption speed of flames at $\phi = 0.70$ with varying fuel compositions and inlet temperature.

tures of 300 K and 500 K. Asymptotic analysis of strained flames predicts that the consumption speeds of flames with Lewis numbers greater than unity decrease with positive strain, and that decrease is proportional to the departure of the Lewis number from unity. The results shown in this figure are consistent with the expected trend; the consumption speed of the flames with highest hydrogen content (Lewis number is closest to unity) has the weakest response to increasing the strain rate. When the inlet temperature is raised, the response on the strain rate becomes stronger for all fuel compositions. (In the case of syngas flames, opposite trends were observed for the response of flames with different hydrogen content to the strain rate, since in this case the Lewis number is less than unity. Increasing the amount of hydrogen in syngas flames increases the departure of Lewis number from unity, resulting in stronger response of the consumption speed to strain rate [57, 62])

In Fig. 2-26, I plot the consumption speed as a function of the equivalence ratio for each fuel composition, and inlet temperatures of 300 K and 500 K, at a strain rate of a=2000 s^{-1}. The dependence of the consumption speed on the equivalence ratio

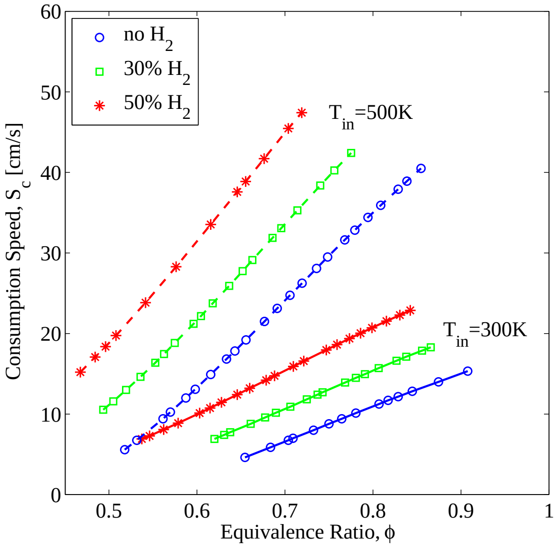

Figure 2-26: Consumption speed of propane-hydrogen flames at a fixed strain rate of a=2000 s^{-1} as a function of equivalence ratio at different fuel compositions and inlet temperatures.

is nearly linear for each fuel composition and inlet temperature. When I compare this figure to the unstrained case, Fig. 2-23, I observe that the strained flames with less hydrogen content are more strongly impacted by the strain rate when compared to higher hydrogen content flames, especially at high equivalence ratios. The Lewis number dependent response of the consumption speed to stretch is greater at higher equivalence ratios.

These results clearly demonstrate that the strained flame consumption speed S_c is more sensitive to the operating conditions than the laminar burning velocity. When using the consumption to reduce the experimental data, there is one undetermined constant a, which can be thought of as a typical strain rate averaged over the entire flame. Here, I select values of a which produces the best correspondence with the experimental data at each inlet temperature, i.e. the value for which the OASPL as a function the heat release parameter looks essentially the same for all fuel compositions at each inlet temperature. In Fig. 2-27 I plot the OASPL against the heat release parameter using the consumption speed for the burning velocity for the data in Fig. 2-9 using strain rates of 2000 s^{-1}, 2300 s^{-1}, 2700 s^{-1} and 3000 s^{-1} for inlet temperatures of 300 K, 400 K, 500 K and 600 K, respectively. As the inlet temperature increases, the average inlet velocity also increases for the same Reynolds number. Because the strain rate is proportional to the velocity, the strain rates are higher at higher inlet temperatures, consistent with the values used in generating Fig. 2-27. Moreover, as the inlet temperature increases, the average flame location becomes closer to the step, where the strain rate is the highest. Here I see that, for the most part, the data are well-correlated with the heat release parameter at these values of the strain rates.

I next proceed to further validate the collapse of the data when plotted against the heat release parameter. I plot the OASPL against the heat release parameter in Fig. 2-28 selecting arbitrary fuel compositions and inlet temperatures from Fig. 2-27. The figure shows that the transitions between different operating modes–independent of the fuel composition, equivalence ratio and the inlet temperature–are correlated well with the heat release parameter, which is a global parameter representing the flame-vortex interaction dynamics. As mentioned before, since the combustor shows strong dependence on the history of the operating conditions, minor differences at different operating conditions are expected. The transition from the quasi-stable to unstable mode occurs at $S_c(\rho_u/\rho_b - 1) \approx 50$ cm/s, and the unstable mode to high-frequency unstable mode transition takes place at $S_c(\rho_u/\rho_b - 1) \approx 120$ cm/s.

Finally, the theory derived in Eqs. (2.15) and (2.16) is verified. R is defined as the ratio between the heat release parameters at the unstable to high-frequency unstable transition and at the quasi-stable to unstable transition. From Eqs. (2.15) and (2.16), using the strained consumption speeds instead of the laminar burning velocities of the unstrained planar flames:

$$R = \frac{S_c(\rho_u/\rho_b - 1)|_{\mathrm{u\rightarrow hfu}}}{S_c(\rho_u/\rho_b - 1)|_{\mathrm{qs\rightarrow u}}} = \frac{2}{3}\frac{f_{5/4}}{f_{1/4}} \tag{2.18}$$

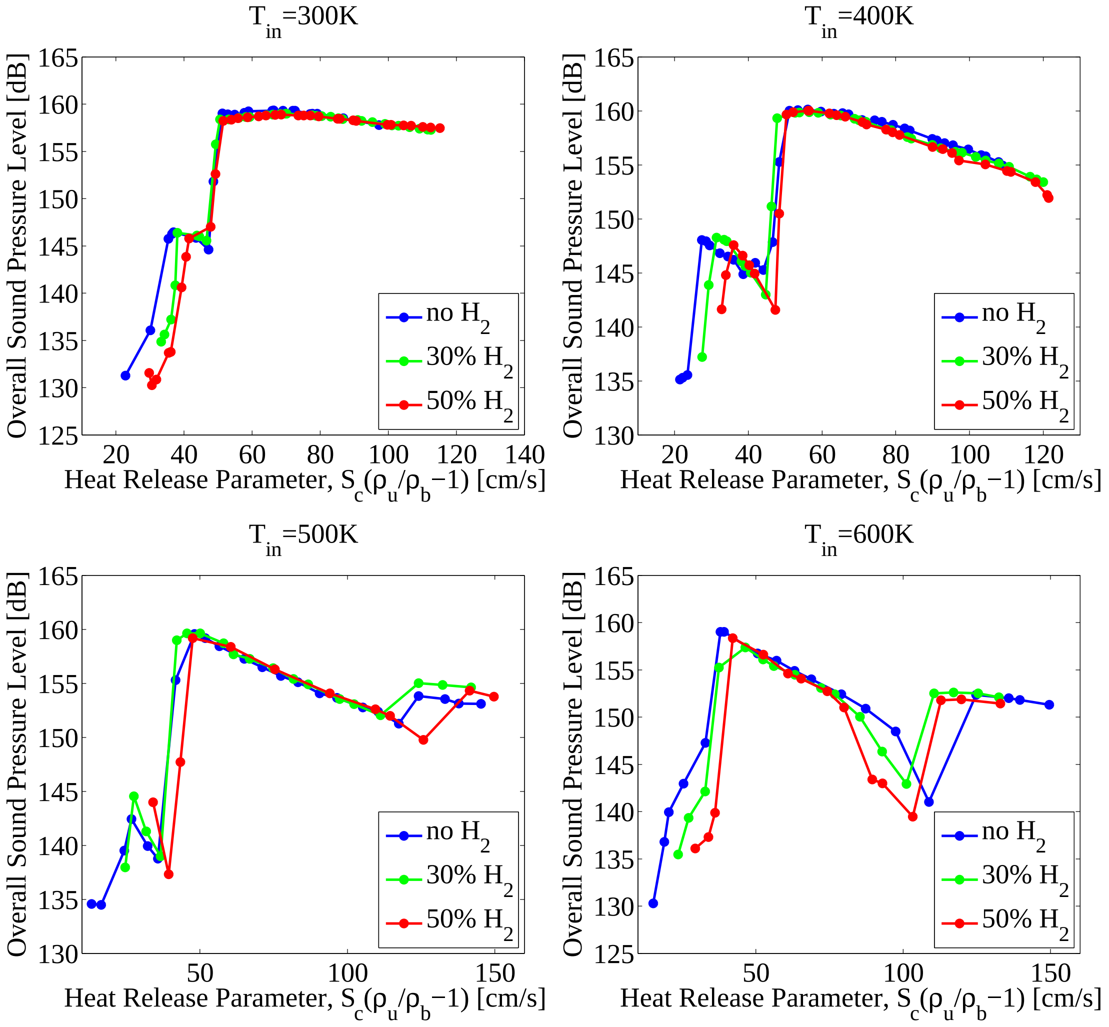

Figure 2-27: OASPL as a function of heat release parameter, $S_c(\rho_u/\rho_b-1)$, at different hydrogen concentrations for (a) T_{in}=300 K, a =2000 s^{-1} ; (b) T_{in}=400 K, a =2300 s^{-1}; (c) T_{in}=500 K, a =2700 s^{-1}; (d) T_{in}= 600 K, a =3000 s^{-1}.

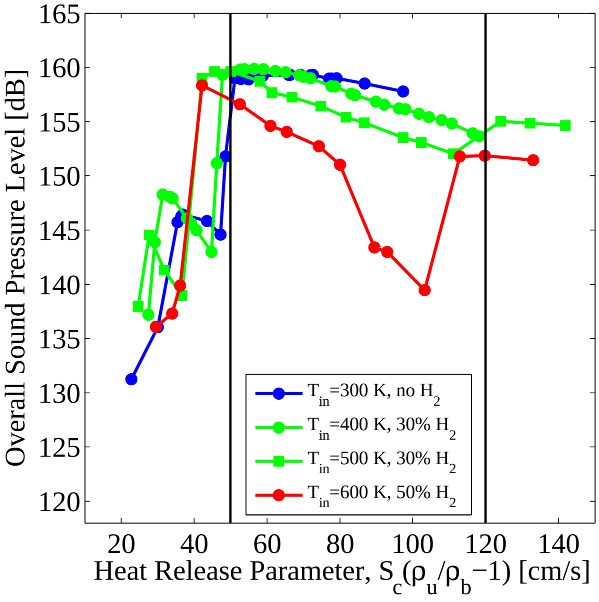

Figure 2-28: OASPL as a function of heat release parameter, $S_c(\rho_u/\rho_b - 1)$, at different hydrogen concentrations and inlet temperatures.

The resonant frequencies corresponding to high-frequency unstable and unstable cases, respectively, are 132 Hz and 36 Hz (see section 2.2.3). Thus, the ratio predicted by the theory is: $R = 2.44$. The ratio found from the experimental measurements is: $R = 120/50 = 2.40$. The theory predicts the experimental measurements with great accuracy! The constant c in Eqs. (2.15) and (2.16) is calculated using the experimental heat-release rate parameter at the quasi-stable to unstable transition:

$$c = \frac{S_c(\rho_u/\rho_b - 1)|_{\text{qs}\rightarrow\text{u}}}{H f_{1/4}} \tag{2.19}$$

which is 0.7.

This analysis show that the stability of the combustor is governed by the transport of the large wake vortex to the upper wall of the combustor. The complicated flame-vortex interaction dynamics can be reduced to a single parameter, $S_c(\rho_u/\rho_b - 1)$, which carries information about the interaction between the flame and the hydrodynamics with different reactant mixture compositions and the volume expansion as a result of the chemical reaction. The former is represented by the consumption speed S_c, and the latter is represented by $\rho_u/\rho_b - 1$.

2.3 Summary

In this chapter, the stability map and combustion dynamics in a backward-facing step combustor are investigated when the dynamics are driven solely by flame-vortex interactions, that is in the absence of equivalence ratio oscillations. Simultaneous pressure, velocity, heat-release rate and equivalence ratio measurements and high-speed video from the experiments were used to identify and characterize several distinct operating modes. Four distinct operating modes were observed depending on the inlet temperature and the equivalence ratio. At high but lean equivalence ratios, the combustor is unstable as a result of the strong interaction between the large unsteady wake vortex and the flame. The flame propagates upstream of the step during a part of the cycle. At intermediate equivalence ratios, the combustor is quasi-stable with the flame staying attached to the step at all times. Near the blowout limit, long stable flames are observed. When the inlet temperature is atmospheric, the quasi-stable and the unstable flames couple with the 1/4 wavemode of the combustor. When the inlet temperature is increased, at high but lean equivalence ratios, the 5/4 wavemode of the combustor is excited, increasing the resonant frequency significantly. This operating mode is the high-frequency unstable mode, where the flame is more compact compared to the unstable case. Increasing the inlet temperature and hydrogen concentration shifts the response curves of the combustor towards lower equivalence ratios. As the inlet temperature is increased, the stable operating band becomes narrower. The vertical velocity of the large wake vortex is proportional to the heat release parameter, and controls the moment when the vortex reaches the upper wall of the combustor producing a heat release pulse. I demonstrated that the consumption speed of strained flames can be used to collapse the response curves describing the transitions among different dynamic modes onto a function of the heat release parameter alone. I predict the critical values of the heat release parameter at which transitions between quasi-stable to unstable, and unstable to high-frequency unstable operating modes take place, which may provide significant benefits during the design stage of the combustors.

Chapter 3

The Impact of Equivalence Ratio Oscillations on Combustion Dynamics

In this chapter, the experiments are conducted in the combustor described in the previous chapter to describe the impact of the equivalence ratio oscillations on combustion dynamics. For this purpose, experiments are performed by moving the fuel injector to a location closer to the step compared to the location of the fuel injector in the previous chapter. The fuel injector location effects the convective time required for the equivalence ratio oscillations formed at the location of the fuel injector to reach the flame zone, therefore, effecting the turbulent mixing time. If the fuel injector is close enough to the location of the step, I expect the equivalence ratio reaching the flame to oscillate; causing the dynamics to be driven by the compound action of the flame-vortex interactions and the equivalence ratio oscillations.

3.1 Results

A series of experiments are conducted in order to examine how the presence of equivalence ratio oscillations impacts the combustion dynamics. I systematically change the Reynolds number the mean equivalence ratio between the lean blowout limit and near stoichiometry. I measure fluctuations in pressure, heat-release rate, and flow velocity; and temporal and spatial variations of the equivalence ratio.

3.1.1 Equivalence Ratio Measurements

The temporal oscillations of the equivalence ratio, and the non-uniformities in the equivalence ratio distribution near the flame zone can significantly affect the combustion dynamics by impacting the local burning velocity along the flame front as well as the flame structure. In order to achieve truly premixed combustion, the spatial equivalence ratio distribution entering the flame zone should be uniform. I measure the spatial distribution of the equivalence ratio placing the fuel injector 28 cm upstream of the step under steady, non-reactive conditions using the technique described in Section 2.1. Figure 3-1 shows the measured equivalence ratio distributions at a cross section immediately downstream of the step at Re=6500. The mean equivalence ratio is set at 0.70. The uniformity of the mixture composition is satisfactory, but there are two peaks in the spanwise direction, and troughs in the lower-left and upper-right corners possibly as a result of the non-uniform base pressure distribution along the fuel injector holes.

Figure 3-2 shows the temporal variation of the equivalence ratio measured 14 cm upstream of the step when the combustor is fired at a mean equivalence ratio of 0.80, Reynolds number of 8500, again when the fuel injector is located 28 cm upstream of the step. Significant temporal variations in the equivalence ratio are observed, ranging from 0.45 to 1.35. The combustion dynamics in this case are expected to

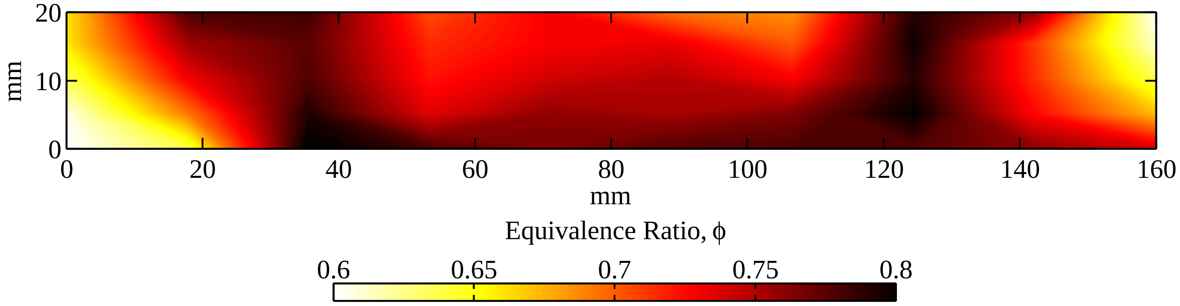

Figure 3-1: Equivalence ratio distribution at a cross section immediately downstream of the fuel injector at Re=6500. The mean equivalence ratio is 0.70. Fuel is injected 28 cm upstream of the step.

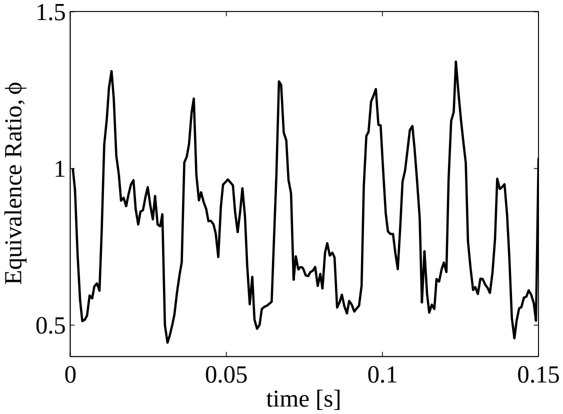

Figure 3-2: Temporal equivalence ratio measurements 14 cm upstream of the step at Re=8500, ϕ =0.80 while injecting the fuel 28 cm upstream of the step.

be governed by both flame-vortex interactions and the equivalence ratio oscillations. Note that diffusion takes place during the transport of the fuel from the measurement location to the flame, which results in lower equivalence ratio oscillation amplitude at the flame compared to the location of the measurements. In order to determine the equivalence ratio reaching the flame zone accurately, I use a one-dimensional convection-diffusion model for scalar transport. The convection-diffusion equation for the fuel with constant mixture density and diffusion coefficient is:

$$\bar{\rho}\frac{\partial Y_f}{\partial t} + \bar{\rho}U(t)\frac{\partial Y_f}{\partial x} = \bar{\rho}D\frac{\partial^2 Y_f}{\partial x^2} + \dot{S}_f(x) \tag{3.1}$$

where $\bar{\rho}$ is the mixture density, Y_f is the mass fraction of the fuel, D is the turbulent diffusion coefficient, U is the flow velocity, and $\dot{S}_f$ is the volumetric rate of fuel addition. The relationship between the equivalence ratio and the fuel mass fraction is:

$$\phi = \frac{Y_f}{FA_s(1 - Y_f)} \tag{3.2}$$

where FA_s is the stoichiometric fuel-air ratio. The initial fuel mass fraction corresponds to the value of the mean equivalence ratio downstream the location of the fuel injector, and zero elsewhere. Equation (3.1) is solved numerically using a finite difference method in a uniform grid, with implicit forward-time, centered-space discretization. $\dot{S}_f = \dot{m}_f/(A_{cs}\Delta x)$ at the location of the fuel injector and zero everywhere else, where $\dot{m}_f$ is the mass flow rate of the injected fuel, which is constant with time, i.e. choked fuel injector, A_{cs} is the cross-sectional area of the combustor, and Δx is the step size used in the numerical calculations.

In order to examine the validity of the convection-diffusion model, in Figs. 3-3 and 3-4, I compare the equivalence ratio calculated by numerically solving Eq. 3.1 at the location of the experimental measurements (14 cm upstream of the step) with the experimental measurements. The operating conditions are: Re=8500, $\bar{\phi} = 0.80$ in Fig. 3-3, and Re=8500, $\bar{\phi} = 0.70$ in Fig. 3-4. I impose the experimentally measured flow velocities in the numerical model. The velocity measurements are performed 22 cm upstream of the step using a hot wire anemometer. Because the distance between the velocity measurement location and the step is small compared to the acoustic length of the combustor (5 m), the amplitude of the velocity oscillations is almost constant between the locations of the fuel injector and the step; therefore, is represented well with the experimental measurements. I selected the parameters in the numerical model to correspond to the values used in the experiment: $\dot{m}_f = 1.16$ g/s and $\bar{\rho} = 1.197$ kg/m^3 in Fig. 3-3, and $\dot{m}_f = 1.02$ g/s and $\bar{\rho} = 1.194$ kg/m^3 in Fig. 3-4. The turbulent diffusion coefficient is selected to give the best match with

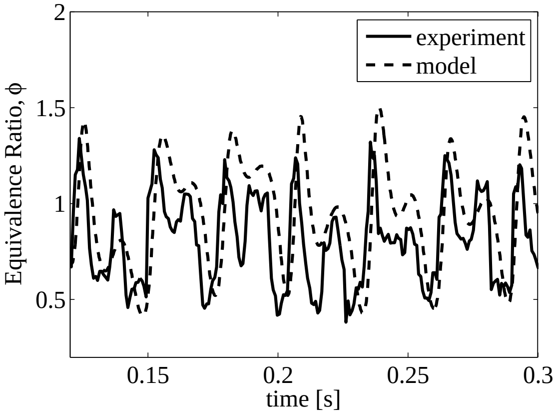

Figure 3-3: Equivalence ratio as a function of time 14 cm upstream of the step calculated numerically solving the convection-diffusion model and measured experimentally. Re=8500 and $\bar{\phi} = 0.80$.

the experimental measurements: $D = 0.015$ m^2/s in Fig. 3-3, and $D = 0.01$ m^2/s in Fig. 3-4. Figure 3-5 compares the measured velocity at $\bar{\phi} = 0.80$ and $\bar{\phi} = 0.70$. The velocity oscillations are strong and there is significant flow reversal at some part of the cycle at $\bar{\phi} = 0.80$. However, the oscillations are weak and the flow does not reverse at $\bar{\phi} = 0.70$. Therefore, the turbulent intensity is expected to be larger at $\bar{\phi} = 0.80$, resulting in a higher turbulent diffusion coefficient, consistent with the selected values.

The phase between the equivalence ratios measured experimentally and calculated numerically agree well. The model slightly over predicts the maximum value of the equivalence ratios when $\bar{\phi} = 0.80$, however there is an overall good matching between the measurements and the prediction of the simple one-dimensional convection-diffusion model. These results show that the convection-diffusion model using appropriate values of diffusion coefficients represents the temporal equivalence ratio variations accurately. In the rest of this chapter, the equivalence ratio arriving at the flame base, i.e. equivalence ratio at the step, is calculated by solving the convection-diffusion model numerically.

The equivalence ratio oscillations shown in Fig. 3-3 exhibit cyclic variation char-

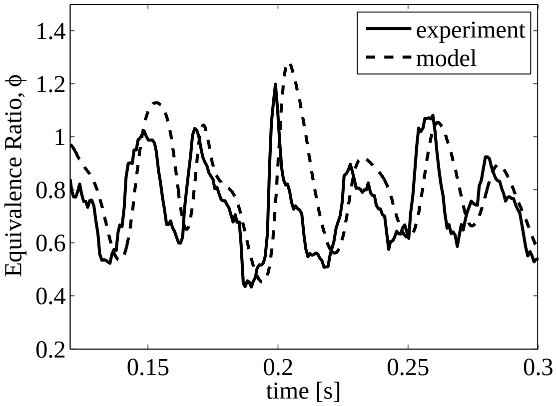

Figure 3-4: Equivalence ratio as a function of time 14 cm upstream of the step calculated numerically solving the convection-diffusion model and measured experimentally. Re=8500 and $\bar{\phi} = 0.70$.

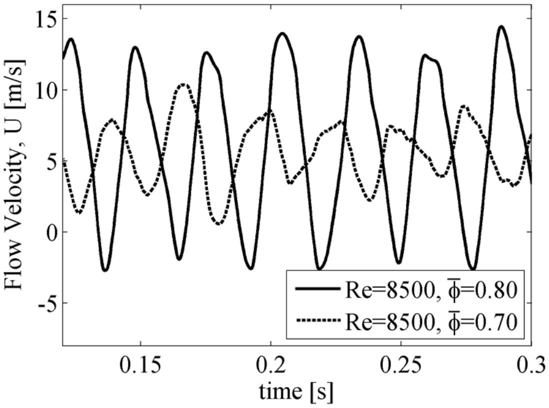

Figure 3-5: Flow velocity as a function of time measured using a hot wire anemometer 22 cm upstream of the step.

acterized by a high amplitude sharp peak followed by a low amplitude broad peak in each cycle, whereas this behavior is not observed in Fig. 3-4. Investigating Fig. 3-5 carefully, I conclude that the low amplitude peak observed in Fig. 3-2(b) arises as a result of the flow reversal taking place during part of the cycle.

3.1.2 Pressure Measurements

In this section, the response curves of the combustor are compared, i.e. pressure amplitude plotted against the mean equivalence ratio, $\bar{\phi}$, when the dynamics are driven solely by the flame-vortex interactions (fuel injector located 93 cm upstream of the step, L_{inj} = 93 cm), and when they are driven by the compound action of the flame-vortex interactions and the equivalence ratio oscillations (L_{inj} = 28 cm). I performed the experiments at Re=6500 and Re=8500. The pressure amplitude is reported in terms of the overall sound pressure level (OASPL) using the pressure sensor located 1.28 m downstream of the choke plate, which is close to the flame location. Note that the combustion dynamics are impacted significantly by the history of the operating conditions, which is reported in the previous chapter. For this reason, all the data are obtained while decreasing the mean equivalence ratio from near stoichiometry (where the flame flashes back to the inlet channel) towards the lean blowout limit.

Figure 3-6 compares the response curves at both fuel injector locations, at Re=6500 and Re=8500. When L_{inj} = 93 cm, the response curves show distinct operating bands at both values of Re. At this location of the fuel injector, there is no measurable effect of Re. At high equivalence ratios the OASPL is around 160 dB, which I refer to as the *unstable* mode. Video images show that at this operating mode, the strong unsteady interactions between the large wake vortex and the flame governs the dynamics. At medium equivalence ratios, the OASPL drops to around 145 dB. This is the *quasi-stable* operating mode of the combustor where the wake vortex-flame interactions are

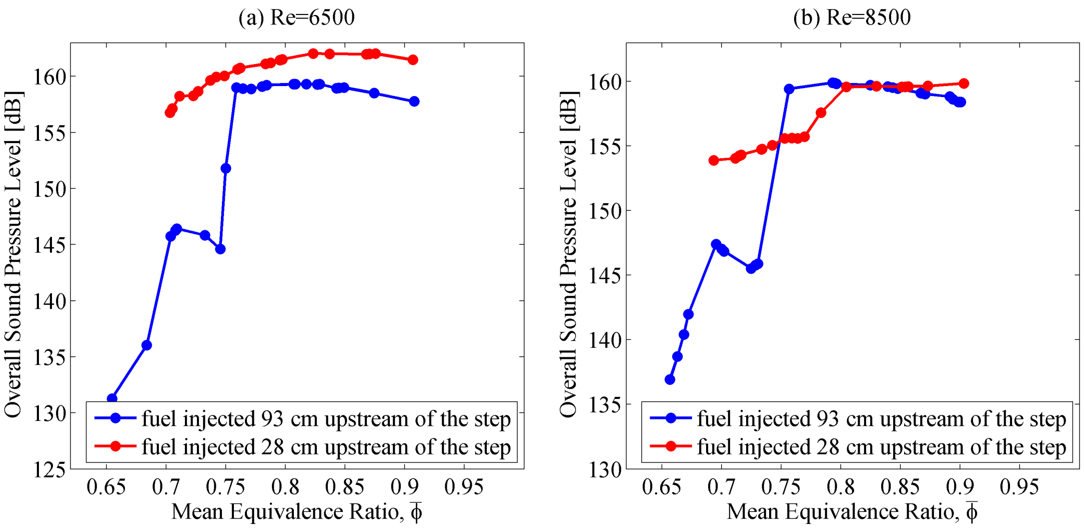

Figure 3-6: OASPL as a function of the mean equivalence ratio when the fuel injector is located 93 cm or 28 cm upstream of the step at (a) Re=6500; (b) Re=8500.

weaker. Near the lean blowout limit, the combustor operates in the *stable* regime with a corresponding OASPL around 135 dB. In this regime, small vortices are shed from the step at high frequencies which does not correspond to the resonant acoustic frequencies of the combustor. The dynamics of each of these distinct operating modes have been described extensively in the previous chapter.

When $L_{inj} = 28$ cm, the dynamics change significantly because of the survival of the equivalence ratio oscillations introduced at the fuel injector location, ϕ'_{inj}, as they are convected to the flame location. Under these conditions, and at both values of Re, the OASPL is always greater than the values corresponding to the quasi-stable or the stable mode. Moreover, the mean equivalence ratio at the lean blowout limit increases. When Re=6500; ϕ' causes the OASPL to rise compared to the cases when the dynamics are driven only by the flame-vortex interactions. At $\bar{\phi} < 0.70$, the flame blows out. At Re=8500; ϕ' acts to decrease (increase) the OASPL compared to the cases when the dynamics are driven only by the flame-vortex interactions for $0.75 < \bar{\phi} < 0.80$ $(0.70 < \bar{\phi} < 0.75)$. At $\bar{\phi} < 0.70$, again the flame to blows out. The Reynolds number impacts combustion dynamics when equivalence ratio oscillations

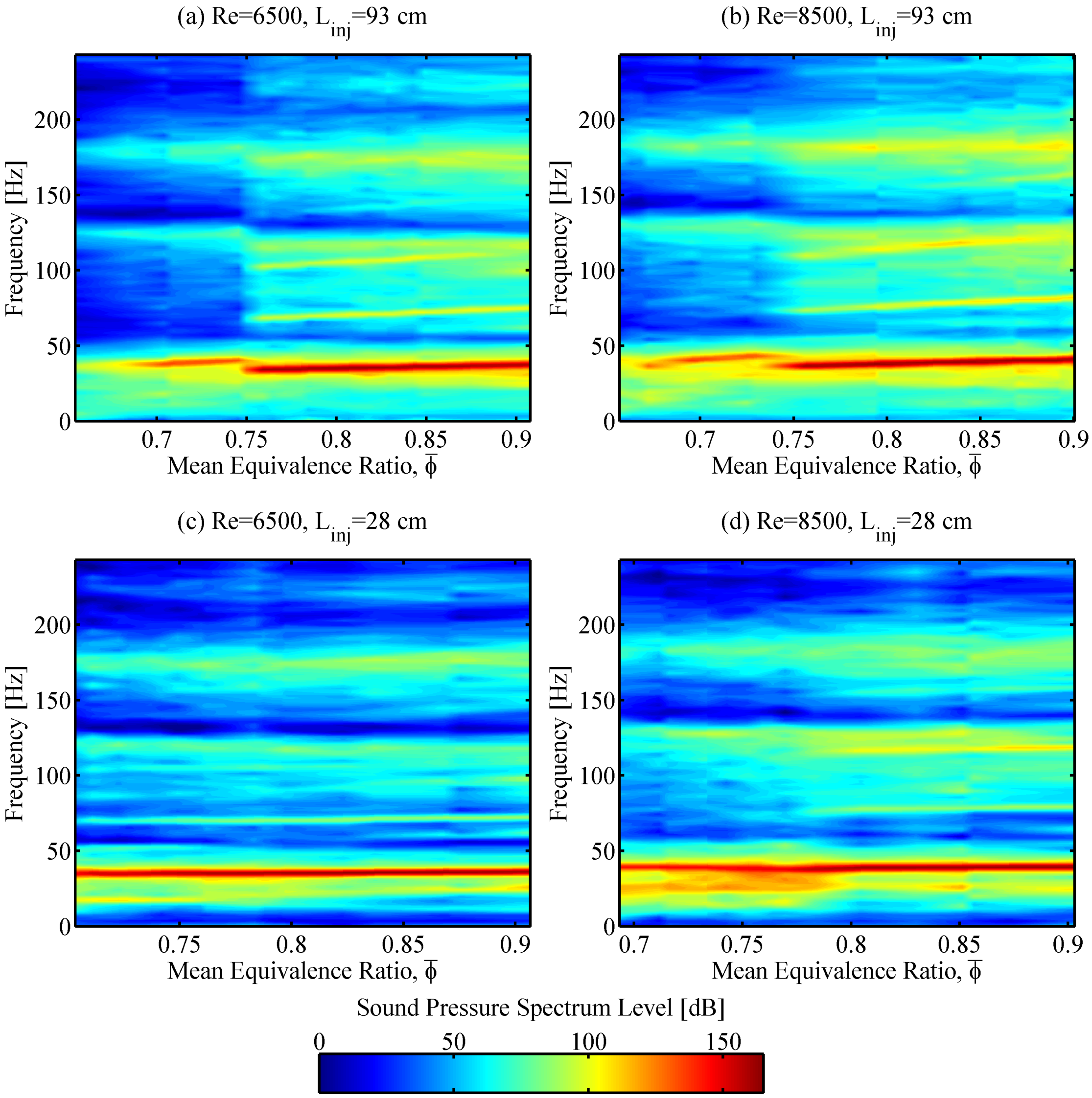

Figure 3-7: Sound pressure spectrum level maps as a function of the mean equivalence ratio for the same cases in Fig. 3-6.

are present. ϕ'_{inj} is convected towards the flame zone with the flow velocity. Therefore, the equivalence ratio near the flame depends on the flow velocity, i.e. Re, which effects the combustion dynamics.

I plot the combustor's frequency response in Fig. 3-7 corresponding to the cases in Fig. 3-6. These figures show the amplitude of the pressure oscillations as a function of the frequency for the ranges of the mean equivalence ratios in Fig. 3-6. The resonant frequency for all cases is around 40 Hz, which corresponds to the 1/4 wavemode of the combustor. I observe low amplitude bands around 80 Hz, 130 Hz and 170 Hz, which correspond to the 3/4, 5/4 and 7/4 wavemodes of the combustor, respectively (see Section 2.2.2). The figure shows that when L_{inj}=93 cm, the resonant frequency increases slightly at the unstable mode to quasi-stable mode transition. Moreover, near the lean blowout limit, the pressure amplitude is very low, because the flame is stable. When L_{inj}=28 cm, the pressure amplitude is large and the resonant frequency remains the same across the entire range of $\bar{\phi}$. These observations show that the combustor's operating mode is never stable or quasi-stable when ϕ' are present at the Reynolds numbers I performed the experiments.

In order to investigate the impact of ϕ' on combustion dynamics further, in Fig. 3-8, I plot the pressure oscillations measured at $\bar{\phi}$ =0.80 and $\bar{\phi}$ =0.70, at Re=6500 and Re=8500, when L_{inj}=28 cm. I observe that the pressure amplitude is constant at both values of the Re when $\bar{\phi}$=0.80. When $\bar{\phi}$=0.70, the pressure amplitude changes between cycles at both values of Re. This suggests that in some cycles the heat-release rate does not couple positively with the pressure oscillations, reducing the pressure amplitude of the next cycle, and explains the drop in the OASPL as $\bar{\phi}$ is dropped. This mechanism is stronger at Re=8500, which shows a decrease in the OASPL as $\bar{\phi}$ is dropped below 0.80 as shown in Fig. 3-6(b). The mechanism responsible for this behavior will become clear in the next section when I investigate the high speed flame images; the simultaneous pressure, velocity, and heat-release rate measurements; and the numerically calculated equivalence ratio arriving at the step.

3.1.3 High Speed Flame Images

Now, I examine the flame images extracted from high speed videos of typical operating modes driven by the compound effects of the flame-vortex interactions and the equivalence ratio oscillations; and describe the corresponding pressure, velocity, and heat-release rate measurements; and the numerically calculated equivalence ratio

(a) Re=6500, $\bar{\phi}$=0.80

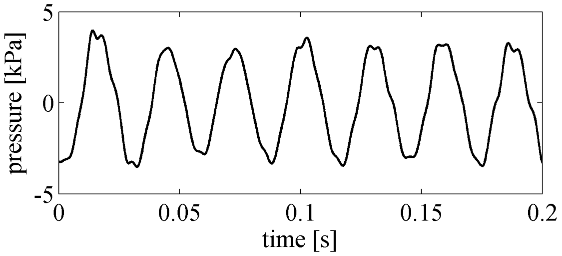

(b) Re=8500, $\bar{\phi}$=0.80

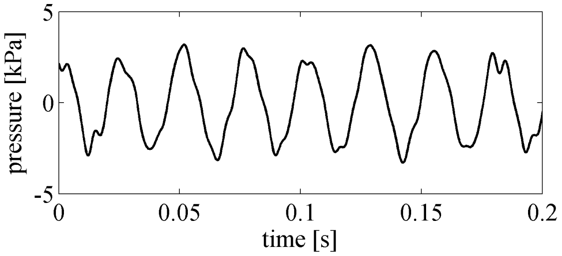

(c) Re=6500, $\bar{\phi}$=0.70

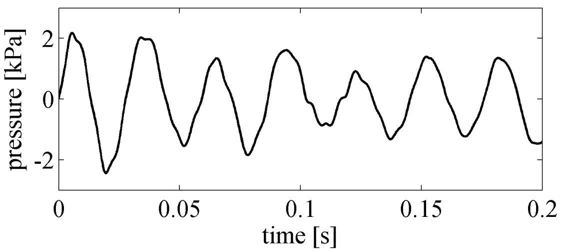

(d) Re=8500, $\bar{\phi}$=0.70

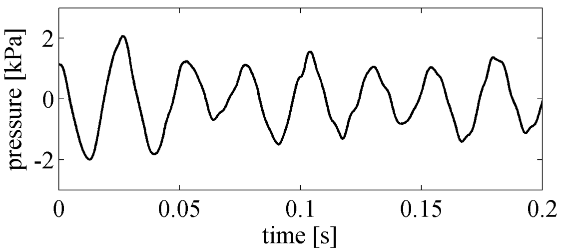

Figure 3-8: Pressure oscillations near the flame at: (a) Re=6500, $\bar{\phi} = 0.80$; (b) Re=8500, $\bar{\phi} = 0.80$; (c) Re=6500, $\bar{\phi} = 0.70$; (d) Re=8500, $\bar{\phi} = 0.70$.

arriving at the step. The pressure is measured using the sensor located 1.28 m downstream of the choke plate under all operating conditions, which is close to the flame location. The velocity measurements are performed 22 cm upstream of the step using a hot wire anemometer. I plot the temporal equivalence ratio variations at the step, ϕ_{step}, by solving the convection-diffusion equation numerically imposing the experimentally measured flow velocity using appropriate values of diffusion coefficients in

Eq. (3.1). I plot the instantaneous non-dimensional heat-release rate $\mathrm{Q}/\bar{\mathrm{Q}}$ using the value of the integrated CH^* chemiluminescence, $\mathrm{CH}^*/\overline{\mathrm{CH}^*}$. Because the equivalence ratio is not uniform spatially in the flame zone, $\mathrm{CH}^*/\overline{\mathrm{CH}^*}$ is a *qualitative* indicator of the heat-release rate [63], which is sufficient to observe the coupling between the heat-release rate and the pressure.

Re=8500 and $\bar{\phi}$=0.80

In Fig. 3-9, I show a sequence of flame images recorded during a representative cycle of oscillations at Re=8500 and $\bar{\phi} = 0.80$. Figure 3-10 shows the simultaneous heat-release rate, velocity and pressure measurements, and Fig. 3-11 shows ϕ_{step} calculated by solving the convection-diffusion equation numerically covering the same time period as the images shown in Fig. 3-9. The diffusion coefficient, $D = 0.015$ m^2/s, as suggested before in Section 3.1.1. The resonant frequency is 35 Hz, which corresponds to the 1/4 wavemode of the combustor.

At the moment of maximum flow acceleration, a wake vortex forms at the hot recirculation zone downstream of the step (1). At this moment, the pressure is near its maximum value and the heat-release rate starts to drop from its maximum value as the burning taking place during the previous cycle, which is concentrated near the downstream edge of the flame image, is completed. ϕ_{step} is around 0.8. As the velocity increases towards it maximum value, the vortex convects downstream while ϕ_{step} drops to its minimum value of around 0.72 (2). When the burning from the previous cycle is completed, the heat-release rate reaches its minimum value (between instants 2 and 3). Next, ϕ_{step} reaches its maximum value of around 1.1 (3). At this moment, the fresh mixture entrained by the vortex with high equivalence ratio starts to burn intensively around the vortex, causing the heat-release rate to increase. Just downstream of the vortex, there is no burning. The vortex accelerates in the streamwise direction and moves towards the upper wall of the combustor as a result of the combustion driven volume expansion (4, 5). As a consequence, the flame area increases, raising the heat-release rate. Because ϕ_{step} is very lean at instant 5, the burning rate near the step is low. At instant 6 the flow reverses, causing the flame to move upstream of the step. The vortex reaches the upper wall of the combustor, limiting the further expansion of the flame area. As a result the heat-release rate reaches its maximum value. After this, the inlet velocity rises again (7), and the cycle repeats. The maximum pressure amplitude is around 3.2 kPa. These dynamics are repeated in every cycle, thus the amplitude of the pressure and the velocity oscillations remain constant.

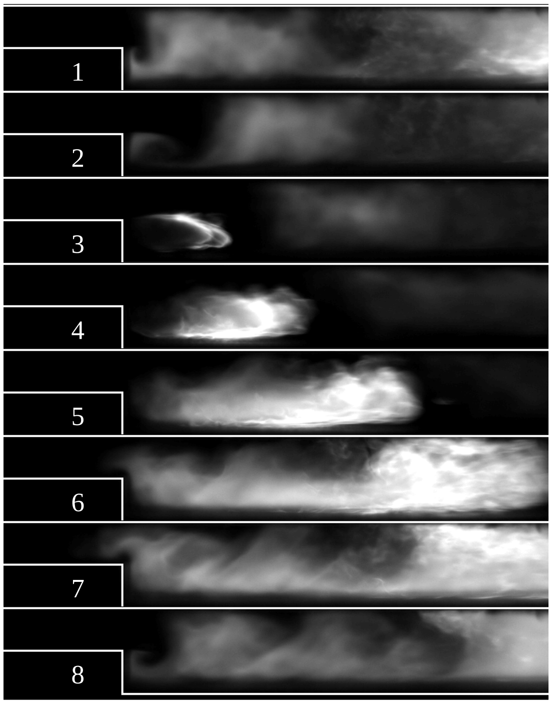

Figure 3-9: Sequential flame images recorded at Re=8500, $\bar{\phi}$=0.80. The resonant frequency is 35 Hz. The time between the frames is 4.1 ms.

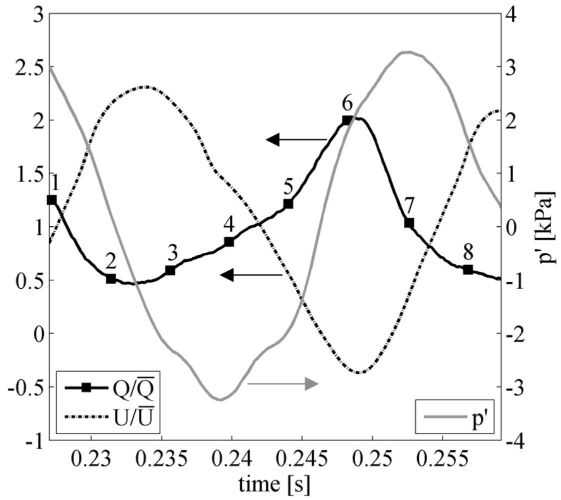

Figure 3-10: Simultaneous heat-release rate, velocity and pressure measurements covering the same time period as the images shown in Fig. 3-9.

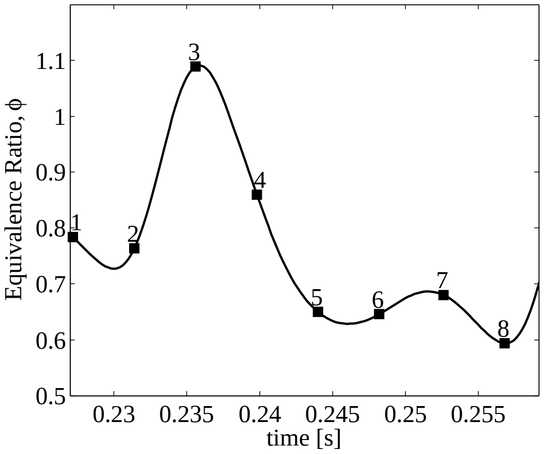

Figure 3-11: Equivalence ratio arriving at the step covering the same time period as the images shown in Fig. 3-9.

Re=8500 and $\bar{\phi}$ =0.70

Next, I reduced the value of the mean equivalence ratio to 0.70, close to the lean blowout limit. In Fig. 3-8(d), I showed that the amplitude of the pressure oscillations were different in every cycle under these operating conditions. For this reason, I inves-

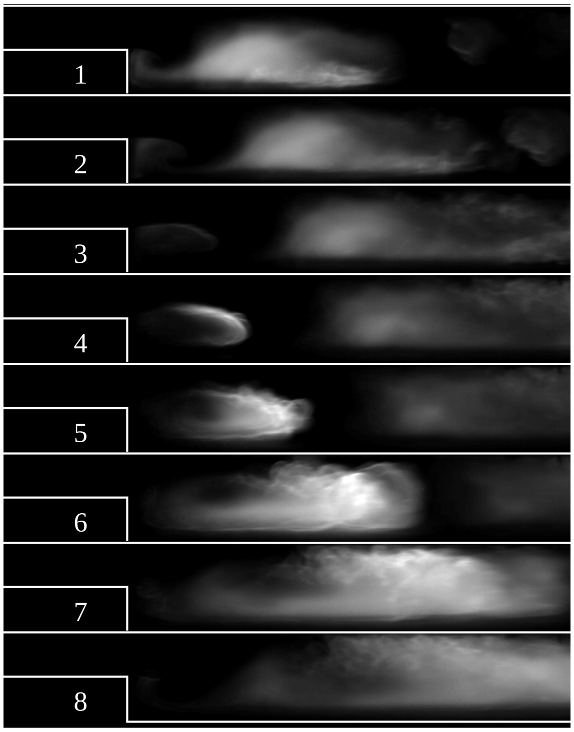

Figure 3-12: Sequential flame images recorded during a cycle showing positive coupling between the heat-release rate and the pressure. Re=8500, $\bar{\phi}$=0.70. The resonant frequency is 36 Hz. The time between the frames is 4.1 ms.

tigate the combustion dynamics of two different cycles showing positive or negative coupling between the pressure and the heat-release rate, caused by the presence of ϕ'.

Cycle 1: Positive coupling

In Fig. 3-12, I show a sequence of flame images during a cycle in which the coupling between the heat-release rate and the pressure is positive. Figure 3-13 shows the simultaneous heat-release rate, velocity and pressure measurements, and Fig. 3-14 shows ϕ_{step} calculated by solving the convection-diffusion equation numerically covering the same time period as the images shown in Fig. 3-12. The diffusion coefficient, $D = 0.01$ m^2/s, as suggested before in Section 3.1.1. The resonant frequency is 36 Hz, which corresponds to the 1/4 wavemode of the combustor.

A vortex forms at the recirculation zone downstream of the step close to the moment of maximum flow acceleration (1). At this instant ϕ_{step} is around 0.72. As

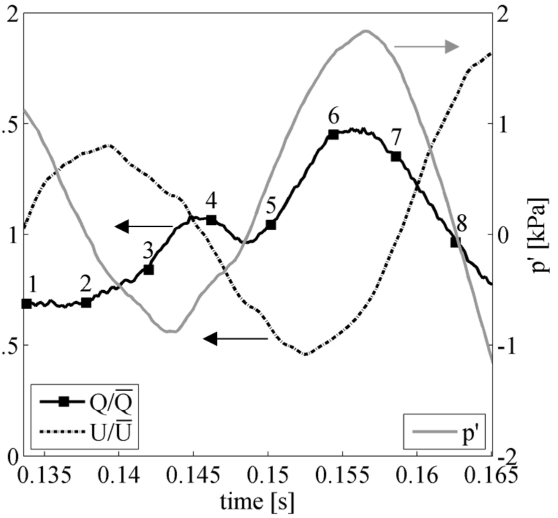

Figure 3-13: Simultaneous heat-release rate, velocity and pressure measurements covering the same time period as the images shown in Fig. 3-12.

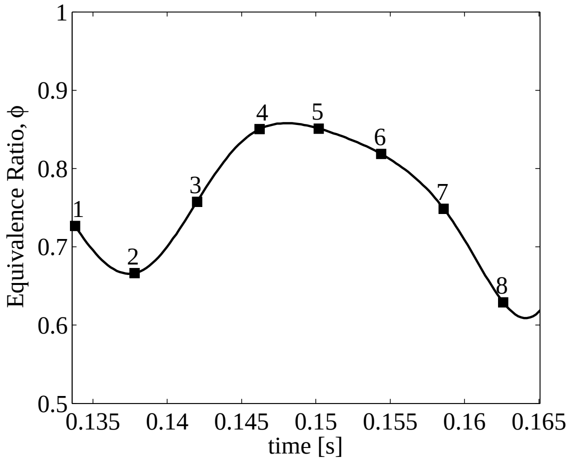

Figure 3-14: Equivalence ratio arriving at the step covering the same time period as the images shown in Fig. 3-12.

the inlet velocity increases, the vortex convects downstream, and ϕ_{step} drops to 0.66 (2). During instants 1 and 2, the heat-release rate is around its minimum value, and the burning from the previous cycle is concentrated in a small zone just downstream of the vortex. Next, ϕ_{step} starts rising. The heat-release rate rises as the area of the flame from the previous cycle increases (3). The burning rate near the step is low, because the equivalence ratio of the reactants entrained by the vortex until this moment is low. Next, when ϕ_{step} reaches its maximum value of around 0.85, the reactant mixture entrained by the vortex starts burning intensively around it. As a result, heat-release rate increases. After this moment, ϕ_{step} starts to drop. Between instants 4 and 5, the heat-release rate drops slightly, because the burning from the previous cycle is completed. Following this moment, the combustion generated volume expansion causes the vortex and the flame wrapped around it to rapidly convect downstream, while the vortex expands towards the upper wall of the combustor. The flame area increases, causing the heat-release rate to increase steeply (5, 6). Note that the equivalence ratio of the mixture in the vicinity of the vortex, ϕ_{vor}, convects downstream together with the vortex by the local flow velocity. Therefore, close to the location of the intense burning, ϕ_{vor} is nearly constant, although ϕ_{step} decreases. As the vortex touches the upper wall of the combustor, the flame area and the heat-release rate reach their maxima between instants 6 and 7. At that moment, the flow velocity is at its minimum value. As the velocity rises again, the heat-release rate starts to drop (8) and a new vortex is formed when the flow accelerates at its maximum rate. The pressure and heat-release rate are in-phase, resulting in a positive feedback. This causes the pressure and velocity amplitudes to increase in the next cycle.

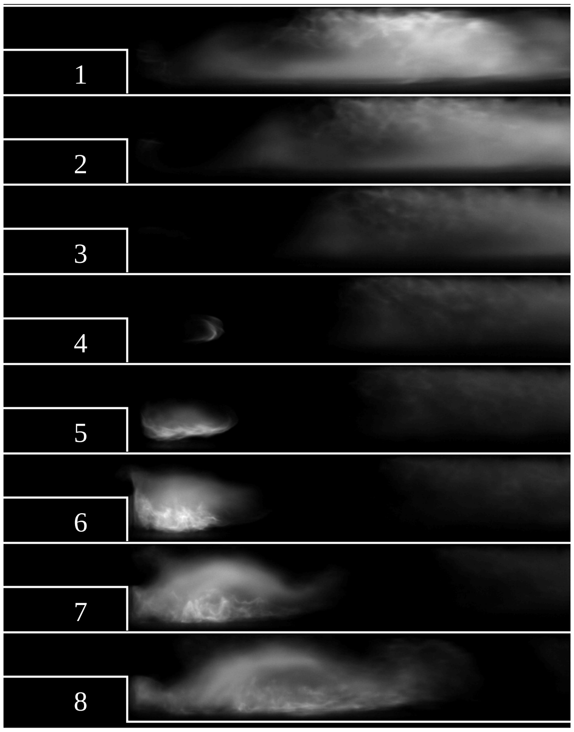

Figure 3-15: Sequential flame images recorded during a cycle showing negative coupling between the heat-release rate and the pressure. Re=8500, $\bar{\phi}$ =0.70. The resonant frequency is 36 Hz. The time between the frames is 4.1 ms.

Cycle 2: Negative coupling

Now, I investigate the combustion dynamics observed at the same operating conditions during a cycle immediately after the one described above. In Fig. 3-15, I show a sequence of flame images, which show negative coupling between the heat-release rate and the pressure. Figure 3-16 shows the simultaneous heat-release rate, velocity and pressure measurements, and Fig. 3-17 shows ϕ_{step} calculated by solving the convection-diffusion equation numerically covering the same time period as the images shown in Fig. 3-16. The diffusion coefficient, $D = 0.01$ m^2/s. The resonant frequency is 36 Hz, which corresponds to the 1/4 wavemode of the combustor.

This cycle again begins when the wake vortex forms, corresponding to the moment of maximum flow acceleration (1). At this moment, ϕ_{step}=0.72 and dropping. Burning from the previous cycle continues near the downstream edge of the flame image.

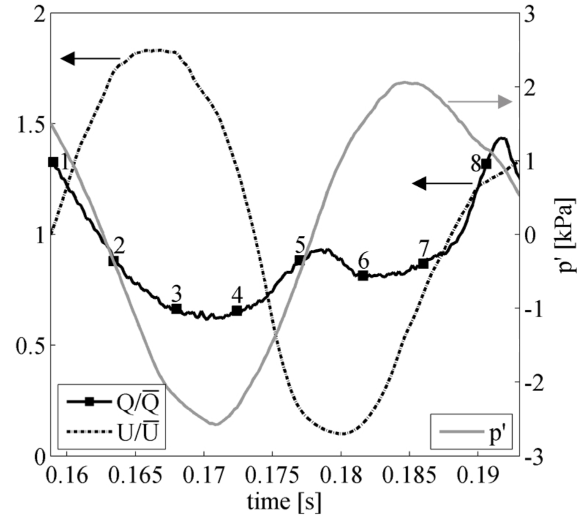

Figure 3-16: Simultaneous heat-release rate, velocity and pressure measurements covering the same time period as the images shown in Fig. 3-15.

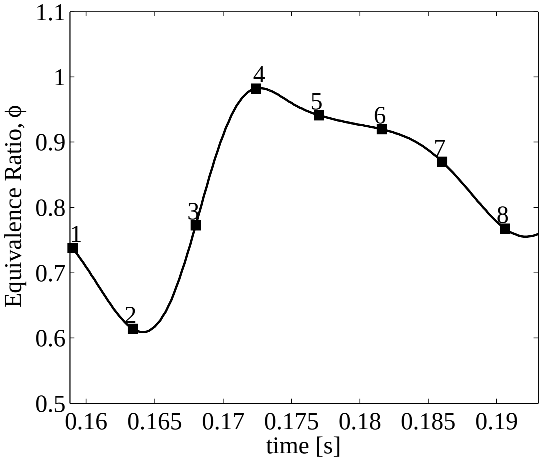

Figure 3-17: Equivalence ratio arriving at the step covering the same time period as the images shown in Fig. 3-15.

Therefore, the heat-release rate is still above its mean value, but decreasing. As the inlet velocity increases, ϕ_{step} reaches its minimum value of around 0.60. At instant 3, the heat-release rate is at its minimum value, the flow velocity is maximum, and ϕ_{step} is around 0.75. Between instants 2 and 3, because the equivalence ratio of the mixture entrained by the vortex is very lean, the flame locally blows out near the step, which is evident from the zero light intensity captured by the camera near the step at instant 3. After this moment, ϕ_{step} reaches its maximum value of near stoichiometry. Intense burning is initiated at the downstream surface of the vortex towards the lower wall of the combustor, when the mixture with sufficient equivalence ratio re-ignites (4). Immediately downstream of the vortex no burning takes place. In this cycle, the burning is concentrated within a small zone downstream of the step, along the height of the combustor, and is intense at the bottom surface of the vortex (5–7). Consequently, the vortex does not convect rapidly in the streamwise direction, because the combustion generated volume expansion effects are only significant in the vertical direction. Therefore, the flame area does not increase rapidly unlike the cycle described previously; the increase in the heat-release rate is not steep. The heat-release rate decreases slightly after instant 5, because the burning from the previous cycle is completed. Between instants 7 and 8, a new vortex is formed near the step, while ϕ_{step} is close to its mean value of 0.70 and decreasing. The high inlet velocity pushes the flame downstream, causing the flame area to increase steeply. As a consequence, the heat-release rate is close to its maximum value around instant 8. In this cycle, the heat-release rate significantly lags the pressure oscillations. Therefore, there is negative-coupling between the heat-release rate and the acoustics. This causes the amplitude of the acoustic oscillations to decrease in the next cycle.

3.1.4 Discussions

The equivalence ratio oscillations formed at the fuel injector location, ϕ'_{inj}, are inversely proportional to the flow velocity: $\phi'_{inj}(t)\ \alpha\ 1/U(t)$. The convective delay between ϕ'_{inj} and the equivalence ratio oscillations arriving the step, ϕ'_{step}, is approximately $\tau_{conv} = L_{inj}/\bar{U}$. Note that as the amplitude of the velocity oscillations increase to cause flow reversal, this approximation is less accurate. The amplitude of the oscillations drop while they are convected as a result of the effect of the diffusion process. Thus, $\phi'_{step}(t) = \alpha\phi'_{inj}(t - \tau_{conv})$, where $\alpha \leq 1$ [17, 19]. At Re=8500 and Re=6500, $\tau_{conv} = 46.0$ ms and $\tau_{conv} = 60.2$ ms, respectively. Note that $\bar{\phi}$ has a negligible impact on τ_{conv} at constant Re. The velocity oscillates at 36 Hz; therefore, $\tau_{conv} = 1.7T$ at Re=8500, and $\tau_{conv} = 2.2T$ at Re=6500, where T is the oscillation period. This shows that ϕ_{step} at Re=8500 is out-of-phase with ϕ_{step} at Re=6500. Investigating Figs. 3-10 and 3-11 carefully, I observe that ϕ_{step} at Re=8500 is out-of phase with the pressure oscillations. As a consequence, ϕ_{step} at Re=6500 is in-phase with the pressure oscillations. If the flame area did not oscillate, i.e. no flame vortex-interactions, the heat-release rate was expected to be proportional to ϕ_{step}. Therefore, the flame was expected to be stable at Re=8500, and unstable at Re=6500 [19]. However, at both values of Re, OASPL is large across the entire range of $\bar{\phi}$, when there is equivalence ratio oscillations as shown in Fig. 3-6. This shows that the dominant mechanism governing the combustion dynamics is the flame-area oscillations generated by the flame-vortex interaction mechanism, which is also demonstrated in Ref. [6] performing a linear analysis. The equivalence ratio oscillations cause oscillations in the heat-release rate flux away from the location of the vortex, which is a secondary mechanism impacting the combustion dynamics.

In a cycle when there is positive coupling between the heat-release rate and the pressure oscillations, combustion dynamics in that cycle are very similar whether the equivalence ratio oscillates or not. The velocity oscillations cause an unsteady vortex to be shed from the recirculation zone behind the step. The vortex entrains the unburned mixture flowing from the step. The entrained mixture burns intensively in the vicinity of the wake vortex. The equivalence ratio of the mixture in the vicinity of the vortex when the burning initiates, ϕ_{vor}, convects together with the vortex by the local flow field, which is strongly dependent on the combustion generated volume expansion. Therefore, close to the location of the intense burning, ϕ_{vor} is nearly constant. The upstream end of the flame is anchored near the step, while the downstream end, where the burning is intense, is wrapped around the wake vortex. Therefore, as the vortex is convected, the total flame-area oscillates, which cause fluctuations in the heat-release rate.

Investigating the flame images and the corresponding pressure measurements carefully, I observe that the reactants entrained by the vortex starts to burn extensively during the first half of the cycle, before the pressure starts to rise from its minimum value. Based on this observation, I estimate ϕ_{vor} as:

$$\phi_{vor} = \max[\phi_{step}(t)] \tag{3.3}$$

when $u'(t) \geq 0$. Without ϕ', the combustor operates under three distinct operating modes; unstable, quasi-stable, and stable as discussed before. The equivalence ratio at the quasi-stable to unstable transition, $\phi_{\mathrm{qs-u}} = 0.75$; and the equivalence ratio at the stable to quasi-stable transition, $\phi_{\mathrm{s-qs}} = 0.70$; independent of Re. If (i) $\phi_{vor} \geq \phi_{\mathrm{qs-u}}$, I expect the heat-release rate to be in-phase with the pressure oscillations and oscillate with large amplitude, generating high amplitude pressure oscillations, which is around 160 dB; (ii) $\phi_{\mathrm{s-qs}} \leq \phi_{vor} \leq \phi_{\mathrm{qs-u}}$, I expect the heat-release rate to be in-phase with the pressure oscillations and oscillate with small amplitude, generating low amplitude pressure oscillations, which is around 148 dB; and (iii) $\phi_{vor} < \phi_{\mathrm{s-qs}}$, I expect the heat-release rate to be almost steady resulting in negligible pressure oscillations, which is around 135 dB. Note that it is not possible to satisfy $\phi_{vor} < \phi_{\mathrm{s-qs}}$ at any operating condition as long as $\bar{\phi}$ at the lean blowout limit is greater than $\phi_{\mathrm{s-qs}}$. Therefore, the combustor never operates under the stable mode with equivalence ratio oscillations. Moreover, as shown in Fig. 2-3(b), the equivalence ratio measured 2 cm downstream of the step at some spanwise locations (≈ 0.80) is higher than the mean equivalence ratio (≈ 0.70), which might contribute to generating strong thermoacoustic instability even at very lean mean equivalence ratios.

Although the dominant mechanism governing the combustion dynamics is the flame-area oscillations generated by the flame-vortex interactions, the equivalence ratio oscillations also have secondary effects by causing the heat-release flux to oscillate away from the vortex.

(i) The phase between ϕ_{step} and the pressure oscillations is dependent on τ_{conv}. If ϕ_{step} is in-phase with the pressure oscillations, e.g. at Re=6500, the heat-release flux near the step is in-phase with the pressure oscillations, contributing to the instability.

(ii) With ϕ', the reactants start to burn intensively at different locations as shown before (around the vortex, or near the bottom surface of the vortex), causing significant differences in combustion dynamics. Figure 3-6 shows that when the equivalence ratio oscillates, at Re=8500, the OASPL drops when $\bar{\phi} < 0.80$, and remains nearly the same as $\bar{\phi}$ is reduced further towards the lean blowout limit. When $\bar{\phi} \geq 0.80$, the pressure amplitude is large, causing flow reversal. Although the instantaneous equivalence ratio during a cycle drops below the lean blowout limit; because of the flow reversal the flame moves upstream of the step, which helps preventing the flame to blow out near the step as shown in Fig. 3-9, image 7. When $\bar{\phi} < 0.80$, the flow no longer reverses. If the equivalence ratio amplitude is large enough, the flame blows out locally near the step (see Fig. 3-17, image 3). Because of the local blowout near the step, the reactants entrained by the vortex re-ignite near the hot lower wall of the combustor towards the bottom surface of the vortex, when ϕ_{step} is close to its maximum value. When the burning starts near the bottom surface of the vortex, the convection of the vortex in the streamwise direction is limited because of the negligible volume expansion in that direction. As a result, the flame area grows slowly, the heat-release rate lags the pressure oscillations, providing negative feedback to the acoustic oscillations as explained before. This causes the amplitudes of the acoustic oscillations to decrease. As the amplitudes of the oscillations decrease, the minimum value of ϕ_{step} during a later cycle increases, preventing the flame to blow out (see Fig. 3-14). As a result, the mixture starts burning quickly around the vortex, allowing the flame area to grow quickly, which provides strong positive heat release-acoustic coupling, increasing the pressure and velocity amplitudes significantly. Because the velocity amplitude increases significantly, ϕ_{step} again drops to very lean values during parts of the cycle causing local flame blowout near the step during a later cycle. Therefore, the combustion dynamics are driven by self-sustained variations in the heat release-acoustic coupling in each cycle governed by the local flame blowout near the step. As a result of this mechanism, the amplitude of the pressure oscillations change in every cycle. Figure 3-6 shows that the value of ϕ below which the flame blows out when there is no ϕ' is 0.65 at both Re=8500 and Re=6500. Therefore, I expect the equivalence ratio at the lean blowout limit, $\phi_{LBO} \approx 0.65$.

$$\phi_{min} = \min[\phi_{step}(t)] \tag{3.4}$$

If $\phi_{min} < \phi_{LBO}$, and there is no flow reversal, i.e. $u'(t)/\bar{U} > 0$, the combustion dynamics are expected to exhibit variations in every cycle.

At Re=6500, the OASPL is high (156 dB) even close to the lean blowout limit as shown in Fig. 3-6. At this Re, because ϕ_{step} couples positively with the pressure oscillations, the instability is stronger. Because the velocity oscillations are stronger, and the mean velocity is lower in this case compared to the case when Re=8500, the flow reversal is stronger. Because of this, the flame does not blowout near the step for $\bar{\phi} \geq 0.72$. When $\bar{\phi} < 0.72$, $\phi_{min} < \phi_{LBO}$ long enough in some cycles during part of the cycle causing local blow out of the flame near the step during some cycles as explained above, resulting in variations in pressure amplitude in each cycle.

(iii) When $\bar{\phi}$ is dropped below 0.70, ϕ_{min} drops significantly below ϕ_{LBO} during a cycle, not allowing the flame to re-ignite. Therefore, $\bar{\phi}$ at the lean blowout limit is higher when the equivalence ratio arriving at the step oscillates.

3.2 Summary

In this chapter, I investigated the impact of equivalence ratio oscillations on combustion dynamics in a backward-facing step combustor. Simultaneous pressure, velocity, and heat-release rate and equivalence ratio measurements and high-speed video from the experiments were used to identify and characterize several distinct operating modes. When equivalence ratio oscillations were absent, I observed three distinct operating modes of the combustor depending on the equivalence ratio. When equivalence ratio oscillations were present, I showed that independent of the phase between the equivalence ratio arriving at the flame and the pressure oscillations, the unsteady interactions between the flame and the vortex were still dominant, because the local equivalence ratio near the vortex during burning is large enough to drive the unstable dynamics. Therefore, the combustion dynamics is primarily governed by the flame-vortex interactions. However, the equivalence ratio oscillations have secondary effects on the dynamics: (i) When there is no flow reversal, the amplitude of the acoustic oscillations change in each cycle governed by the local flame blowout near the step; (ii) when the equivalence ratio arriving at the flame is in-phase with the pressure oscillations, stronger heat-release rate oscillations are generated at the entire range of mean equivalence ratios, further contributing to the instability; and (iii) the mean equivalence ratio at the lean blowout limit is higher compared to the dynamics driven by the flame-vortex interactions alone.

These results suggest that the equivalence ratio oscillations are undesirable when the combustion dynamics are primarily governed by the flame-vortex interactions. In order to eliminate the equivalence ratio oscillations oxidizer-fuel premixing strategies allowing for longer mixing time or faster mixing rate should be developed.

Chapter 4

Mitigation of Thermoacoustic Instability Utilizing Steady Air Injection Near the Flame Anchoring Zone

In Chapters 2 and 3, I systematically investigated the combustion dynamics in the backward-facing step combustor driven only by the flame-vortex interactions, and the combined action of the flame-vortex interactions and the equivalence ratio oscillations, respectively. The results suggest that when the equivalence ratio arriving at the flame oscillates, it is not possible to operate the combustor in the stable mode independent of the operating conditions. Because of this reason, in this chapter, I place the fuel injector 93 cm upstream of the step to eliminate the equivalence ratio oscillations. Note that without control, the flame is stable only at narrow range of equivalence ratios near the lean blowout limit as shown in Fig. 2-9.

Active combustion control strategies that modulates the fuel flow rate [44–51], or air flow rate [52] can be applied to suppress thermoacoustic instabilities in premixed combustors by disrupting the coupling mechanisms that support these instabilities. While effective in suppressing the instabilities, these approaches require high speed actuators and add significant complexity to the design of the combustors. For this reason, developing simple, passive control strategies that directly impact the flame anchoring zone with minimal complexity are desirable.

The potential for suppressing thermoacoustic instability by injecting steady air [49, 64, 65], or by injecting open-loop, low-frequency modulated air [66] near the flame anchoring zone has been shown in the past. In these approaches, the secondary air flow is thought to change the velocity field and disrupt the flame-vortex interaction, which has been shown to be the primary instability mechanism in dump combustors [67]. In this chapter, I inject steady air flow near the flame anchoring zone through choked micro-diameter holes. The small hole diameter allows for large velocities with low air flow rates. I perform a systematic experimental study with extensive range of operating conditions, which involves using two different configurations of secondary air injection in an atmospheric pressure backward-facing step combustor. Secondary air can be injected from 12, 0.5 mm diameter holes drilled along the combustor width in the cross-stream direction 5 mm upstream of the step, or in the streamwise direction near the corner of the step. These two configurations are referred to as the *normal* microjets and the *axial* microjets, respectively. Their positions are shown schematically in Fig. 4-1. The flow rate of the secondary air is controlled using a Sierra C100M mass flow controller, which allows a maximum air flow rate of 4.3 g/s.

The effectiveness of both of these configurations in mitigating the instability are analyzed at different fuel compositions, equivalence ratios and inlet temperatures. The Reynolds number is fixed at 6500, which is based on the step height, and the primary air flow rate. The secondary air temperature is always the same as the inlet temperature and adjusted using an Osram Sylvania 4kW in-line electric heater, with on/off temperature controller. Previous studies have shown that enriching hydrocar-

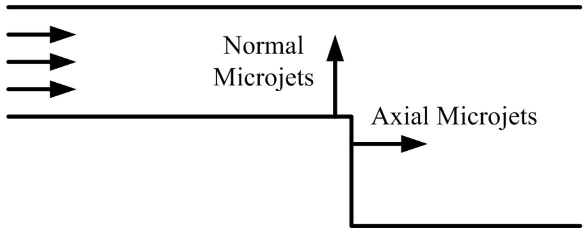

Figure 4-1: The microjet air injection configurations seen from the side of the combustor with the fuel/air mixture entering from the left.

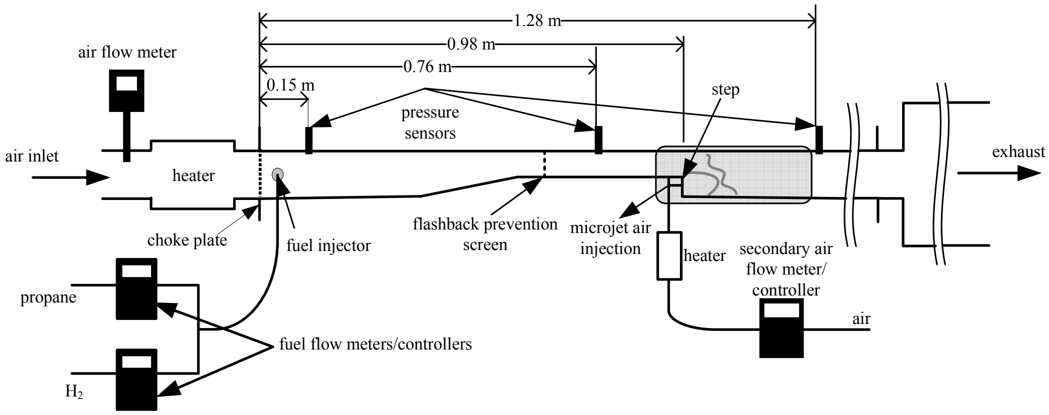

Figure 4-2: Schematic diagram of the backward-facing step combustor modified to allow for microjet air injection.

bon fuels with small amounts of hydrogen significantly enhances the lean blowout limit of the combustor [31–33, 68]. For this reason, I also add small amounts of hydrogen to the primary fuel, in this case propane. The data obtained with no secondary air injection are referred to as the baseline (without passive control) and explained extensively in Chapter 2. In order to understand the role of air injection in suppressing the instabilities, flame images are recorded using a high speed video camera.

The backward-facing step combustor with the modifications to allow for the secondary air injection is shown in Fig. 4-2.

4.1 Combustion dynamics with normal microjets

I performed experiments to investigate the effect of secondary air injection through normal microjets on the combustion dynamics. I measured the pressure amplitude and examined the flame images at different fuel compositions, inlet temperatures, equivalence ratios and microjet flow rates.

4.1.1 Pressure Measurements

In Fig. 4-3, I plot the OASPL as a function of the equivalence ratio based on the main air flow rate at different normal microjet flow rates without hydrogen enrichment and with 50% by volume hydrogen enrichment. The temperatures of the inlet mixture and the secondary air flow are 300 K. The main air flow rate is approximately 17.5 g/s. Without hydrogen enrichment, normal microjets destabilize the unstable dynamics ($\phi > 0.77$), causing near 4 dB increase in the OASPL. The quasi-stable dynamics is stabilized with normal microjets, reducing the OASPL by a maximum of 12 dB to the values corresponding to the stable mode. The stable mode is not impacted by normal microjets. When 50% by volume hydrogen is added to propane, there is reduction in the OASPL compared to the baseline when $\phi > 0.68$. At equivalence ratio of 0.80, this reduction is near 18 dB, the OASPL is close to the values observed in the quasi-stable regime. When the equivalence ratio is reduced below 0.68, the normal microjets destabilize the unstable dynamics further, similar to the cases without hydrogen enrichment. Again, normal microjets stabilize the quasi-stable dynamics and do not impact the stable dynamics with 50% by volume hydrogen enrichment.

In order to investigate the effect of normal microjets further, I plot the combustor's frequency response in Fig. 4-4 corresponding to the cases in Fig. 4-3. These figures show the amplitude of pressure oscillations as a function of the frequency for the ranges of equivalence ratios in Fig. 4-3. Without hydrogen enrichment, there is no

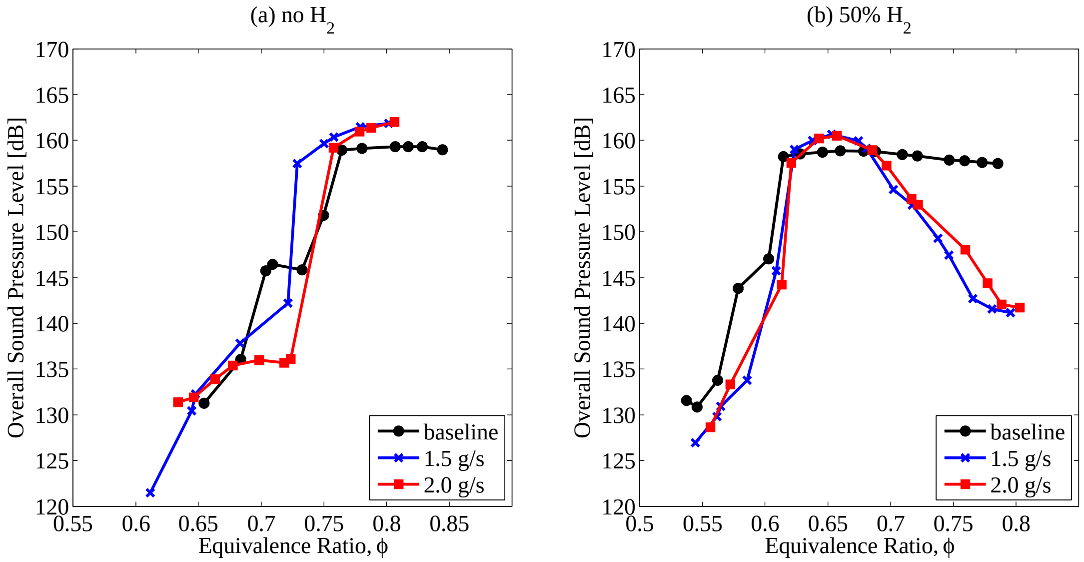

Figure 4-3: OASPL as a function of equivalence ratio at different normal microjet flow rates (a) without hydrogen enrichment and (b) with 50% by volume hydrogen enrichment. The temperatures of the inlet mixture and the normal microjets are 300 K.

change in the resonant frequency when normal microjets are introduced. The resonant frequency is around 40 Hz in all cases and corresponds to the 1/4 wavemode of the combustor. With 50% by volume hydrogen enrichment, when the equivalence ratio is greater than 0.76, the OASPL is very low which corresponds to the plateau observed in Fig. 4-3(b). The dominant frequencies in these cases are 120 Hz and 175 Hz. At these operating conditions the normal microjets are able to suppress the dynamics.

Next, I increase the temperatures of the inlet mixture and the secondary air flow to 600 K. The main air flow rate in this case is around 28.5 g/s. Figure 4-5 shows the OASPL as a function of the equivalence ratio based on the main air flow rate at different normal microjet flow rates without hydrogen enrichment or with 50% by volume hydrogen enrichment. As the equivalence ratio increases from its value where the transition to quasi-stable operating mode takes place, i.e. $\phi \sim 0.55$ without hydrogen enrichment and $\phi \sim 0.45$ with 50% by volume hydrogen enrichment, first the normal microjets destabilize the unstable dynamics further, then the OASPL drops to the values corresponding to the quasi-stable dynamics just before suddenly

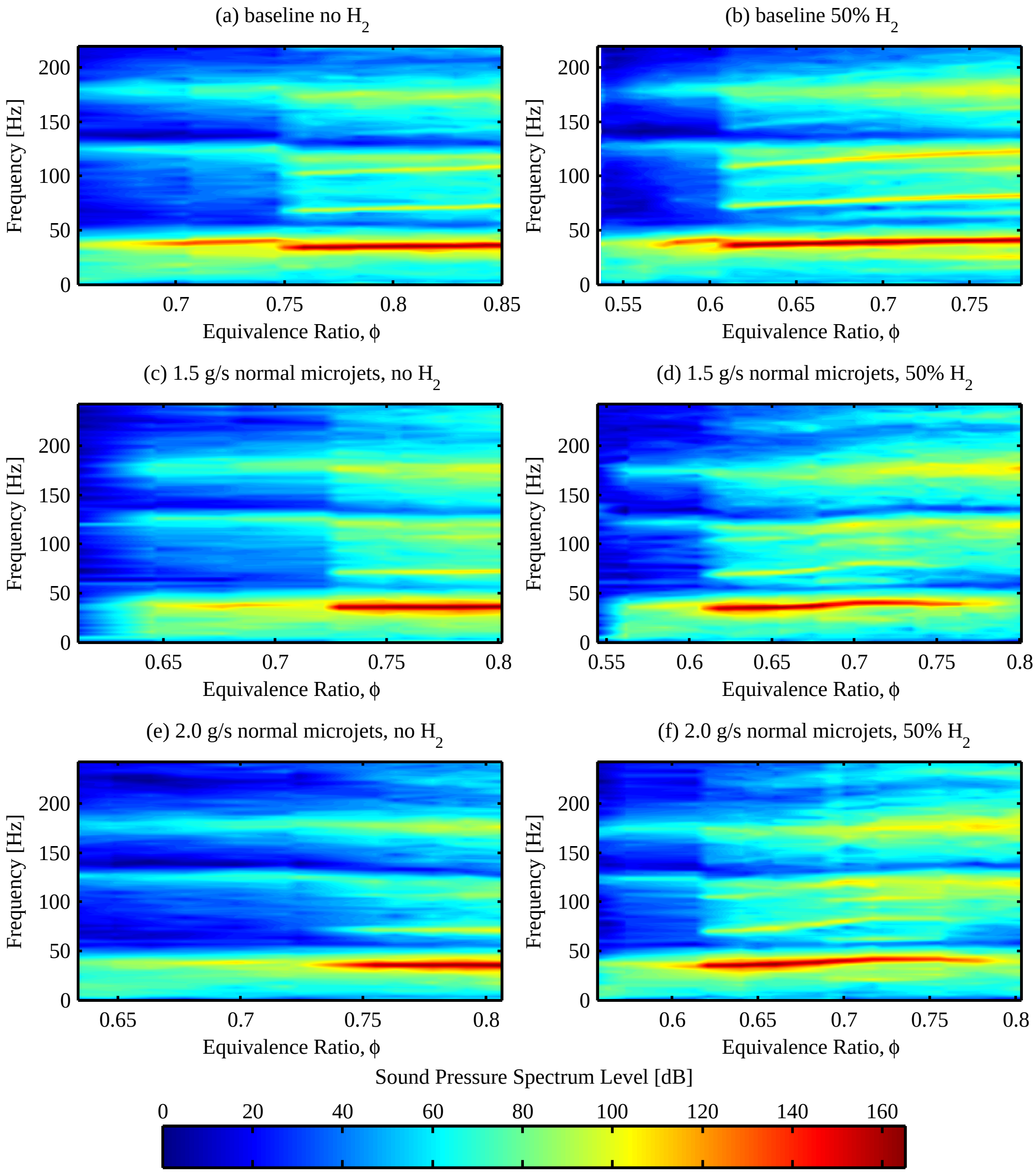

Figure 4-4: Sound pressure spectrum level maps as a function of equivalence ratio for the same cases in Fig. 4-3.

increasing to higher values, which suggests excitation of a higher acoustic mode. The equivalence ratio at the transition to the higher acoustic mode is lower with normal microjets compared to the baseline. Figure 4-5 also shows that the normal microjets stabilize the dynamics in the quasi-stable regime and have no impact on the dynamics in the stable regime similar to the behavior observed in Fig. 4-3.

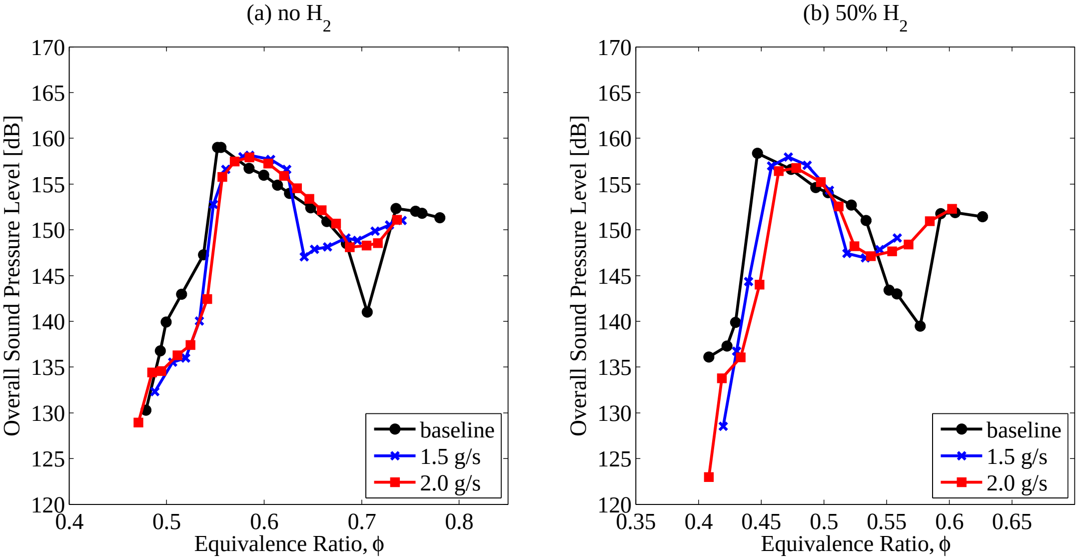

Figure 4-5: OASPL as a function of equivalence ratio at different normal microjet flow rates (a) without hydrogen enrichment and (b) with 50% by volume hydrogen enrichment. The temperatures of the inlet mixture and the normal microjets is 600 K.

I plot the combustor's frequency response in Fig. 4-6 corresponding to the cases in Fig. 4-5. Without normal microjets, at higher equivalence ratios, the acoustic mode around 132 Hz is excited. This acoustic mode corresponds to the 5/4 wavemode of the combustor as shown in Section 2.2.2. However, with the normal microjets, the excited higher acoustic mode resonates around 85 Hz, which is the 3/4 wavemode of the combustor. The response of the 7/4 wavemode around 200 Hz is also significant. The normal microjets damp/stabilize the acoustic mode around 132 Hz, as a result allowing the 85 Hz mode to be excited although in that case the flame is close to a pressure node as mentioned before. Since the excited resonant frequency is lower with normal microjets, the equivalence ratio at the transition is also lower compared to the baseline case. It is also interesting to observe that without hydrogen enrichment, the transition equivalence ratio is lower when the microjet flow rate is 1.5 g/s, compared to the microjet flow rate of 2.0 g/s. These observations will become more clear when I extend the theory explained in Section 2.2.4 to the 3/4 wavemode.

Next, I investigate the flame images recorded at different operating conditions

(a) baseline no H_2 (b) baseline 50% H_2

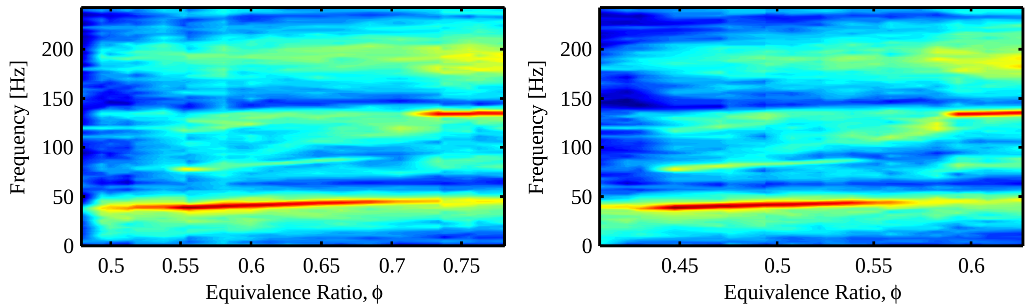

(c) 1.5 g/s normal microjets, no H_2 (d) 1.5 g/s normal microjets, 50% H_2

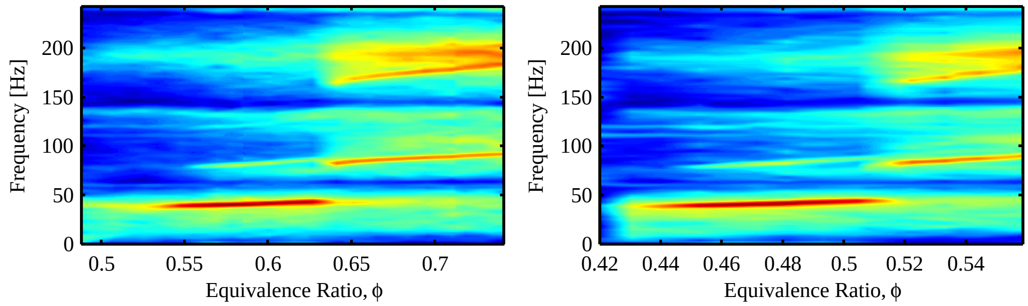

(e) 2.0 g/s normal microjets, no H_2 (f) 2.0 g/s normal microjets, 50% H_2

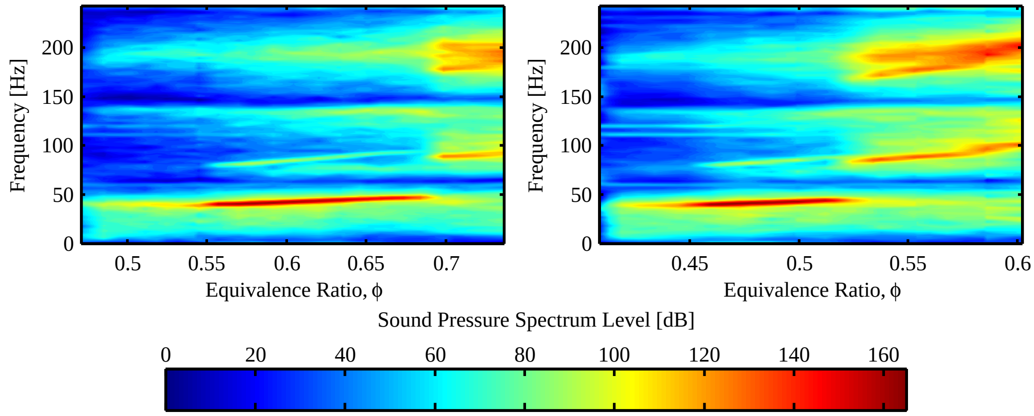

Figure 4-6: Sound pressure spectrum level maps as a function of equivalence ratio for the same cases in Fig. 4-5.

and secondary air flow rates to examine the impact of normal microjets on the flame-vortex interaction mechanism.

4.1.2 Flame Images

In order to distinguish between the dynamics at different operating conditions with passive control using normal microjets, I examine the flame images extracted from high speed videos of different operating modes and describe corresponding unsteady pressure, and heat-release rate measurements.

First, a typical operating condition when the normal microjets are ineffective in stabilizing the flame is investigated. In Fig. 4-7, a sequence of flame images is shown, recorded at: ϕ=0.57, without hydrogen enrichment, the temperatures of the inlet mixture and the normal microjets are 600 K, and the secondary air flow rate is 1.50 g/s. Figure 4-8 shows simultaneous heat-release rate and pressure measurements covering the same time period as the images shown in Fig. 4-7. The resonant frequency is 39 Hz, which corresponds to the 1/4 wavemode of the combustor. The images show a typical unstable flame interacting with the large unsteady wake vortex formed at the recirculation zone behind the step (see Section 2.2.3) . The wake vortex is formed (1-2) when the pressure is at its maximum. Since the combustor resonates at the 1/4 wavemode, the velocity oscillations lag the pressure oscillations by 90 degrees (see Fig. 2-22(a)); thus, this instant also corresponds to the moment of maximum flow acceleration. The wake vortex convects downstream as the pressure drops while moving towards the upper wall of the combustor (2-5). As a result, a packet of unburned gases forms between the vortex and the flame of the previous cycle. In addition, the heat-release rate is decreasing following the end of the intense burning from the previous cycle. At instant 4, the heat-release rate reaches its minimum, and starts to rise as the unburned mixture trapped inside the vortex begin to burn (4-5). When the vortex reaches the upper wall of the combustor, the heat-release rate reaches its maximum (6-7) value, because the flame area is at its maximum value. Next, the heat-release rate starts to drop, fresh reactants enter the flame anchoring zone and the cycle repeats. Since at this inlet temperature the average velocity is high, flow never reverses, thus the flame never flashes back upstream of the step. The pressure and the heat-release rate are nearly in-phase resulting in the positive feedback between the unsteady heat-release rate and the pressure, driving the instability. The

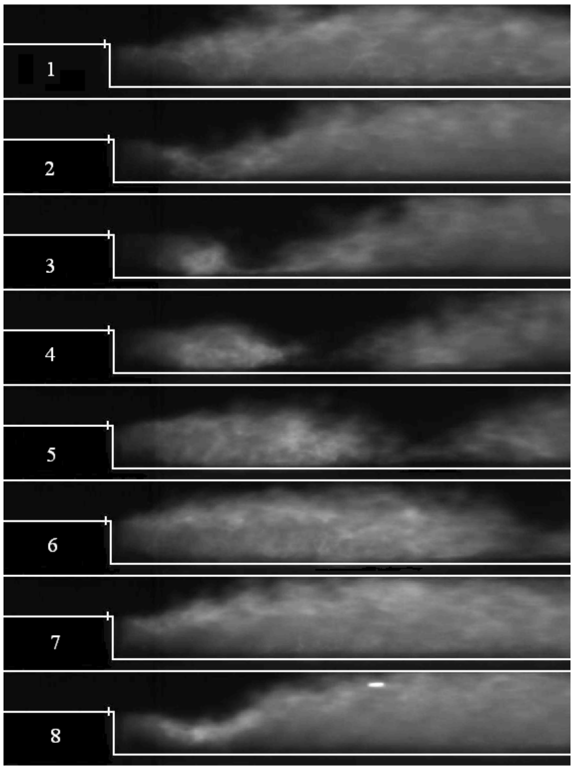

Figure 4-7: Sequential flame images with 1.50 g/s normal microjets, without hydrogen enrichment, at ϕ = 0.57. The temperatures of the inlet mixture and the normal microjets is 600 K. The time between the frames is 4.0 ms.

maximum pressure amplitude is near 1.8 kPa, and the OASPL is around 157 dB.

Next, I investigate the combustion dynamics when the resonant frequency is around 85 Hz corresponding to the 3/4 wavemode of the combustor. Note that the combustor does not couple with the 3/4 wavemode before activating the normal microjets. In Fig. 4-10, a sequence of flame images is shown, recorded at: ϕ=0.72, without hydrogen enrichment, the temperatures of the inlet mixture and the normal microjets are 600 K, and the secondary air flow rate is 1.50 g/s. Figure 4-11 shows simultaneous heat-release rate and pressure measurements covering the same time period as the images shown in Fig. 4-10. In this figure, I plot the pressure oscillations measured at two different locations: (i) 0.15 m downstream of the choke plate and (ii) 1.28 m downstream of the choke plate, which is near the flame location. I observe that the pressure near the choke plate oscillates at 91 Hz, which corresponds to the

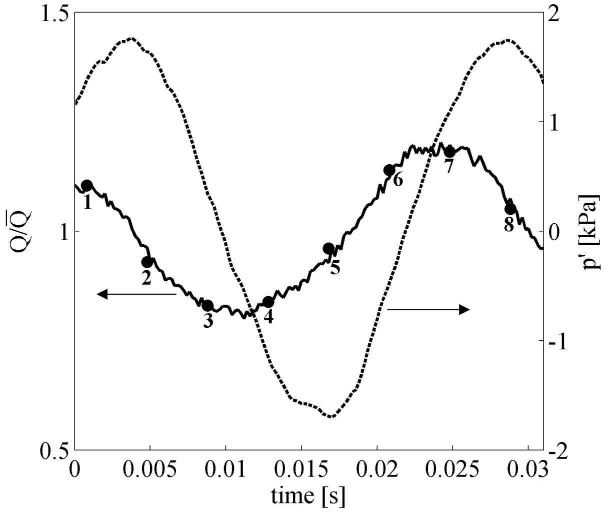

Figure 4-8: Simultaneous pressure and heat-release rate measurements corresponding to the instants in Fig. 4-7.

3/4 wavemode; whereas the pressure near the flame oscillates at 197 Hz, which corresponds to the 7/4 wavemode. This observation is verified in Fig. 4-9, where I plot the sound pressure spectra measured using both pressure sensors.

The heat-release rate measurements and the flame images show that the combustion dynamics are coupled with the 3/4 wavemode of the combustor, although the oscillation frequency near the flame corresponds to the 7/4 wavemode. The combustion dynamics captured in Fig. 4-10 is similar to the dynamics explained above. In this case, the flame is more compact, since it oscillates at a higher frequency. Near instant 1, the wake vortex is formed near the step, when the pressure is at its maximum. At this moment, the acceleration of the flow should also be maximum, suggesting that the velocity lags the pressure by 90 degrees similar to the unstable mode shown in Fig. 2-22. This means that the the flame is upstream of the pressure node. Since the pressure node is close to the flame for the 3/4 wavemode (see Fig. 2-13), the flame might also have been located downstream of the pressure node, which would cause the velocity to lead the pressure by 90 degrees. In that case the vortex should have formed when the pressure was at its minimum value, similar to the high-frequency

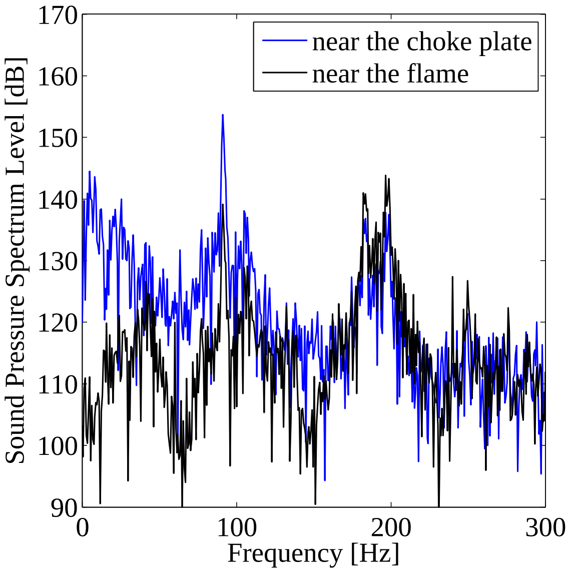

Figure 4-9: Sound pressure spectrum levels measured near the choke plate and near the flame.

unstable mode shown in Fig. 2-22. The wake vortex convects downstream and moves towards the upper wall of the combustor (2-6), forming a reactant packet between the flame wrapped around the vortex, and the vertical flame formed in the previous cycle. Again, when the vortex reaches the upper wall, the heat-release rate reaches its maximum value (7). At that moment, a new vortex forms at the step, and the cycle repeats. The pressure and the heat-release rate are in-phase, driving the instability.

Finally, I investigate the combustion dynamics for a case when normal microjets effectively suppress the instability. In Fig. 4-12, a sequence of flame images is shown, recorded at: ϕ=0.80, with 50% hydrogen enrichment, the temperatures of the inlet mixture and the normal microjets are 300 K, and the secondary air flow rate is 1.50 g/s. Figure 4-13 shows simultaneous heat-release rate and pressure measurements covering the same time period as the images shown in Fig. 4-12. The images show that the dynamics are steady, there is no unsteady interaction between the flame and the unsteady wake vortex. The flame is anchored upstream of the step at the upper wall of the combustor. The heat-release rate is nearly steady and does not

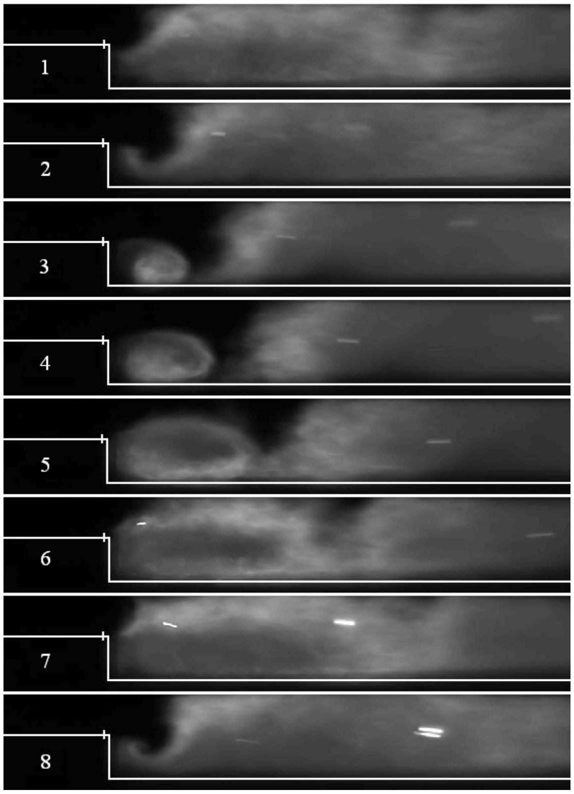

Figure 4-10: Sequential flame images with 1.50 g/s normal microjets, without hydrogen enrichment, at $\phi = 0.72$. The temperatures of the inlet mixture and the normal microjets are 600 K. The time between the frames is 1.8 ms.

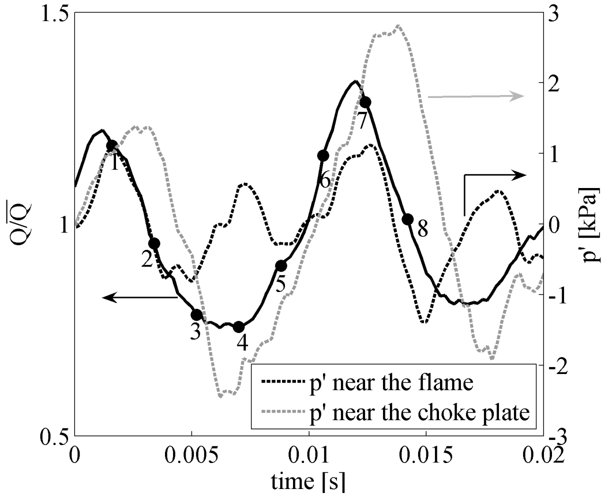

Figure 4-11: Simultaneous pressure and heat-release rate measurements corresponding to the instants in Fig. 4-10.

couple with the pressure oscillations. The pressure oscillation amplitude is around 0.4 kPa. At this operating condition, the burning velocity of the flame is high, and the mean flow velocity is low (because the inlet temperature is atmospheric). Without secondary air injection through normal microjets, at this operating condition the flame detaches from the recirculation zone and flashes back to the inlet channel. However, when the normal microjets are turned on, they prevent the flame from flashing back. Apparently, small scale vortices are generated as a result of the interaction of the microjets with the main flow, and as the microjets hit the upper wall of the combustor, creating a recirculation zone strong enough to anchor the flame at that location [69].

These results show that the normal microjets cannot prevent the formation of the unsteady vortex downstream of the step when the operating conditions correspond to the unstable or the high-frequency unstable modes. However, as the operating conditions are changed so that the burning velocity of the flame increases, the role of the unsteady vortex on the overall dynamics becomes less significant. That is why the OASPL starts to decrease at high equivalence ratios with hydrogen enrichment (see Fig. 4-3). Before activating the normal microjets, when the burning velocity of the flame exceeds a certain threshold, the flame detaches from the step and flashes back upstream. At these operating conditions, when the normal microjets are turned on, instead of the unsteady recirculation zone formed downstream of the step, the flame anchors upstream of the step in the ”new, stable, aerodynamically created” intense recirculation zone formed near the location of microjets, towards the upper wall of the combustor. As a result, the flame dynamics are stabilized.

4.1.3 Extended Theory

When the normal microjets are introduced – except the operating conditions when they suppress the instability – the mechanism of flame-vortex interactions are still

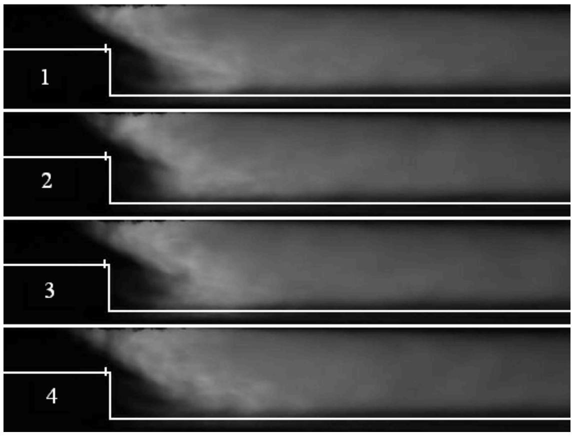

Figure 4-12: Sequential flame images with 1.50 g/s normal microjets, with 50% by volume hydrogen enrichment, at $\phi = 0.80$. The temperatures of the inlet mixture and the normal microjets are 300 K. The time between the frames is 27 ms.

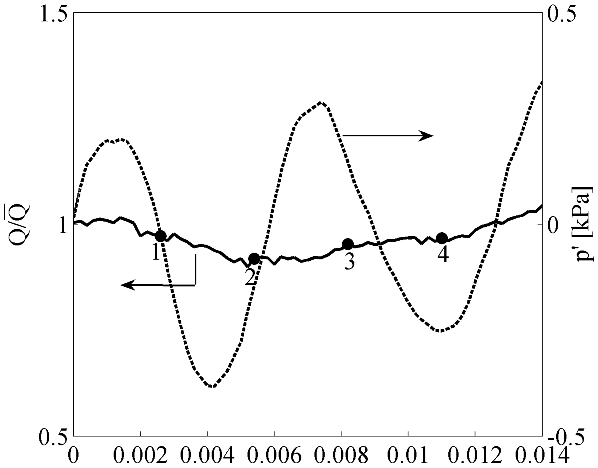

Figure 4-13: Simultaneous pressure and heat-release rate measurements corresponding to the instants in Fig. 4-12.

strong, and governs the combustion dynamics (see Fig. 4-7 and Fig. 4-10). Therefore, I expect this model to be also applicable for the cases with the normal microjets. The theory developed in Section 2.2.4 is extended to predict the operating conditions at which a transition to the 3/4 wavemode resonating around 85 Hz is expected. For convenience, I summarize and generalize the model below.

The time elapsed between the moment of vortex formation and the moment when the vortex reaches the upper wall (moment of maximum heat-release rate) is defined as τ_{vor}. It is assumed that the vortex moves towards the wall predominantly as a result of the expansion velocity in the vertical direction. The expansion velocity is proportional to the heat release parameter $S_T(\rho_u/\rho_b - 1)$ where S_T is the turbulent burning velocity and ρ_u and ρ_b are the unburned and burned mixture densities. Assuming a linear relationship between the turbulent and laminar burning velocities, and taking into account of the strain on the burning velocity, the vertical velocity of the vortex, v_{vor}, is:

$$v_{vor} = \frac{S_c}{c}(\rho_u/\rho_b - 1) \tag{4.1}$$

where S_c is the strained laminar consumption speed of the flame. The constant of proportionality between the expansion velocity and the heat-release parameter, and the proportionality between the turbulent and laminar burning velocities are represented by an arbitrary constant c. Representing the vertical distance between the corner of the step where the vortex forms and the upper wall as H, I obtain $\tau_{vor} = H/v_{vor}$. Substituting v_{vor} from Eq. (4.1):

$$\tau_{vor} = \frac{cH}{S_c(\rho_u/\rho_b - 1)} \tag{4.2}$$

The transitions occur when the pressure and heat-release rate oscillations are in phase, that is $\tau_{pq} = NT$, where N is an integer and T is the oscillation period. Therefore, the transitions between the operating modes take place when (for $N = 1$) :

$$\tau_{vor} = \alpha \frac{1}{f_{res}} \tag{4.3}$$

where $\alpha = 1$ if the velocity lags the pressure by 90 degrees at the flame location (Fig. 2-22(a)), and $\alpha = 3/2$ if the velocity leads the pressure by 90 degrees at the flame location (Fig. 2-22(b)). f_{res} is the resonant frequency. Using Eqs. (4.2) and (4.3), at the transitions between operating modes:

$$S_c(\rho_u/\rho_b - 1)|_{tr} = cHf_{res}/\alpha \tag{4.4}$$

The left-hand side of Eq. (4.4) i.e. the heat release parameter at transition, depends on the operating conditions (ϕ, fuel composition and $\mathrm{T_{in}}$). For a set of operating conditions satisfying Eq. (4.4), the transitions between the operating modes are expected to take place.

Except the case when the normal microjets suppress the instability, the combustion dynamics are still governed by the flame-vortex interaction mechanism even with the normal microjets. The maximum heat-release rate again corresponds to the instant when the vortex reaches the upper wall of the combustor, and the vortex forms at the moment of the maximum acceleration. Therefore, the theory summarized above should also be applicable for the cases with normal microjets. In order to test this hypothesis, in Fig. 4-14, I plot the OASPL as a function of the heat release parameter, $S_c(\rho_u/\rho_b - 1)$, for arbitrarily selected cases from Figs. 4-3 and 4-5. The transition heat release parameters cannot be determined easily using the OASPLs measured by the pressure sensor near the flame, therefore I also plot the OASPLs measured using the pressure sensor near the choke plate. I again use the strain rates of 2000 $\mathrm{s^{-1}}$ and 3000 $\mathrm{s^{-1}}$ for inlet temperatures of 300 K and 600 K, respectively. The heat release parameter is calculated using the equivalence ratio based on the main air flow rate.

Figure 4-14 shows that again all the data are well correlated with the heat release parameter. The observed transitions between different operating modes occur at heat release parameters of around 50 cm/s, 75 cm/s, 110 cm/s and 120 cm/s. Note that the transitions at 75 cm/s and 110 cm/s represent the excitation of the 3/4 wavemode which has not been excited without microjets. Since the flame is very close to a pressure node when 3/4 wavemode is excited as shown in Section 2.2.2, the flame location might be upstream or downstream of the pressure node. If the flame is upstream/downstream of the pressure node, the velocity lags/leads the pressure by 90 degrees. According to the theory represented in Eq. (4.4), the value of α is either 1 or 3/2, respectively, resulting in two distinct transitions when 3/4 wavemode is excited. Using Eq. (4.4), the model predicts the ratio of the heat release parameters between the first transition to 3/4 wavemode and to the unstable transition as:

$$R_{3/4,1} = \frac{2}{3}\frac{f_{3/4,1}}{f_{1/4}} \tag{4.5}$$

where $f_{3/4,1} = 85$ Hz and $f_{1/4} = 39$ Hz from Fig. 4-6(c-d and f), giving $R_{3/4,1} = 1.45$. From the experimental data shown in Fig. 4-14, $R_{3/4,1} = 75/50 = 1.50$. Similarly, the ratio between the heat release parameters at the second transition to the 3/4 wavemode and the unstable transition is:

$$R_{3/4,2} = \frac{f_{3/4,2}}{f_{1/4}} \tag{4.6}$$

where $f_{3/4,2} = 89$ Hz and $f_{1/4} = 39$ Hz. Note that the 3/4 wavemode resonant frequency is slightly higher at the second transition as shown in Fig. 4-6(e). The ratio is calculated as $R_{3/4,2} = 2.28$. From the experimental data shown in Fig. 4-14, $R_{3/4,2} = 110/50 = 2.20$. The model again predicts the transitions with good accuracy and shows that it is applicable as long as the dynamics are governed by the flame-vortex interaction mechanism.

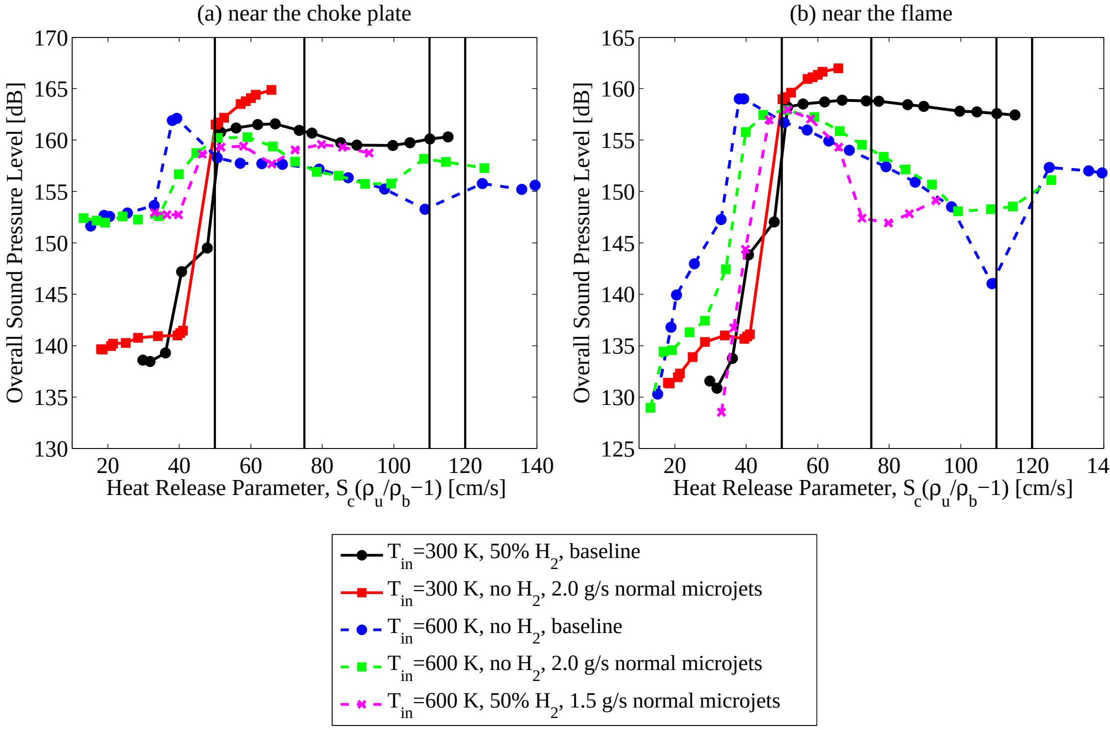

Figure 4-14: OASPL as a function of heat release parameter, $S_c(\rho_u/\rho_b-1)$, at different hydrogen concentrations, inlet temperatures and normal microjet flow rates.

4.2 Combustion dynamics with axial microjets

I also performed experiments to investigate the effect of secondary air injection through axial microjets on the combustion dynamics. I performed pressure measurements and examined the flame images at different fuel compositions, inlet temperatures, equivalence ratios and microjet flow rates.

4.2.1 Pressure Measurements

In Fig. 4-15, I plot the OASPL as a function of the equivalence ratio based on the main air flow rate at different axial microjet flow rates without hydrogen enrichment and with 50% by volume hydrogen enrichment. The temperatures of the inlet mixture and

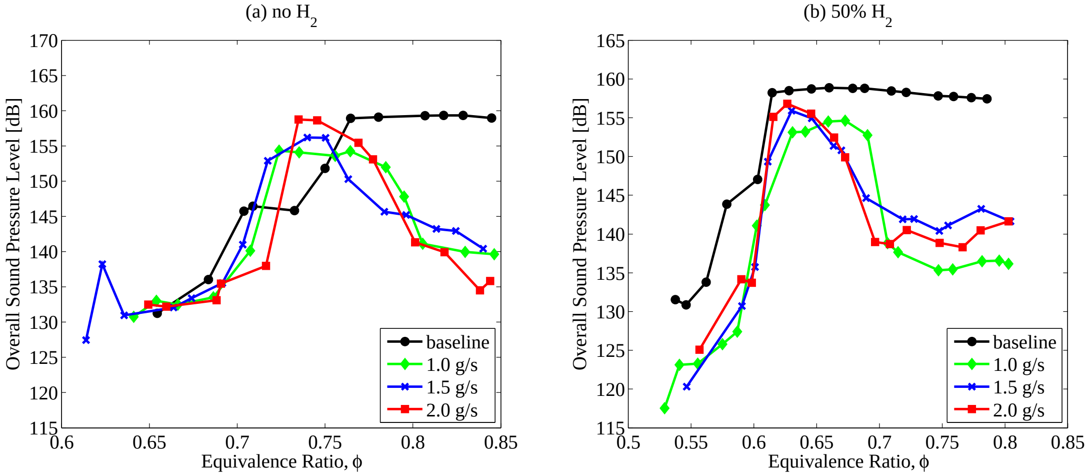

Figure 4-15: OASPL as a function of equivalence ratio at different axial microjet flow rates (a) without hydrogen enrichment and (b) with 50% by volume hydrogen enrichment. The temperatures of the inlet mixture and the axial microjets are 300 K.

the secondary air flow are 300 K. The axial microjets destabilize the quasi-stable flame without hydrogen enrichment, whereas they stabilize the quasi-stable flame when 50% by volume hydrogen is added to propane. The stable flame is not impacted by the axial microjets without hydrogen enrichment, but the OASPL decreases around 7 dB in the stable regime with 50% by volume hydrogen enrichment. The OASPL drops across the entire range of equivalence ratio, however the reduction in the OASPL is maximum and around 20 dB when $\phi > 0.80$ without hydrogen enrichment and $\phi > 0.70$ with 50% by volume hydrogen enrichment.

Figure 4-16 shows the combustor's frequency response corresponding to the baseline, 1.5 g/s and 2.0 g/s axial microjet flow rate cases in Fig. 4-15. The 1/4 wavemode resonating around 40 Hz is dominant except for the cases when the axial microjets stabilize the unstable dynamics. When the axial microjets stabilize the dynamics, the sound pressure level at the resonant frequency decreases substantially; on the other hand, the sound pressure level at the 175 Hz becomes stronger. The baseline cases show that the resonant frequency slightly increases in the quasi-stable regime compared to the unstable regime, causing a discontinuity in the spectrum maps. However,

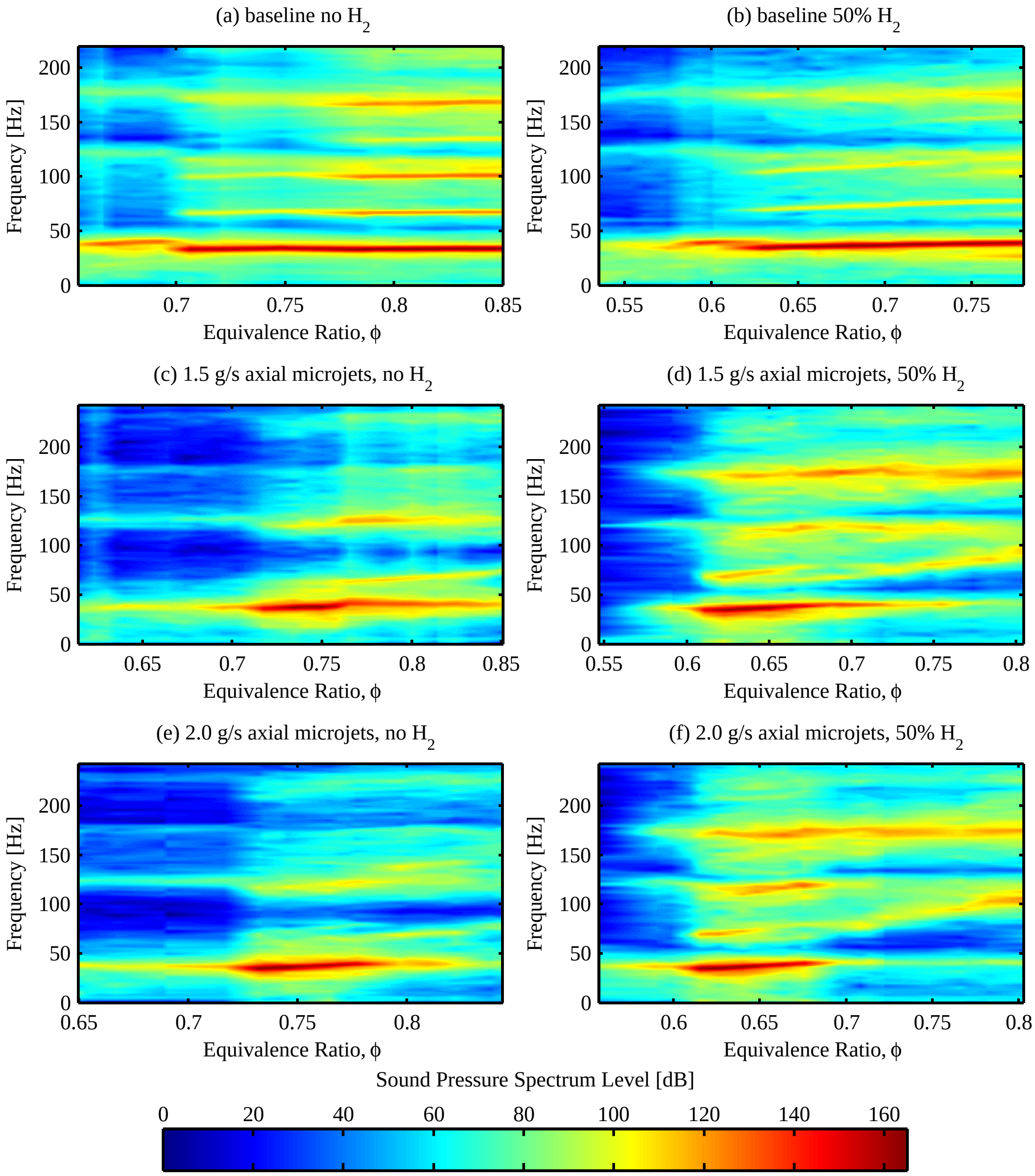

Figure 4-16: Sound pressure spectrum level maps as a function of equivalence ratio for the baseline, 1.5 g/s and 2.0 g/s axial microjet flow rate cases in Fig. 4-15.

with axial microjets, without hydrogen enrichment, the unstable band is continuous until the stable band is reached. With 50% by volume hydrogen enrichment, the quasi-stable band completely disappears, causing a sudden transition from unstable to stable dynamics.

Next, I increased the temperatures of the inlet mixture and the secondary air to

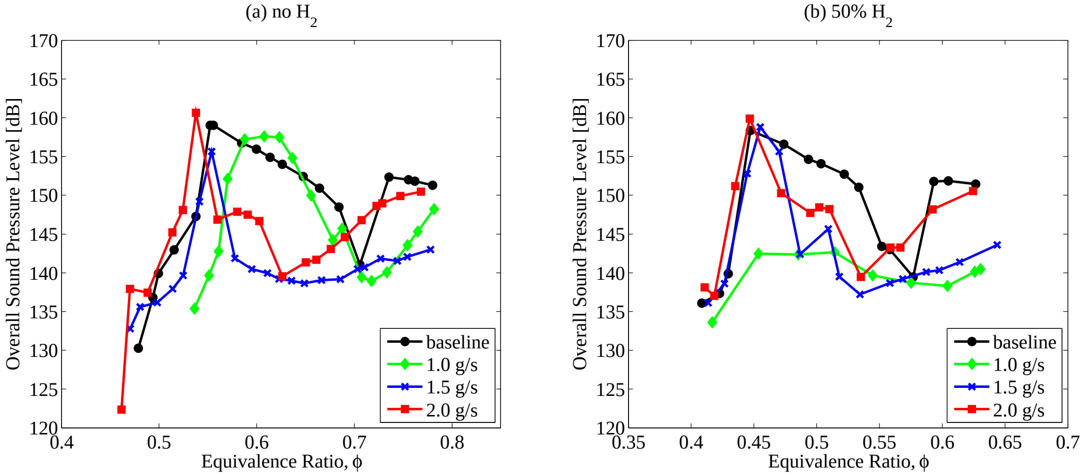

Figure 4-17: OASPL as a function of equivalence ratio at different axial microjet flow rates (a) without hydrogen enrichment and (b) with 50% by volume hydrogen enrichment. The temperatures of the inlet mixture and the axial microjets are 600 K.

600 K. Figure 4-17 shows the OASPL as a function of the equivalence ratio based on the main air flow rate at different axial microjet flow rates without hydrogen enrichment or with 50% by volume hydrogen enrichment. Although the axial microjets at a flow rate of 1 g/s do not suppress the pressure oscillations except at a narrow region near the quasi-stable to unstable transition without hydrogen enrichment, they suppress the pressure oscillations by around 20 dB at the entire equivalence ratio range corresponding to unstable and high-frequency unstable operating modes when 50% by volume hydrogen is added to propane. When the axial microjet flow rate is increased to 1.5 g/s, the pressure oscillations are suppressed by 15 dB, both without and with hydrogen enrichment except the region near the quasi-stable to unstable region. As the microjet flow rate is increased further to 2 g/s, the high-frequency unstable flame can no longer be stabilized. These results show that there is an optimum axial microjet flow rate depending on the fuel composition and the inlet temperature at which a robust stabilization of the dynamics is achieved.

In Fig. 4-18, I plot the combustor's frequency response corresponding to the baseline, 1.5 g/s and 2.0 g/s axial microjet flow rate cases in Fig. 4-17. The introduction

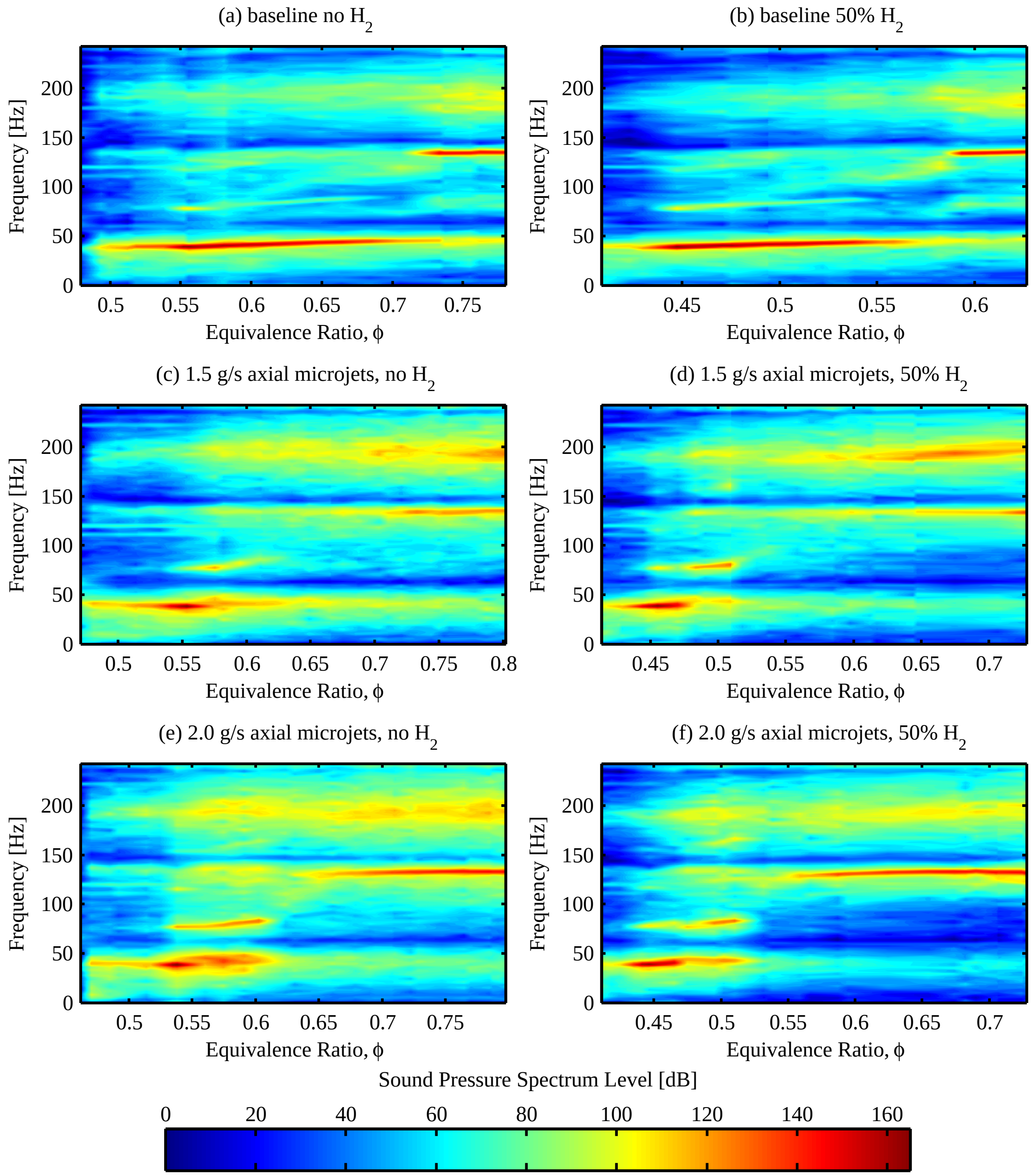

Figure 4-18: Sound pressure spectrum level maps as a function of equivalence ratio for the baseline, 1.5 g/s and 2.0 g/s axial microjet flow rate cases in Fig. 4-17.

of axial microjets cause the resonant frequency to shift to 85 Hz, corresponding to the 3/4 wavemode at intermediate values of equivalence ratios, except at the axial microjet flow rate of 1.5 g/s, without hydrogen enrichment. At this operating condition, the amplitude of the oscillations at the 85 Hz mode is always lower than that at the 40 Hz mode. When the axial microjet flow rate is 1.5 g/s, the high frequency unstable mode is suppressed. As the axial microjet flow rate is increased to 2.0 g/s, the 3/4 wavemode is excited independent of the hydrogen concentration in the fuel, and the high frequency unstable mode cannot be suppressed, suggested by the red bands observed at high equivalence ratios at both hydrogen concentrations. The excitation of the 3/4 wavemode is also suggested by the slight jumps in the OASPL in Fig. 4-17.

4.2.2 Flame Images

In order to distinguish between the dynamics at different operating conditions with passive control using axial microjets, I examine the flame images extracted from high speed videos of different operating modes and describe corresponding unsteady pressure, and heat-release rate measurements.

First, I investigate a typical operating condition when the axial microjets are ineffective in stabilizing the flame. In Fig. 4-19, a sequence of flame images is shown, recorded at: ϕ=0.55, without hydrogen enrichment, the temperatures of the inlet mixture and the axial microjets are 600 K, and the secondary air flow rate is 1.50 g/s. Figure 4-20 shows simultaneous heat-release rate and pressure measurements covering the same time period as the images shown in Fig. 4-19. The resonant frequency is 37 Hz, which corresponds to the 1/4 wavemode of the combustor. In this case, the secondary air injection through axial microjets causes the flame at the recirculation zone to blow out. Therefore, the flame anchors near the hot top wall of the combustor. The formation of the wake vortex, and its convection in the downstream direction towards the upper wall of the combustor cannot be observed from these images. Close to instant 1, the pressure is at its maximum value, i.e. the flow acceleration is maximum (recalling that the pressure leads the velocity by 90 degrees when the resonant frequency corresponds to the 1/4 wavemode). At this moment, I expect a wake vortex to be formed in the recirculation zone. The flame is pushed downstream

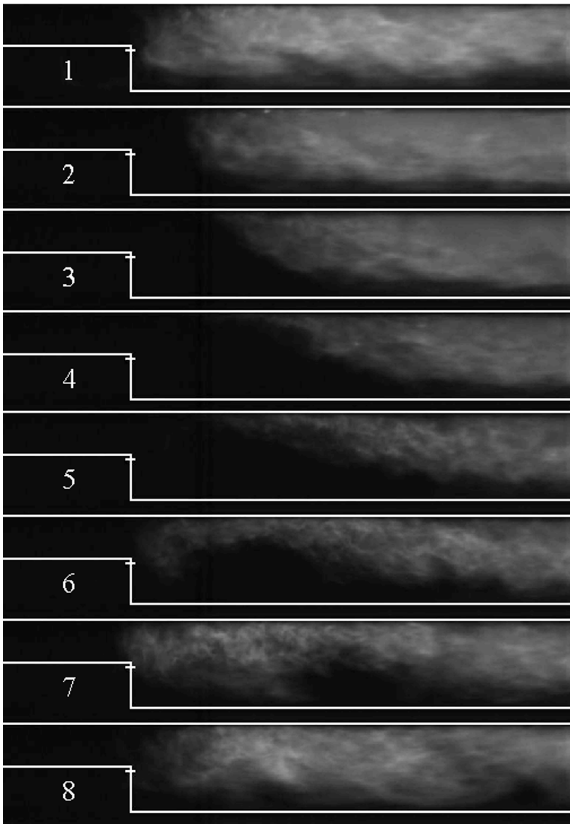

Figure 4-19: Sequential flame images with 1.50 g/s axial microjets, without hydrogen enrichment, at $\phi = 0.55$. The temperatures of the inlet mixture and the normal microjets are 600 K. The time between the frames is 3.9 ms.

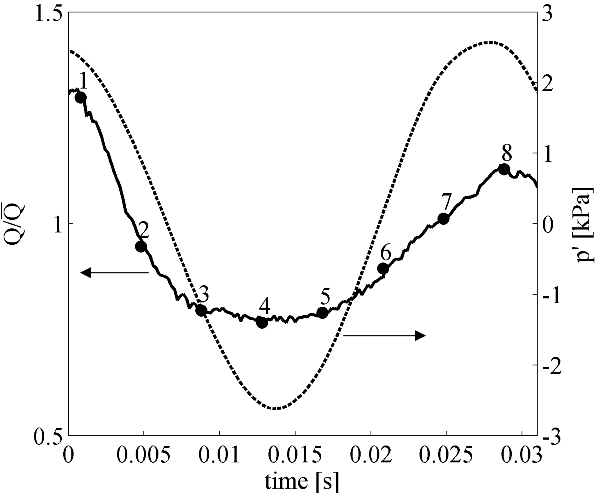

Figure 4-20: Simultaneous pressure and heat-release rate measurements corresponding to the instants in Fig. 4-19.

with the high flow velocity, while the vortex convects downstream towards the upper wall of the combustor (2-4). As the inlet velocity drops below its mean value, the flame near the upper wall of the combustor moves towards the step (5). At this moment, the flame area, thus the heat-release rate start to rise. At instant 6, the flame reaches the step and is wrapped around the vortex. The heat-release rate reaches its maximum value when the vortex reaches the upper wall of the combustor, and breaks down (8). The reactants within the vortex burn, generating significant flame area. The heat-release rate is in-phase with the pressure oscillations, generating thermo-acoustic instability. The maximum pressure amplitude is around 2.6 kPa, close to the value measured during the unstable operating mode of the combustor. In this case, secondary air injection through axial microjets does not prevent the strong unsteady flame-vortex interaction mechanism.

Now, I examine the flame images when the axial microjets are effective in suppressing the unstable operating mode of the combustor. In Fig. 4-21, a sequence of flame images is shown, recorded at: ϕ=0.66, without hydrogen enrichment, the temperatures of the inlet mixture and the axial microjets are 600 K, and the secondary air flow rate is 1.50 g/s. Figure 4-22 shows simultaneous heat-release rate and pressure measurements covering the same time period as the images shown in Fig. 4-21. At this equivalence ratio, the axial microjets do not cause the flame to blow out near the recirculation zone. The vortex at the recirculation zone is steady, and trapped within a small zone downstream of the step. The axial microjets act as a restriction, not allowing the vortex to convect downstream and move towards the upper wall of the combustor, preventing the flame-vortex interactions. Thus, the flame is steady, generating almost steady heat-release rate.

Finally, I examine the flame images when the axial microjets are effective in suppressing the high-frequency unstable operating mode of the combustor. In Fig. 4-23, a sequence of flame images is shown, recorded at: ϕ=0.78, without hydrogen enrich-

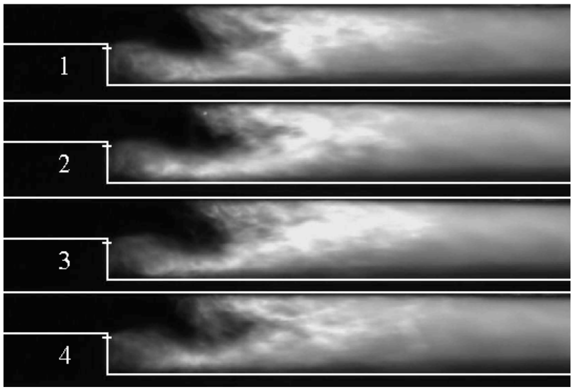

Figure 4-21: Sequential flame images with 1.50 g/s axial microjets, without hydrogen enrichment, at $\phi = 0.66$. The temperatures of the inlet mixture and the normal microjets are 600 K. The time between the frames is 8.3 ms.

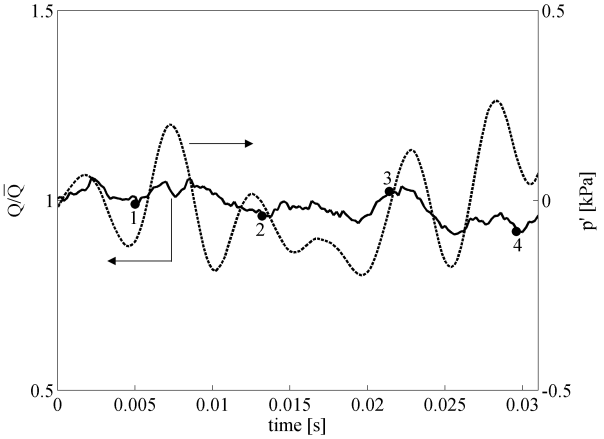

Figure 4-22: Simultaneous pressure and heat-release rate measurements corresponding to the instants in Fig. 4-21.

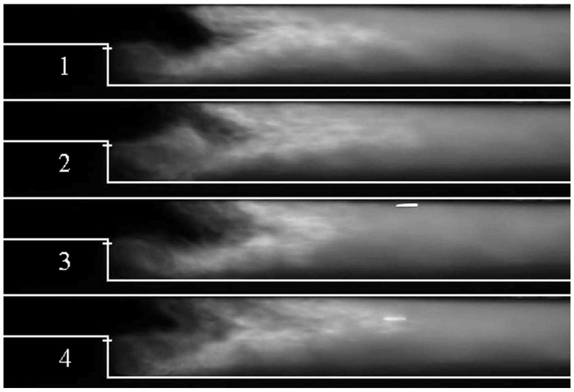

Figure 4-23: Sequential flame images with 1.50 g/s axial microjets, without hydrogen enrichment, at $\phi = 0.78$. The temperatures of the inlet mixture and the normal microjets are 600 K. The time between the frames is 6.7 ms.

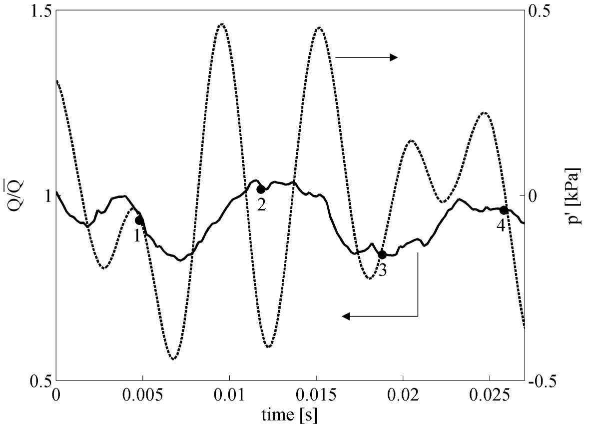

Figure 4-24: Simultaneous pressure and heat-release rate measurements corresponding to the instants in Fig. 4-23.

ment, the temperatures of the inlet mixture and the axial microjets are 600 K, and the secondary air flow rate is 1.50 g/s. Figure 4-24 shows simultaneous heat-release rate and pressure measurements covering the same time period as the images shown in Fig. 4-23. The flame shapes and the combustion dynamics with axial microjets are the same as above. Again, the unsteady interactions between the wake vortex and the flame are prevented by the axial microjets by which the hydrodynamics of the flame anchoring zone are stabilized. The heat-release rate is almost steady, does not couple with the acoustics of the combustor; thus preventing thermoacoustic instability.

After the axial microjets are turned on at an optimum axial microjet flow rate

(i) preventing the local flame blowout near the step, and (ii) high enough to impact the dynamics of the recirculation zone, the disruption of the flame-vortex interactions results in mismatch between the pressure-heat release rate phase correlation, significantly reducing the pressure amplitude. As a result, the phase relationship between the pressure and the heat-release becomes random, leading to the stable dynamics [70].

4.3 Summary

In this chapter, I experimentally investigated the effectiveness of passive control by injecting steady air flow near the step in the cross-stream or streamwise directions through choked micro-diameter holes.

At operating conditions when the flame detaches from the step and flashes back into the upstream channel without air injection, when air is injected in the cross-stream direction, the flame anchors slightly upstream of the step instead of on the unsteady recirculation zone, which suppresses the instability. On the other hand, at operating conditions corresponding to the low-frequency unstable and high-frequency unstable operating modes of the combustor without air injection, air injection in the cross-stream direction is ineffective in stabilizing the dynamics, which is still governed by the flame-vortex interactions. In these cases, the 3/4 wavemode of the combustor, in addition to the 1/4 and the 5/4 wavemodes is excited. The equivalence ratios at which the resonant frequency shifts to the 3/4 wavemode is predicted well with the model developed in Chapter 2.

When air is injected in the streamwise direction near the edge of step, both the unstable and the high-frequency unstable dynamics could be stabilized at an optimum secondary air flow rate which depends on the operating conditions. When effective, the secondary air flow suppresses the shedding of an unsteady vortex, and hence the flame-vortex interaction mechanism. Instead, a compact, stable flame is formed near the step. On the other hand, when air injection in the streamwise direction is ineffective, the flame blows out near the step; instead it anchors at the hot top wall of of the combustor. In this case, the flame is unsteady, the flame-vortex interactions are strong, and the dynamics are distinct compared to that at the low-frequency unstable and high-frequency unstable modes.

These results suggest that the interaction between the flame and the unsteady vortex shedding is a leading cause of the instability, as proposed earlier. They also suggest that blocking this interaction can lead to suppressing the dynamics.

Chapter 5

Modeling the Dynamic Response of Laminar Perforated-Plate Stabilized Flames

In this chapter, I develop a model to determine the transfer function between the heat-release rate and the velocity oscillations in perforated-plate stabilized flames under different power and equivalence ratios. Previous planar flame models have been successfully extended to account for the conical flame surfaces formed downstream of the plate holes. The coupled effects of the heat loss to the plate and the flame kinematics have been modeled. In order to validate the model, the model results are compared to the experimental measurements.

5.1 Analytical Model

In order to obtain the response of the heat-release rate to inlet velocity oscillations, I consider: i) The flame surface kinematics to represent the flame area response; ii) The heat loss to the burner plate due to flame-wall interactions, to introduce the burning velocity response. These mechanisms are coupled, since the heat loss

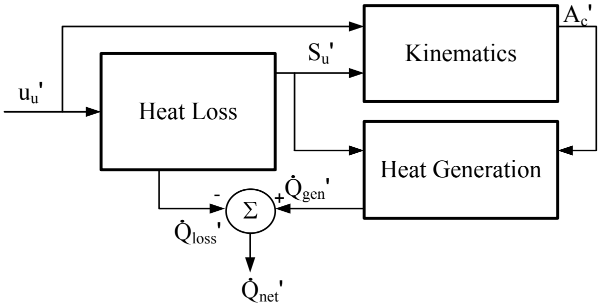

Figure 5-1: The block diagram summarizing the modeling approach.

to the burner plate causes the flame temperature to oscillate, resulting in burning velocity oscillations, which strongly impact the flame surface kinematics. I model the flame surface kinematics by solving the flame surface kinematics equation [23], while treating the inlet velocity and the flame burning velocity as the inputs. Then, I model the heat loss to the burner plate and relate the fluctuations in the burning velocity to the inlet velocity. Finally, I merge both of these mechanisms to derive the response of the net heat-release rate to inlet velocity fluctuations. The block diagram of the modeling approach is shown in Fig. 5-1.

5.1.1 Flame Kinematics

Figure 5-2 shows a schematic diagram of the flame surface observed in a typical perforated-plate stabilized configuration. The infinitely thin flame consists of planar and conical surfaces; the former is formed downstream of the perforated-plate surface and the latter is formed downstream of the holes. The flame structure I observed in the experiments validate this assumption. The flame surface temperature, T_b is assumed to be uniform along the flame surface, and hence the burning velocity with respect to the reactant mixture, S_u, is also uniform. Consistent with the scope of this study, which is to obtain an analytical flame model extending the previous planar flame models, the flame temperature, the burning velocity and their variations are taken as averages over the entire flame surface. This assumption becomes more accurate as

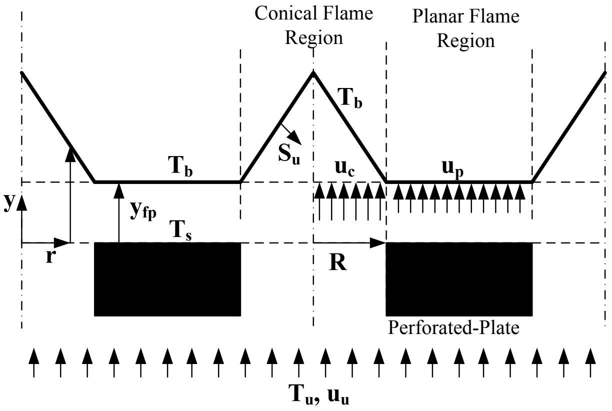

Figure 5-2: Schematic diagram of the modeled flame surface in perforated-plate stabilized configuration.

the area of the holes decreases as compared to the area of the burner plate. Further, I assume that the impact of stretch on the laminar burning velocity is negligible. The temperature of the burner surface is T_s. The inlet temperature, T_u, and density, ρ_u, are constant. The velocity of the inlet mixture is u_u. The velocities entering the planar and conical regions are u_p, and u_c, respectively, and are only dependent on time. The radial velocities and the effect of expansion due to combustion are neglected. These idealizations are limitations of the model and could be relaxed in the future studies. There are total of N holes with radii of R. The planar flames stabilize at a distance y_{fp} away from the burner surface as a result of the heat loss. The distance between the plate surface and the conical flame is represented by y_{fc}, and is a function of the radial direction, r, and time, t. The area of the inlet is A_u, and the total area of the holes is $A_{open} = \pi R^2 N$. The total area of the planar and conical flame surfaces are A_p and A_c, respectively. All the variables are linearized by separating them into mean and oscillatory components, $x = \bar{x} + x'$, and oscillations are spatially uniform and periodic functions of time. Note that the oscillations are acoustic, thus the effects of unsteady vortex shedding is neglected. This is a plausible assumption since the amplitude of the flow oscillations are typically small at these low velocities.

I model the kinematics of flame surfaces using a similar approach as Fleifil et al. [23]; solving the flame surface kinematics equation. For planar and conical flame surfaces, respectively:

$$\frac{\partial y_{fp}(t)}{\partial t} = u_p(t) - S_u(t) \tag{5.1}$$

$$\frac{\partial y_{fc}(r,t)}{\partial t} = u_c(t) - S_u(t)\sqrt{\left(\frac{\partial y_{fc}(r,t)}{\partial r}\right)^2 + 1} \tag{5.2}$$

Linearizing Eqs. (5.1) and (5.2), I obtain the following for the mean components, respectively:

$$\bar{u}_p = \bar{S}_u \tag{5.3}$$

$$d\bar{y}_{fc}/dr = -\sqrt{\left(\bar{u}_c/\bar{S}_u\right)^2 - 1} \tag{5.4}$$

In obtaining Eq. (5.4), the negative of the square root is taken, since the conical flame surfaces have negative slopes with respect to the radial direction. Since the velocity entering the flame is uniform and the expansion effects are ignored, the mean slope of the conical flame surface is constant; thus, the conical flame surfaces are V-shaped.

The oscillatory components of Eqs. (5.1) and (5.2), respectively, are:

$$\frac{\partial {y_{fp}}'}{\partial t} = {u_p}' - {S_u}' \tag{5.5}$$

$$\frac{\partial {y_{fc}}'}{\partial t} = {u_c}' - {S_u}'\frac{\bar{u}_c}{\bar{S}_u} + \frac{{\bar{S}_u}^2}{\bar{u}_c}\sqrt{\left(\frac{\bar{u}_c}{\bar{S}_u}\right)^2 - 1}\frac{\partial {y_{fc}}'}{\partial r} \tag{5.6}$$

Note that the flame response, ${y_{fp}}'(t)$ and ${y_{fc}}'(r,t)$, depends on ${S_u}'(t)$. Equation (5.5) suggests that the planar flame surfaces perform rigid-body oscillations, and the area of the planar flames, A_p is constant. The boundary condition of Eq. (5.6) is obtained by matching the oscillations of the conical flame surfaces with the oscillations of the planar flame surfaces at $r = R$: ${y_{fc}}'(R,t) = {y_{fp}}'(t)$.

Applying mass conservation in a control volume extending from the inlet to $y = y_{fp}$ plane, I obtain the following equations for mean and oscillatory components respectively:

$$A_{open}\bar{u}_c + A_p\bar{S}_u = A_u\bar{u}_u \tag{5.7}$$

$$A_{open}{u_c}' + A_p{S_u}' = A_u{u_u}' \tag{5.8}$$

Since $\bar{u}_p = \bar{S}_u$ and $\bar{u}_c \geq \bar{S}_u$, Eq. (5.7) implies $\bar{S}_u \leq \bar{u}_u$. Note that when $\bar{u}_c = \bar{S}_u = \bar{u}_u$, the conical flame surfaces disappear, the flame becomes flat. Since, $L/\bar{c} << 1/f_{res}$ for a typical burner, where L is the distance between the location where ${u_u}'$ is measured and the tip of the flame, $\bar{c}$ is the average speed of sound and f_{res} is the resonant frequency; and neglecting ${u_u}'$, ${u_p}'$ and ${u_c}'$ are in-phase. In order to satisfy Eq. (5.8), and to obtain an analytical result, I assume ${u_p}' = {u_u}'\bar{S}_u/\bar{u}_u$ and ${u_c}' = {u_u}'\bar{u}_c/\bar{u}_u$. I would like to note that using uniform harmonic modulation to model the acoustic oscillations upstream of the conical flame surfaces is an idealization. A more realistic approach to be considered in the future is to model the velocity upstream of the conical surfaces in the form of a convective wave propagating with the average flow velocity and to decrease the amplitude of oscillations with increasing y [71]. I obtain the solutions of Eqs. (5.5) and (5.6) by taking the Laplace transforms of both equations. The solutions of Eqs. (5.5) and (5.6) in frequency domain, defining: $\beta \equiv \bar{S}_u/\bar{u}_c\sqrt{(\bar{u}_c/\bar{S}_u)^2 - 1}$ is:

$$\hat{y}_{fp}(s) = \frac{1}{s}\left[\hat{u}_u(s)\frac{\bar{S}_u}{\bar{u}_u} - \hat{S}_u(s)\right] \tag{5.9}$$

$$\hat{y}_{fc}(r,s) = \frac{1}{s}\left\{\left[\frac{\bar{u}_c}{\bar{u}_u}\hat{u}_u(s) - \frac{\bar{u}_c}{\bar{S}_u}\hat{S}_u(s)\right] - \left[\left(\frac{\bar{u}_c - \bar{S}_u}{\bar{u}_u}\right)\hat{u}_u(s) - \left(\frac{\bar{u}_c}{\bar{S}_u} - 1\right)\hat{S}_u(s)\right] \cdot \exp\left[\frac{(r-R)s}{\bar{S}_u\beta}\right]\right\} \quad (5.10)$$

where s is the complex frequency and for all variables $\hat{x}(r,s)$ is Laplace transform of $x'(r,t)$. The area of the conical flame surface is:

$$A_c = 2\pi N \int_0^R \sqrt{1 + \left(\frac{dy_{fc}}{dr}\right)^2}\, rdr \quad (5.11)$$

Linearizing Eq. (5.11), and using Eq. (5.4), the mean and oscillatory components of conical flame surface area are:

$$\bar{A}_c = A_{open}\bar{u}_c/\bar{S}_u \quad (5.12)$$

$$A_c{}' = -2\pi N\beta \int_0^R \left(\partial y_{fc}{}'/\partial r\right) rdr \quad (5.13)$$

Taking the Laplace transform of Eq. (5.13), and using the flame surface response obtained in Eq. (**??**), I obtain the linear oscillatory response of the conical flame surface area in the frequency domain:

$$\hat{A}_c(s) = \frac{2\pi N\bar{S}_u\beta^2}{s^2}\left[\left(\frac{\bar{u}_c - \bar{S}_u}{\bar{u}_u}\right)\hat{u}_u(s) - \left(\frac{\bar{u}_c}{\bar{S}_u} - 1\right)\hat{S}_u(s)\right] \cdot \left[\exp\left(\frac{-Rs}{\bar{S}_u\beta}\right) + \frac{Rs}{\bar{S}_u\beta} - 1\right] \quad (5.14)$$

Equation (5.14) shows the strong dependence of the flame surface area oscillations on inlet and burning velocity oscillations. When $\bar{u}_c = \bar{S}_u = \bar{u}_u$, $\hat{A}_c(s) = 0$. The conical flame area becomes $A_c = A_{open}$, hence the flame becomes flat.

The heat-release rate, $\dot{Q}_{gen}$, due to combustion is:

$$\dot{Q}_{gen} = \rho_u S_u \Delta H (A_c + A_p) \tag{5.15}$$

where ΔH is the absolute value of the enthalpy of reaction of the fuel per kg of the reacting mixture. Linearizing Eq. (5.15), the mean heat generation rate becomes:

$$\bar{\dot{Q}}_{gen} = \rho_u \bar{S}_u \Delta H \left(A_{open} \bar{u}_c / \bar{S}_u + A_p \right) \tag{5.16}$$

The oscillatory heat generation rate in the frequency domain, $\hat{\dot{Q}}_{gen}(s)$, is:

$$\hat{\dot{Q}}_{gen}(s) = \rho_u \Delta H \left[(A_{open} \bar{u}_c / \bar{S}_u + A_p) \hat{S}_u(s) \right] + \rho_u \Delta H \bar{S}_u \hat{A}_c(s) \tag{5.17}$$

Note that the heat-release rate oscillations are dependent on both the conical flame surface area and the burning velocity oscillations. The conical flame surface area oscillations are derived in Eq. (5.14). The burning velocity fluctuations is described in the next section by modeling the heat loss to the plate.

5.1.2 Heat Loss

In previous studies [22, 27–30, 72], burning velocity oscillations in perforated-plate stabilized planar flames were modeled by accounting for the heat loss mechanism to the plate. In Ref. [30], Rook derived the burning velocity-inlet velocity transfer function for planar perforated-plate stabilized flames ignoring the increase in the flame surface area as a result of the formation of conical flame surfaces, assuming unity Lewis number, zero flame stretch and single step reaction mechanism. In this model the flame performs rigid-body oscillations, and the temperature at $y = 0$ plane is uniform, $\bar{T}_s$. Thus, the heat transfer coefficient between the burner plate and the mixture flowing from the holes is infinite. Although, Rook obtained reasonable results at low inlet velocity, i.e. low power conditions, the model is limited by the planar flame assumption, i.e. it is only valid when the mean inlet velocity is equal to the mean burning velocity. At higher inlet velocities the flame surface is two-dimensional.

In order to relate the response of burning velocity oscillations to inlet velocity accurately, one needs to solve the 2-D conservation equations coupled with the heat loss to the plate. I use Rook's planar model [30] to *estimate* the burning velocity response of the modeled 2-D flame, by assuming that the heat and mass diffusion in the tangential direction of the flame surfaces are negligible compared to the normal direction. Furthermore, the impact of flame-area oscillations on the burning velocity response is neglected, which is consistent with assuming a uniform burning velocity response at the entire flame surface. Using these assumptions, the temperature in the normal direction to the flame surfaces of the 2-D flame is the same as the temperature obtained in Rook's planar model setting the mean and oscillatory velocity at the inlet to be $\bar{S}_u$ and ${u_p}'$, respectively. The "excess inlet velocity" generates the extra flame surface area; the conical flame surfaces.

The burning velocity oscillations in the frequency domain are [30]:

$$\hat{S}_u(s) = \left(\frac{KL(s)}{KL(s) + \frac{\delta}{\bar{S}_u} s} \right) \frac{\bar{S}_u}{\bar{u}_u} \hat{u}_u(s) \tag{5.18}$$

with

$$K = Ze/2 \cdot 1/(\bar{T}_b - T_u) \tag{5.19}$$

$$L(s) = (T_{ad} - T_u) \exp\left(-\bar{\psi}_{fp}/\delta\right) \cdot \exp\left[\frac{\bar{\psi}_f}{2\delta} \left(1 - \sqrt{1 + \frac{4\delta}{\bar{S}_u} s} \right) \right] \tag{5.20}$$

where $Ze \equiv T_{act}(\bar{T}_b - T_u)/{\bar{T}_b}^2$ is the Zeldovich number, T_{act} is the activation temperature, T_{ad} is the adiabatic flame temperature, $\delta \equiv \alpha_u/\bar{S}_u$ is the flame thickness, where α_u thermal diffusivity of the inlet mixture, and $\bar{\psi}_{fp} \equiv \delta \ln\left[(T_{ad} - T_u)/(T_{ad} - \bar{T}_b + \bar{T}_s - T_u)\right]$ is the density-weighted mean flame stand-off distance. Detailed derivation could be found in Refs. [29, 30].

Now, I determine the rate of heat loss to the burner plate surface. The mean and oscillatory rates of heat loss to the plate surface are:

$$\bar{\dot{Q}}_{loss} = A_p \lambda_s \partial \bar{T}/\partial y|_{y=0^+} \tag{5.21}$$

$$\dot{Q}_{loss}{}' = A_p \lambda_s \partial T'/\partial y|_{y=0^+} \tag{5.22}$$

where $\dot{Q}_{loss}$ is the rate of heat loss to the burner plate, λ_s is the thermal conductivity of the mixture at the plate surface. Rook[30] derives the mean and oscillatory temperature profiles in density-weighted coordinates. Using the mean temperature profile, Eq. (5.21) becomes:

$$\bar{\dot{Q}}_{loss} = \rho_u \bar{S}_u A_p \Delta H \exp(-\bar{\psi}_{fp}/\delta) \tag{5.23}$$

The oscillatory heat loss rate in frequency domain, $\hat{\dot{Q}}_{loss}(s)$, is obtained by substituting the temperature response derived in Ref. [30] in Eq. (5.22):

$$\hat{\dot{Q}}_{loss}(s) = -\rho_u A_p \Delta H \exp\left(-\bar{\psi}_{fp}/\delta\right) \cdot \frac{1}{2}\left(1 + \sqrt{1 + \frac{4\delta}{\bar{S}_u} s}\right) / \left(\frac{\delta}{\bar{S}_u} s\right) \cdot \left[\frac{\bar{S}_u}{\bar{u}_u} \hat{u}_u(s) - \hat{S}_u(s)\right] \tag{5.24}$$

5.1.3 Net Heat-Release Rate

The net mean heat-release rate, $\bar{\dot{Q}}_{rel}$, and the net heat-release rate oscillations in frequency domain, $\hat{\dot{Q}}_{rel}(s)$, are calculated from:

$$\bar{\dot{Q}}_{rel} = \bar{\dot{Q}}_{gen} - \bar{\dot{Q}}_{loss} + \dot{Q}_{bur} \tag{5.25}$$

$$\hat{\dot{Q}}_{rel}(s) = \hat{\dot{Q}}_{gen}(s) - \hat{\dot{Q}}_{loss}(s) \tag{5.26}$$

where $\bar{\dot{Q}}_{gen}$, $\bar{\dot{Q}}_{loss}$, $\hat{\dot{Q}}_{gen}(s)$ and $\hat{\dot{Q}}_{loss}(s)$ are derived in Eqs. (5.16) , (5.23), (5.17), and (5.24), respectively. $\dot{Q}_{bur}$ accounts for heating of the mixture inside the holes by the heat transfer from the plate. Note that the temperature oscillations in the solid plate are negligible, implying that $\dot{Q}_{bur}{}' \sim 0$. The transfer function relating the net heat-release rate oscillations to inlet velocity oscillations, $\hat{\dot{Q}}_{rel}(s)/\hat{u}_u(s)$, is obtained by dividing Eq. (5.26) with the Laplace transform of the inlet velocity, $\hat{u}_u(s)$.

5.2 Experimental Setup

Experiments were performed to validate the dynamic heat-release model. A ceramic burner plate, with 2530, 1 mm diameter; and 368, 4 mm diameter holes was used. The burner dimensions are 21.3 cm × 8.0 cm × 1.3 cm. The burner was supplied with a uniform methane/air mixture. Fuel and air flow rates were controlled to obtain the desired power and equivalence ratio. The inlet velocity in the mixing chamber was excited using a subwoofer loudspeaker driven at low frequencies (10 Hz - 500 Hz). The modulation level was 10% of the mean air flow, and around this region, no dependency on the modulation level is observed. A stepwise frequency sweep was applied to determine the flame response to velocity oscillations. In the mixing chamber a TSI IFA 300 hot wire anemometer was used to monitor the velocity fluctuations. The velocity was measured 3 cm upstream of the burner plate surface. It has been shown that the heat release is proportional to light emission from free radicals like CH* or OH* [73]. The spatially integrated time dependent heat-release rate oscillations were detected by measuring CH* chemiluminescence using a Hamamatsu R3788 photomultiplier with an interference filter at 430 nm. Because the conical flame area is smaller than the total plate area, I neglected the spatial variation in the burning rate with respect to the temporal variation. The spatially integrated CH* emissions captured in the experiments are averaged over many cycles to determine the heat-release rate-inlet velocity transfer function. Similar measurements were performed by Noiray et al. [74] in perforated plate burners using OH* chemiluminescence. A multi-channel data acquisition device was used to synchronize the excitation and to detect the signals. After performing some calibration measurements the heat-release rate-inlet velocity transfer function was obtained.

5.3 Results

To determine the response of the net heat-release rate to dynamics, model results were obtained at different equivalence ratios and power outputs, $\bar{\dot{Q}}_{gen}$, using the specifications of the burner plate mentioned in the previous section while superposing the results obtained for the two different hole sizes used in the experiment. The activation temperature was fixed at 15000 K, a typical value for single-step methane combustion. I calculated the mean inlet velocity using: $\bar{u}_u = \bar{\dot{Q}}_{gen}/[\rho_u A_u \Delta H(\phi)]$. I performed a parametric study to determine the impact of the flame temperature, $\bar{T}_b$, and the burner plate surface temperature, $\bar{T}_s$, on the flame response and assumed reasonable values for these parameters at each operating condition. For steady flames, the following relation between $\bar{T}_b$ and $\bar{S}_u$ is used [75, 76]:

$$\frac{\bar{S}_u}{\bar{S}_{u,ad}} = \exp\left[\frac{-T_{act}}{2}\left(\frac{1}{\bar{T}_b} - \frac{1}{T_{ad}}\right)\right] \tag{5.27}$$

where $\bar{S}_{u,ad}$ is the adiabatic burning velocity for a given equivalence ratio calculating using the following correlation [77]:

$$\bar{S}_{u,ad} = A\phi^B \exp\left[-C(\phi - D)^2\right] \tag{5.28}$$

where $A = 0.6079$, $B = -2.554$, $C = 7.31$, and $D = 1.230$. After determining $\bar{S}_u$ from Eq. (5.27), I calculated $\bar{u}_c$ using Eq. (5.7). Once I determine $\bar{u}_u$, $\bar{T}_b$, $\bar{T}_s$, $\bar{S}_u$ and

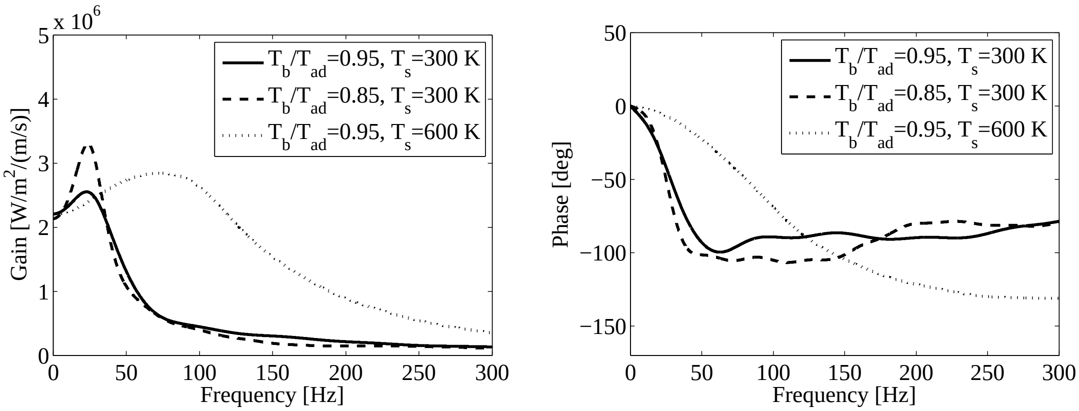

Figure 5-3: The impact of the flame temperature, $\bar{T}_b$, and the burner surface temperature, $\bar{T}_s$, on the gain and phase of the response of the net heat heat-release rate per inlet area to the inlet velocity fluctuations at 10 kW power and equivalence ratio of 0.65. $T_{ad} = 1755$ K.

$\bar{u}_c$, all the parameters used in the model are known.

In Fig. 5-3 I show model results for the impact of the flame temperature, $\bar{T}_b$, and the burner plate surface temperature, $\bar{T}_s$, on the gain and phase of the net heat-release rate-inlet velocity transfer function at 10 kW power and equivalence ratio of 0.65. The adiabatic flame temperature is 1755 K. At this operating condition, the planar flame model is not applicable since the mean inlet velocity, $\bar{u}_u$=27.9 cm/s, is much higher than the adiabatic burning velocity, $\bar{S}_{u,ad}$=15.6 cm/s.

Results show non zero gain at all frequencies, and resonance at 30 Hz when $\bar{T}_s$=300 K, and at 80 Hz when $\bar{T}_s$=600 K. I observe that without heat loss, the flame stand-off distance simply responds to flow oscillations, resulting in fixed amplitude oscillations. With heat loss, as the flame moves away / towards the burner, its burning velocity increases / decreases, amplifying the flame motion. The enthalpy oscillations resulting from the oscillatory heat loss at the burner surface are transported to the flame after a convective time delay in the order of $\tau \sim \bar{\psi}_{fp}/\bar{S}_u$, where $\bar{\psi}_{fp}$ is the density-weighted flame stand-off distance as mentioned before. This positive coupling between the heat loss and the flame position manifests itself in the gain response. Since the burning rate is assumed to respond instantaneously to the fluctuations in the temperature, the burning velocity of the flame oscillates in-phase with the enthalpy fluctuations reaching the flame front. Depending on the frequency of the imposed oscillations, f, the convective time delay results in a phase difference of $2\pi\tau f$ between the burning velocity and the heat loss oscillations. When this phase is $\pi/2$, the flame reaches its absolute minimum or maximum distance from the burner depending on the propagation direction; that is the resonant behavior shown in Fig. 5-3 occurs. The resonant frequency is $f_{res} = 1/(4\tau) \sim \bar{S}_u/(4\bar{\psi}_{fp})$. For more discussion, see Refs. [29, 30]. As the burner surface temperature is raised while keeping the flame temperature constant, the convective time delay decreases due to the reduction in $\bar{\psi}_{fp}$. As a result, the resonant frequency increases when the burner surface temperature is increased at constant flame temperature, as observed in Fig. 5-3.

Figure 5-3 shows that the delay between heat release-rate and inlet velocity increases rapidly for the range of frequencies between zero and almost twice the resonant frequency, and remains nearly constant as the frequency is increased further. In order to explain the origin of this observation, I plot the contributions of the burning velocity and flame-area oscillations to the net heat-release rate fluctuations for a 10 kW power burner, $\phi = 0.65$ and $\bar{T}_b/T_{ad} = 0.95$, $\bar{T}_s = 300\,\mathrm{K}$. The inlet velocity performs sinusoidal oscillations, i.e. $u_u{}' = \epsilon\bar{u}_u \ \sin(\omega t)$. As shown in Fig. 5-4, when the net heat-release rate response due to flame-area oscillations is out-of-phase / in-phase with the inlet velocity oscillations, the flame-area oscillations decrease / increase the amplitude of the net heat-release rate fluctuations. At low frequencies, a significant portion of the net heat-release rate oscillations are caused by the burning velocity oscillations associated with the heat loss. At higher frequencies with respect to the resonant frequency, the net heat-release rate oscillations are still present, but only as a result of the flame-area fluctuations, making the burner still prone to thermoacoustic instabilities even at frequencies significantly higher than the resonant frequency. At higher inlet velocity, the effect of flame-area oscillations become more significant,

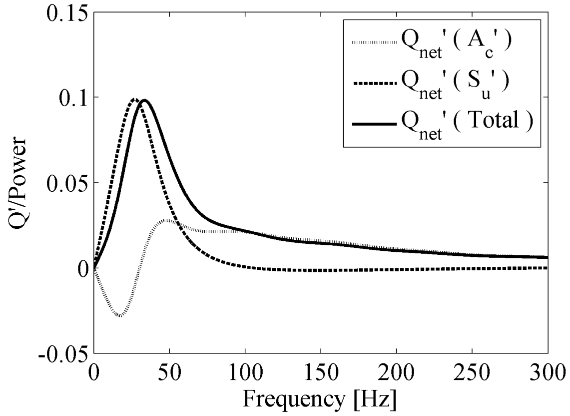

Figure 5-4: Contributions of flame area and burning velocity oscillations on the net heat-release rate fluctuations at 10 kW power and equivalence ratio of 0.65. $\bar{T}_b/T_{ad} = 0.95$, $\bar{T}_s = 300$ K, $u_u{}' = \epsilon \bar{u}_u sin(\omega t)$, where $\epsilon = 0.1$, $\omega t = \pi$.

increasing the amplitude of the net heat-release rate oscillations. Increase in the inlet velocity does not effect the resonant frequency or the heat-release rate response at low frequencies, which are controlled primarily by burning velocity oscillations. Higher burner surface temperature at fixed flame temperature, $\bar{T}_b$, increases the impact of the flame-area oscillations at higher frequencies, because the resonance occurs at higher frequency.

Figure 5-5 shows the contributions of the inlet velocity and the burning velocity oscillations to the flame-area oscillations for the same parameters used in Fig. 5-4. I observe that at low frequency, both the inlet velocity and the burning velocity oscillations contribute to the flame-area oscillations. At higher frequencies, the only contribution comes from the velocity oscillations, because the burning velocity oscillations decay quickly. Therefore, the phase of the response of the flame area to inlet velocity becomes nearly constant resulting in a constant phase of the net heat-release rate response observed in Fig. 5-3, within the range of frequencies where only flame-area oscillations are present.

In Figs. 5-6 and 5-7, I compare the gain and the phase of the measured and computed net heat-release rate-inlet velocity transfer function, at equivalence ratios

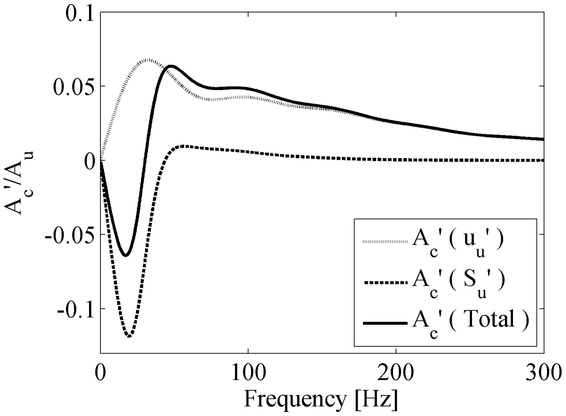

Figure 5-5: Contributions of the inlet velocity and the burning velocity oscillations on the conical flame surface area oscillations per inlet area at 10 kW power and equivalence ratio of 0.65. $\bar{T}_b/T_{ad} = 0.95$, $\bar{T}_s = 300$K, $u_u' = \epsilon \bar{u}_u sin(\omega t)$, where $\epsilon = 0.1$, $\omega t = \pi$.

of 0.74 and 0.65 at 5 kW and 10 kW power, respectively. T_{ad} at these equivalence ratios are 1921 K and 1755 K, respectively. The flame and burner plate surface temperatures are chosen to obtain the best match with the experimental results. $\bar{T}_b$ and $\bar{T}_s$ are 1595 K and 750 K, respectively at $\phi = 0.74$; and 1700 K and 450 K, respectively at $\phi = 0.65$. The model captures the trends observed in the experiment and accurately predict the phase and its saturation around 200 Hz. As the equivalence ratio is raised, the heat loss increases, resulting in lower flame temperature, and higher burner surface temperature. The convective time delay, $\bar{\psi}_{fp}/\bar{S}_u$ decreases, increasing the resonant frequency.

5.4 Summary

In this chapter, I extended the dynamic planar flame models of perforated-plate stabilized flames to account for the formation of conical flame surfaces downstream of a perforated-plate holes in order to introduce the effect of flame-area fluctuations. In summary: i) At low frequencies with respect to the resonant frequency, the contribution of flame-area oscillations to the net heat-release rate is weak compared to

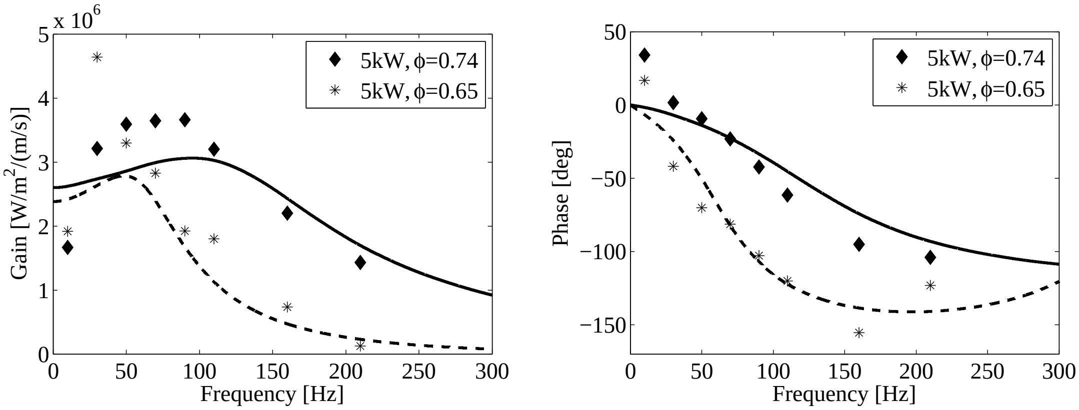

Figure 5-6: Gain and phase of the net heat release per inlet area-inlet velocity transfer function. Markers show experimental measurements. Curves are model results: $\phi = 0.74$, solid lines; $\phi = 0.65$, dashed lines. Power=5 kW.

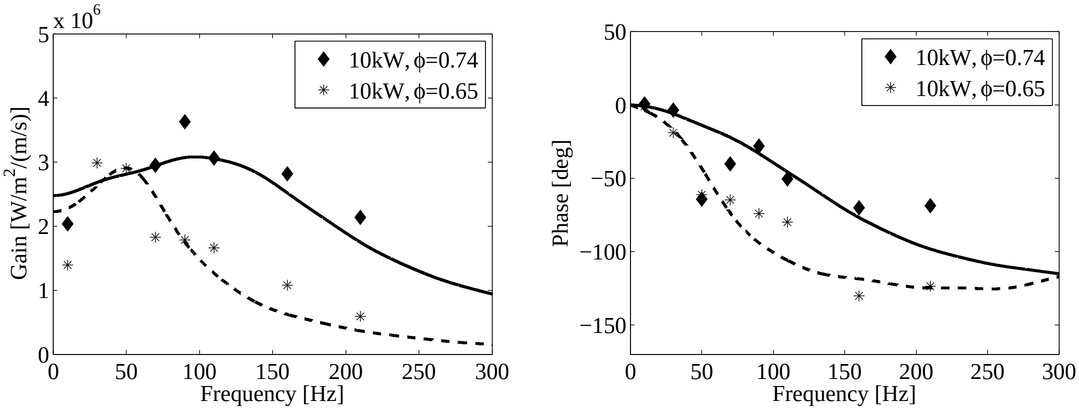

Figure 5-7: Gain and phase of the net heat release per inlet area-inlet velocity transfer function. Markers show experimental measurements. Curves are model results: $\phi = 0.74$, solid lines; $\phi = 0.65$, dashed lines. Power=10 kW.

that of the burning velocity oscillations. At these frequencies, flame-area oscillations arise both due to the impact of inlet velocity and burning velocity oscillations; ii) When the frequency is high with respect to the resonant frequency, only flame-area oscillations contribute to the net heat-release rate fluctuations, which arise as a result of the inlet velocity fluctuations; iii) The conical flame surface area increases at high inlet velocity and low equivalence ratio, increasing the impact of flame-area oscillations; and iv) When heat loss is large, the burning velocity drops, the plate surface temperature rises and the resonant frequency increases. Thus, the flame-area oscillations impact the heat-release rate response at higher frequencies. This model can be extended further upon taking into account the effect of expansion velocity while modeling the conical flame surfaces, treating the heat transfer inside the burner more realistically, using more realistic velocity profiles, and developing more accurate models to predict the oscillations of the burning velocity while taking into account the two-dimensionality of the problem in more detail.

Chapter 6

Two-Dimensional Numerical Simulations of Laminar Perforated-Plate Stabilized Flames

The model developed in the previous chapter relies on the specification of two parameters, the flame temperature, $\bar{T}_b$, and the perforated-plate surface temperature, $\bar{T}_s$. These parameters impact the flame transfer function significantly as shown in Fig. 5-3. In order to understand the impact of the operating conditions and the perforated-plate characteristics on these parameters, the steady flame structure and characteristics, and the dynamic response of the flames, I perform a two-dimensional numerical study to simulate the flame formed downstream of a single perforated-plate hole. The numerical model solves the velocity field under reactive conditions, whose effects cannot be captured by the analytical model. The analytical flame model represents the effect of the complex chemical kinetic processes only with two parameters, the Zeldovich number and the activation temperature, assuming a single-step reaction mechanism. This is an unrealistic oversimplification of the complex chemical kinetic processes. Therefore, in the flame simulations, a more detailed chemical kinetic mechanism for methane combustion is used. The temperature profile inside the perforated-plate is solved by allowing heat transfer between the gas and the perforated-plate to investigate the heat loss mechanism more realistically.

6.1 Formulation

The two-dimensional numerical model is based on a zero-Mach-number formulation of the compressible conservation equations in radial coordinates. Acoustic wave propagation is ignored, and the pressure field is decomposed into a spatially uniform component $p_o(t)$ and a hydrodynamic component $p(z, r, t)$ which varies both in space and time. Attention is restricted to open domains; the thermodynamic pressure p_o is constant. The model assumes zero bulk viscosity, and a detailed chemical reaction mechanism that involves K species and M elementary reactions. Soret and Dufour effects, radiant heat transfer, and body forces are ignored. The mixture is assumed to follow the perfect gas law, with individual species molecular weights, specific heats, and enthalpies of formation; and the Fickian binary mass diffusion. Under these assumptions, the mass, momentum, and energy conservation equations are respectively expressed as [78]:

$$\frac{\partial \rho}{\partial t} + \nabla \cdot (\rho \vec{V}) = 0 \tag{6.1}$$

$$\frac{\partial(\rho u)}{\partial t} + \frac{\partial(\rho u^2)}{\partial z} + \frac{1}{r}\frac{\partial(r\rho uv)}{\partial r} = -\frac{\partial p}{\partial z} + \Phi_z \tag{6.2}$$

$$\frac{\partial(\rho v)}{\partial t} + \frac{\partial(\rho vu)}{\partial z} + \frac{1}{r}\frac{\partial(r\rho v^2)}{\partial r} = -\frac{\partial p}{\partial r} + \Phi_r \tag{6.3}$$

$$\rho c_p \left(\frac{\partial T}{\partial t} + \vec{V} \cdot \nabla T \right) = \nabla \cdot (\lambda \nabla T) - \sum_{k=1}^{K} c_{pk} (\vec{j_k} \cdot \nabla T) - \sum_{k=1}^{K} h_k \dot{\omega}_k W_k \tag{6.4}$$

where ρ is the mixture density, $\vec{V} = (u, v)$ is the velocity vector, Φ_z and Φ_r are the viscous stress terms, λ is the mixture conductivity, $\vec{j_k} = -\rho \frac{W_k}{\bar{W}} D_{km} \nabla X_k$ is the diffusive mass flux vector, W_k is the molar mass of species k, $\bar{W} = 1/(\sum_{k=1}^{K} Y_k/W_k)$ is the molar mass of the mixture, D_{km} is the mixture average diffusion coefficient for species k relative to the rest of the multi-component mixture, X_k is the mole fraction of species k, c_{pk} is the specific heat of species k at constant pressure, c_p is the mixture specific heat at constant pressure, h_k is the enthalpy of species k, and $\dot{\omega}_k$ is the molar production rate of species k. The production rate of each species is given by the sum of the contributions of elementary reactions with Arrhenius rates. The Kth species (the last species), here N_2, is always in excessive, and its mass fraction Y_K is calculated from the identity $\sum_{k=1}^{K} Y_k \equiv 1$. The conservation equation for the kth species, $k = 1, ..., K-1$, is written as

$$\frac{\partial (\rho Y_k)}{\partial t} + \nabla (\rho \vec{V} Y_k) = -(\nabla \cdot \vec{j_k}) + \dot{\omega}_k W_k \tag{6.5}$$

The perfect gas state equation is expressed as $p_o = \rho \hat{R} T / \bar{W}$, where $\hat{R}$ is the universal gas constant. Finally, for the purposes of the numerical implementation, the time rate of change of density is found by differentiating the state equation

$$\frac{\partial \rho}{\partial t} = \rho \left(-\frac{1}{T} \frac{\partial T}{\partial t} - \bar{W} \sum_{k=1}^{K} \frac{1}{W_k} \frac{\partial Y_k}{\partial t} \right) \tag{6.6}$$

where $\partial Y_k / \partial t = [\partial (\rho Y_k)/\partial t + \nabla (\rho \vec{V}) Y_k]/\rho$ and substituting for $\partial T/\partial t$ and $\partial (\rho Y_k)/\partial t$ from the energy and species conservation equations, respectively.

In order to include the effect of the heat loss to the perforated-plate, the heat conduction equation within the burner plate is solved

$$\rho_{fh} c_{fh} \frac{\partial T}{\partial t} = \nabla \cdot (\lambda_{fh} \nabla T) \tag{6.7}$$

where ρ_{fh}, c_{fh}, and λ_{fh} are the density, specific heat and thermal conductivity of the burner plate material, respectively. For simplicity they are assumed to be constant.

6.2 Numerical solution

I simulate a flame stabilized downstream of a single perforated-With heat loss, as the flame moves away / towards the burner, its burning velocity increases / decreases, amplifying the flame motion. plate hole. The top view of the solution domain at the perforated-plate surface, $z = 0$, is shown in Fig. 6-1.

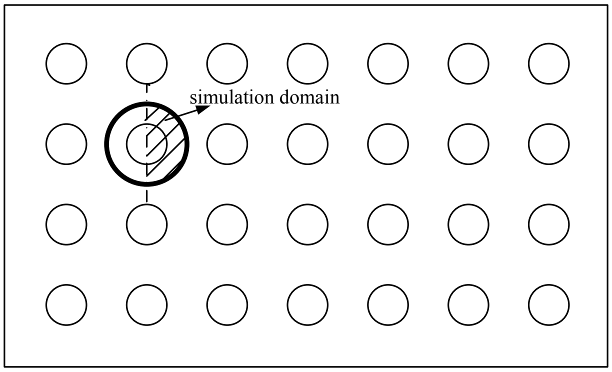

Figure 6-1: The schematic diagram showing the computational domain at the perforated-plate surface, $z = 0$.

Figure 6-2 shows a schematic diagram of the computational domain at an arbitrary angular slice, illustrating the boundary conditions specified at each surface. The conduction heat transfer between the perforated-plate and the gas mixture is considered. The radiation between the gas and the perforated-plate, and between the perforated-plate and the environment are neglected. Convective heat transfer is modeled at the bottom surface of the perforated-plate with a constant specified heat

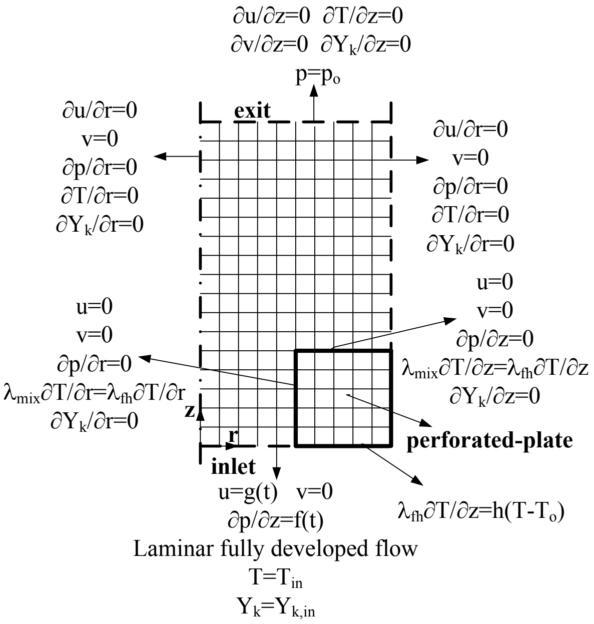

Figure 6-2: The schematic diagram showing the computational domain at an arbitrary angular slice.

transfer coefficient, h. Symmetry boundary conditions are imposed at the centerline, $r = 0$. Adiabatic, impermeable, slip-wall boundary conditions are used at the right boundary in order to model the interaction between adjacent flames. At the exit, typical out-flow boundary conditions are used. The average inlet velocity, $\bar{u}_{in}$, is either kept constant to simulate steady flames, or superposed with sinusoidal oscillations at different amplitudes and frequencies to simulate the unsteady flame response to the velocity oscillations. The mixture composition at the inlet is steady and uniform and calculated based on the specified equivalence ratio of the reactant mixture. The inlet temperature is uniform and atmospheric. The pressure gradient, and the velocity profile at the inlet are calculated solving the Navier Stokes equation in the r-direction at the inlet, with the known instantaneous average inlet velocity, using the laminar, fully developed flow assumption:

$$\rho\frac{\partial u_{in}}{\partial t} = -\frac{\partial p}{\partial z}|_{in} + \frac{\mu_{in}}{r}\frac{\partial}{\partial r}\left(r\frac{\partial u_{in}}{\partial r}\right) \tag{6.8}$$

with

$$2\pi \int_0^R u_{in}(r,t)dr = \pi R^2 \bar{u}_{in} \left[1 + \Lambda \sin(\omega t)\right] \tag{6.9}$$

where the subscript in refers to the inlet of the domain, R is the radius of the hole, Λ is the non-dimensional forcing amplitude and ω is the forcing frequency. Using Eq. (6.8) and Eq. (6.9):

$$\frac{\partial p}{\partial z}|_{in} = \frac{2\mu_{in}}{R}\frac{\partial u_{in}}{\partial r}|_R - \rho \bar{u}_{in} \Lambda \omega \cos(\omega t) \tag{6.10}$$

The pressure gradient at the inlet is calculated using Eq. (6.10). Once the pressure gradient is calculated, the velocity profile at the inlet, $u_{in}(r,t)$ is computed from Eq. (6.8), using a second-order, centered-difference discretization.

The conservation equations are solved using a second-order predictor-corrector finite-difference projection scheme. The domain is discretized using a staggered grid with uniform, but different cell sizes in each coordinate direction. Velocity components are evaluated at the cell edges, while scalars are evaluated at the cell centers. Spatial derivatives are discretized using second-order central differences. The equations are integrated using an additive (non-split) semi-implicit second-order projection scheme. The projection scheme is based on a predictor–corrector stiff approach that couples the evolution of the velocity and density fields in order to stabilize computations of reacting flows with large density variations. The predictor uses a second-order Adams–Bashforth time integration scheme to update the velocity and scalar fields and incorporates a pressure correction step in order to satisfy the continuity equation. The corrector is a mixed scheme, which combines non-split stiff integration of reaction source terms with the second-order Runge-Kutta treatment of the remaining terms. The momentum equations are integrated using the second-order Adams–Bashforth scheme as in the predictor. The stiff integrator is adapted from the CVODE package [79]. The corrector also incorporates a pressure correction step. In both sub-steps, the pressure correction step involves the inversion of the pressure Poisson equation which is implemented using Sundials banded matrix solver. The calculation of the production rates of each species and the evaluation of the thermodynamic and transport properties are performed using Cantera [58]. The code is written in C++, and paralellized using Open MP. A one-dimensional flame solution is used as the initial condition. The details about the numerical algorithm can be found in Refs. [80, 81].

I utilize a reduced methane combustion mechanism involving 20 species and 79 reactions, which is obtained by eliminating some species and the reactions from the mechanism developed by UCSD Center of Energy Research [61]. In order to obtain the reduced mechanism, I performed simulations of a premixed laminar flame stabilized in a planar stagnation flow using a one-dimensional code, which is explained before in section 2.2.4, and in detail in Refs. [60, 69]. The one-dimensional computations are performed for strain rates ranging from 12 to 9000 s^{-1}. In all cases, the oxidizer was air, the reactant mixture temperature was 300 K, and the pressure was atmospheric.

First, the one-dimensional code was run with the full UCSD mechanism. Given a set of elementary reactions that convert species A to species B, we sum the reaction rates for each of these reactions and integrate this value across the flame, obtaining the total rate at which A is converted to B. One way of displaying this information is a reaction pathway diagram, which shows the conversion rates amongst the reacting species. Figure 6-3 shows the reaction pathway diagram for a planar methane-air flame with an equivalence ratio of 0.80 and a = 12 s^{-1} containing the most active carbon-containing species obtained using the UCSD mechanism. In this figure, colors and line width are used to indicate the magnitude of each conversion rate. Each decrease in the line width in the figure indicates a halving of the corresponding conversion rate. Conversions which occur at rates of less than 1% of the rate at which

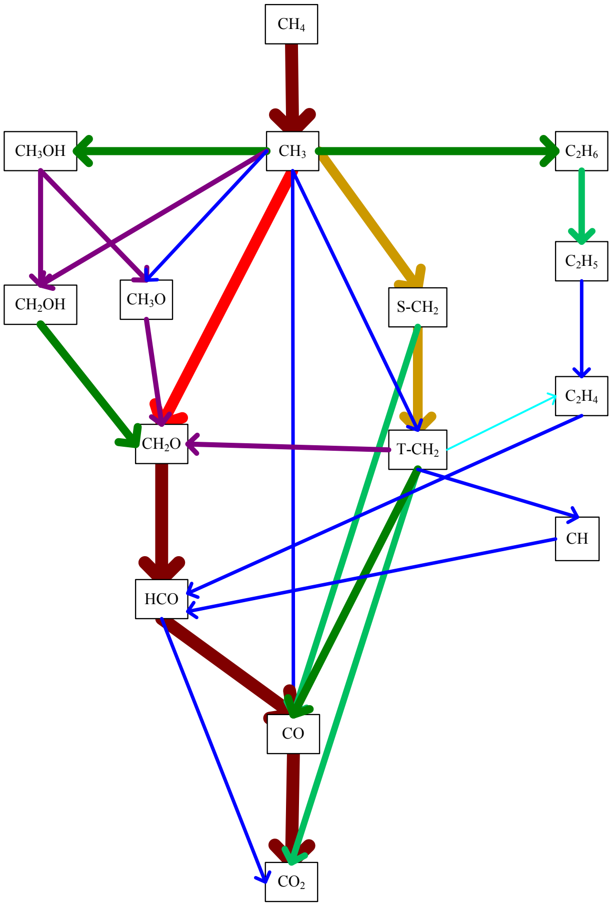

Figure 6-3: Reaction pathway diagram containing the most active carbon species.

methane is consumed, and the other carbon containing species involving these reactions are not shown. Based on this figure, I observe that the contribution of the species at the right-side branch (starting from CH_3) are not significant compared to the other major reaction pathways. Therefore, only the following species (and the reactions involving those species) were included in the reduced chemical kinetic mechanism: N_2, H, O_2, OH, O, H_2, H_2O, HO_2, H_2O_2, CO, CO_2, HCO, CH_2O, CH_4, CH_3, T-CH_2, S-CH_2, CH_3O, CH_2OH, and CH_3OH.

In order to test the validity of the reduced mechanism, I compare the flame burning velocities and the flame thicknesses calculated using the full UCSD mechanism, the reduced mechanism, and also the commonly used GRI-Mech 3.0 mechanism [82]. I use the consumption speed, S_c, to quantify the burning velocity, calculated by integrating the energy equation across the flame. The consumption speed is defined as

$$S_c = \frac{\int_{-\infty}^{\infty} q'''/c_p dy}{\rho_u \left(T_b - T_u\right)} \tag{6.11}$$

where q''' is the volumetric heat-release rate, c_p is the specific heat of the mixture, y is the coordinate normal to the flame, ρ_u is the unburned mixture density, and T_u and T_b are the unburned and burned temperature, respectively. As the strain rate parameter a approaches 0, the consumption speed approaches the laminar burning velocity.

The flame thickness is determined from the peak temperature gradient and the unburned and burned temperatures as

$$\delta_f = (T_b - T_u)/|\partial T/\partial x|_{max} \tag{6.12}$$

The laminar burning velocity, i.e. at $a = 0$, as a function of the equivalence ratio using the UCSD mechanism, the reduced mechanism and the GRI-Mech 3.0 mechanism is shown in Fig. 6-4. The laminar burning velocity is determined by extrapolating the consumption speed to a strain rate of zero, analogous to the commonly-employed technique for determining laminar burning velocity from experimentally-observed strained flames. In Fig. 6-5, I plot the flame thickness as a function of the equivalence ratio calculated for a strain rate of $a = 48$ s^{-1}, using the UCSD mechanism, the reduced mechanism, and the GRI-Mech 3.0 mechanism.

Both Fig. 6-4 and Fig. 6-5 show that in the lean equivalence ratio range, both the laminar burning velocity and the flame thickness are represented well with the reduced mechanism compared to the parent UCSD mechanism. The laminar burning velocities calculated with the UCSD mechanism (and the reduced mechanism) are lower than those calculated by the GRI-Mech mechanism, and the difference between the calculated burning velocities increases as the equivalence ratio approaches stoichiometry. In this study, because I am interested in the lean equivalence ratio range, the use of the reduced mechanism seems justified.

The domain size is as follows: the radius of the hole is 0.5 mm (the hole diameter, D=1 mm), and the radius of the simulation domain is 1 mm. The perforated-plate thickness is 13.2 mm. The distance between the top surface of the plate and the exit is 15 mm. The cell size in the flow direction is 0.04 mm, while the cell size in the radial direction is 0.02 m. Therefore, the domain is composed of 50 × 705 cells.

The code was run on a 2.66GHz CPU speed Intel Xeon - Harpertown node consisting of dual quad-core CPUs (8 processors). With the above grid resolution and the computational resources, it is observed that an integration time step of 30 ns takes approximately 1.47 s in real time. The 40 ns integration time step is the maximum that could be reached, because of the limitation imposed by the CFL condition of the species with the highest diffusivity; in this case H [83].

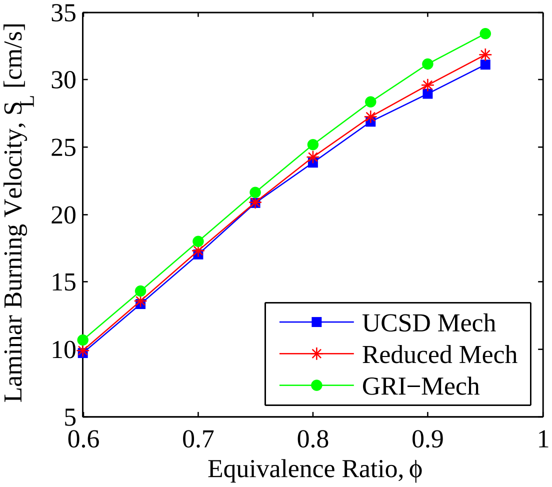

Figure 6-4: Laminar burning velocity as a function of the equivalence ratio calculated using the UCSD mechanism, the reduced mechanism and the GRI-Mech 3.0 mechanism.

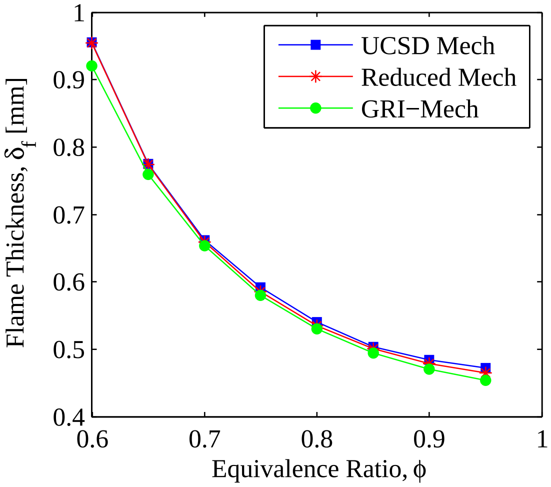

Figure 6-5: Flame thickness as a function of the equivalence ratio calculated using the UCSD mechanism, the reduced mechanism and the GRI-Mech 3.0 mechanism.

6.3 Results

I investigate the steady flame characteristics and the unsteady flame dynamics under different operating conditions, and perforated-plate characteristics. The equivalence ratio, ϕ; and the thermal conductivity of the perforated-plate material, λ_{fh}, are varied. The average inlet velocity (inside the holes), $\bar{u}_{in}$ is calculated from the total power output, P, using the specifications of the perforated-plate used in the experiments explained in detail in the previous chapter: $\bar{u}_{in} = P/(\rho_u A_{open} \Delta H)$, where A_{open} is the total hole area and ΔH is the LHV of methane per mass of the reactant mixture. In this chapter, the total power (from all holes) is kept constant at P=20 kW, a typical value of the maximum power capacity of common household burners. The power generated from a single 1 mm diameter hole simulated here is around 2.5 W.

6.3.1 Steady Flame

I investigate the steady flame structure and characteristics at three different equivalence ratios: $\phi = 0.87$, $\phi = 0.74$, and $\phi = 0.65$. The mean inlet velocity at these equivalence ratios respectively are: $\bar{u}_{in} = 1.11$ m/s , $\bar{u}_{in} = 1.29$ m/s , and $\bar{u}_{in} = 1.46$ m/s. The Reynolds numbers respectively are: Re=69, Re=80, and Re=91, which are calculated based on the hole diameter and the mean inlet velocities. The thermal conductivity of the perforated-plate material is either $\lambda_{fh} = 0$ (adiabatic plate) or $\lambda_{fh} = 1.5$ W/mK (conductive plate; porcelain thermal conductivity is used in order to model the ceramic burner).

Adiabatic Plate

First, the heat transfer between the gas and the plate is not considered by assuming an adiabatic plate, i.e. $\lambda_{fh} = 0$. In Figs. 6-6(a-c), the temperature contours at different equivalence ratios are shown. The range of the streamwise axes on the figures are chosen near the flame location, and do not represent the entire domain in that direction. The flame cools down as ϕ decreases, causing the burning velocity to drop (see Fig. 6-4). Because the power is kept constant, the decrease in the burning velocity must be compensated by the increase in the flame surface area, causing the flame tip to stabilize further downstream from the perforated-plate. In all cases, the flame is anchored near the edge of the plate; however the anchoring point moves outwards in the radial direction as ϕ decreases. Figure 6-7 shows the fuel mass fraction contours for the same cases shown in Fig. 6-6. The shape of the fuel mass fraction contours are very similar to the shape of the temperature contours, as expected for an adiabatic flame with near unity Lewis number. The fuel mass diffusion layer thicknesses are smaller than the thermal diffusion layer thicknesses. The thicker thermal diffusion layers are mainly generated as a result of the slow CO oxidation reaction.

Figure 6-8 shows the contours of the volumetric heat-release rate and the velocity

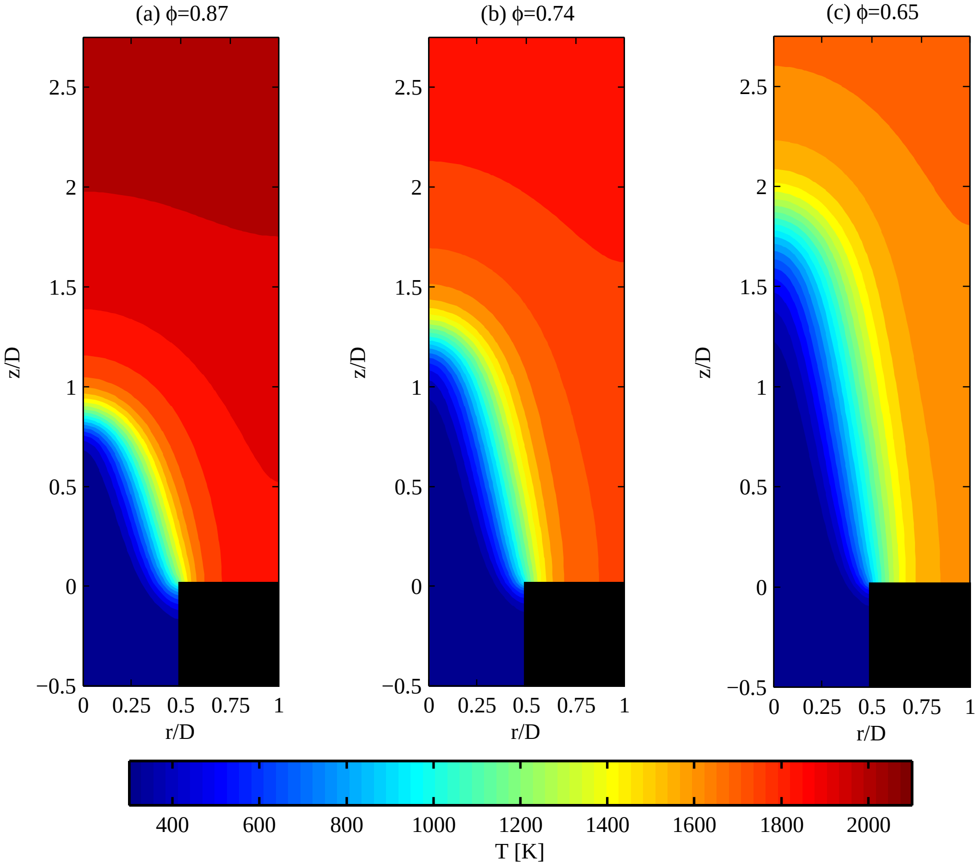

Figure 6-6: Temperature contours of steady flames with adiabatic perforated-plate at (a) $\phi = 0.87$, (b) $\phi = 0.74$, and (c) $\phi = 0.65$.

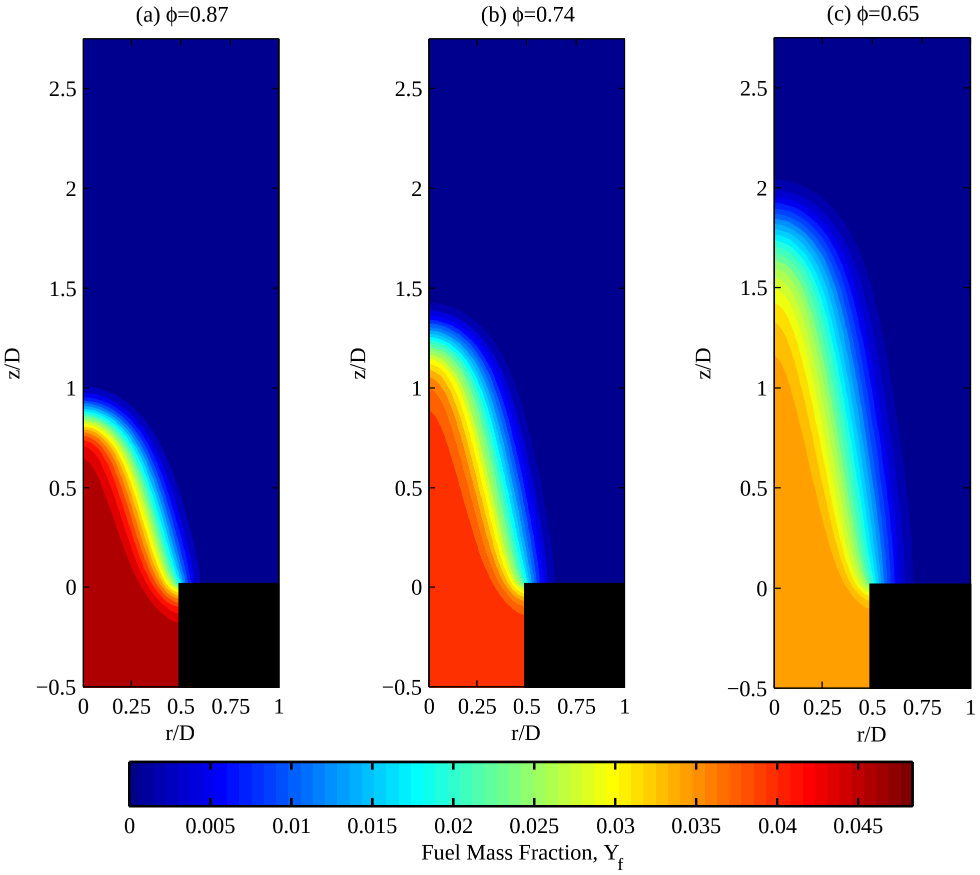

Figure 6-7: Fuel mass fraction contours of steady flames with adiabatic perforated-plate at (a) $\phi = 0.87$, (b) $\phi = 0.74$, and (c) $\phi = 0.65$.

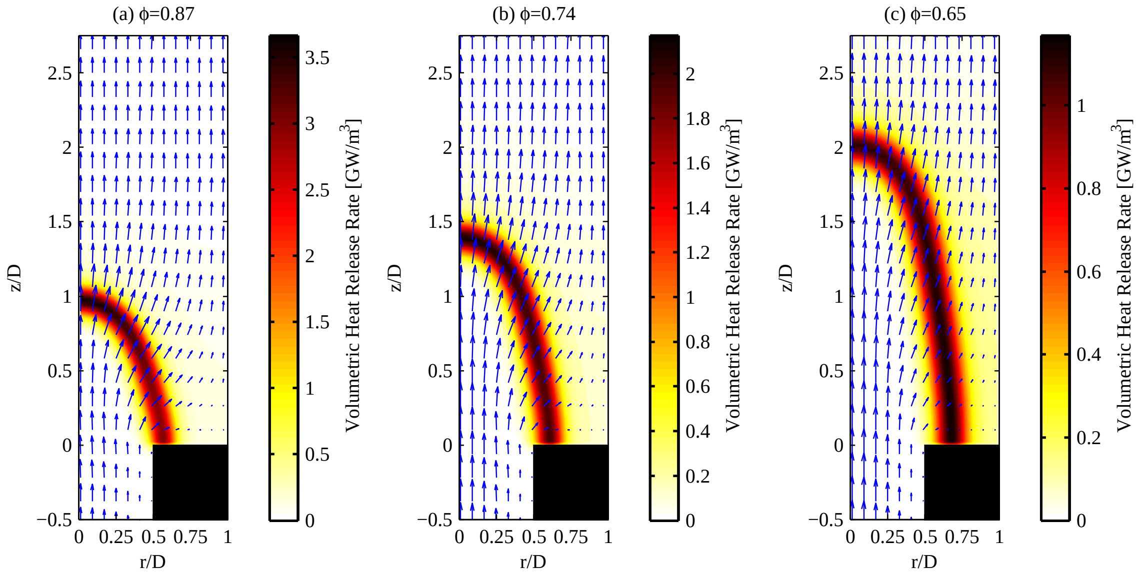

Figure 6-8: Contours of the volumetric heat-release rate and the velocity fields with adiabatic perforated-plate at (a) $\phi = 0.87$, (b) $\phi = 0.74$, and (c) $\phi = 0.65$.

vectors for the same cases. As expected, the shape of the contours at which the volumetric heat-release rate is maximum strongly matches with the shape of the temperature and mass fraction contours. The volumetric heat-release rate decreases significantly as ϕ decreases, as a result of the decrease in the flame temperature. The flame thickness increases as ϕ becomes leaner, consistent with the trend I observed in Fig. 6-5.

The formation of the recirculation zone downstream of the perforated-plate is prevented by the flame in all cases due to the elevated temperature. Near the anchoring point, the flow accelerates turns towards the flame normal direction. Due to this "turn", the reduction of the density near the flame cannot be compensated by the acceleration of the streamwise velocity alone, causing the local mass flux in the streamwise direction to decrease. From mass conservation, this decrease should be compensated by an increase in the mass flux towards the centerline. I illustrate this effect in Fig. 6-9, where I plot the streamwise velocity along the z direction for all three equivalence ratios at $r/D = 0.01$. The figure shows that at all equivalence

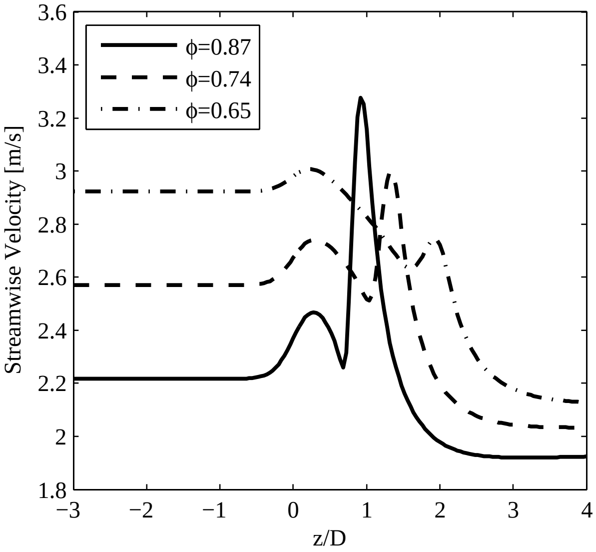

Figure 6-9: Streamwise velocities with adiabatic perforated-plate at equivalence ratios of 0.87, 0.74 and 0.65 along the streamwise direction at $r/D = 0.01$.

ratios, two peaks exist in the streamwise velocity profile. The first peak, which occurs close to $z = 0$, is generated due to the above mentioned flow-flame interactions. The second peak arises as a result of the volumetric expansion generated by the reaction, and as expected its magnitude decreases with the equivalence ratio.

Next, for all three cases, I calculate the consumption speed of the flame at the centerline (at the flame tip), $S_{c,0}$, using Eq. (6.11). The laminar burning velocities of planar unstretched flames obtained using the 1-D code (see Fig. 6-4), and the consumption speeds at the centerline are summarized in Table 6.1. It is known that negative curvature (flame concave towards the reactants) acts to increase the flame burning velocity [84, 85], when the radius of curvature of the flame is comparable with the flame thickness. As ϕ decreases, the flame thickness increases. The flame moves downstream, also causing the flame tip curvature to increase (the radius of curvature to decrease). The radius of curvature of the flame tip becomes comparable with the flame thickness, thus the consumption speed at the centerline exceeds the laminar burning velocity of a planar flame.

	$\phi = 0.87$	$\phi = 0.74$	$\phi = 0.65$
S_L [cm/s]	28.2	20.2	13.6
$S_{c,0}$ [cm/s]	27.9	21.7	15.9

Table 6.1: The laminar burning velocities of planar unstretched flames, and the flame consumption speeds at the centerline with adiabatic perforated-plate.

Conductive Plate

Now, I investigate the impact of the heat transfer between the gas mixture and the perforated-plate on the steady flame characteristics. In Fig. 6-10, the temperature contours at equivalence ratios of 0.87 and 0.74 are shown. The range of the streamwise axes on the figures are chosen near the flame location, and do not represent the entire domain in that direction. At this power, the flame blows out with the conductive plate

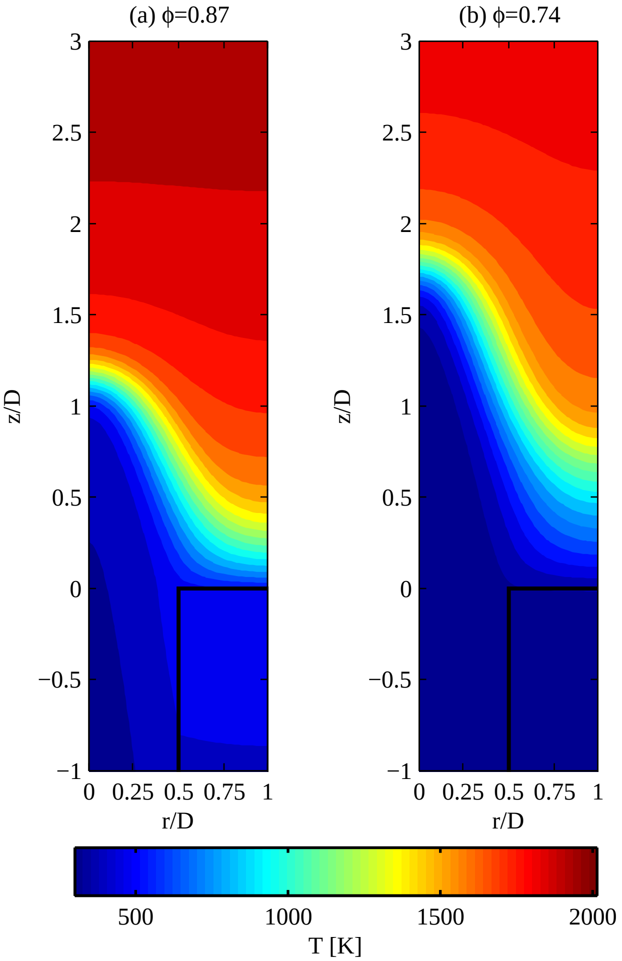

Figure 6-10: Temperature contours of steady flames with conductive perforated-plate at (a) $\phi = 0.87$, and (b) $\phi = 0.74$.

when $\phi = 0.65$. This suggests that although leaner equivalence ratios are desirable in these systems for fuel efficiency and low NO_x emissions, as the power output is increased the equivalence ratio should also be increased to prevent flame blowout. The temperature of the products decrease with ϕ; however, the cooling down of the flame as ϕ drops is not as severe as in the adiabatic cases. At both equivalence ratios, the temperature contours become horizontal downstream of the solid surfaces of the perforated-plate near the right domain boundary, suggesting that a positively curved flame (the flame convex towards the reactants) forms downstream of the plate as a result of the heat loss. Moreover, because of the heat loss, the thermal diffusion layer thickness of the positively curved flames are large. At $\phi = 0.74$, the thermal diffusion layer thickness of the positively curved flame downstream of the plate is larger than that of the negatively curved flame tip. The flame anchors a finite difference away from the plate surface, which is referred to as the flame stand-off distance.

Figure 6-11 shows the heat flux from the gas to the top surface of the perforated-plate as a function of the radial coordinate at all three equivalence ratios. The heat flux increases along the radial direction, and also with the equivalence ratio. As ϕ increases, the difference between the heat fluxes rises towards the adiabatic right surface of the computational domain. I plot the top surface temperature of the perforated-plate, T_s, as a function of the radial coordinate in Fig. 6-12. As ϕ increases, T_s also increases as a result of the higher heat flux, consistent with the trend in the model developed in the previous section. The heat flux from the perforated-plate side surface to the gas as a function of the streamwise coordinate for both equivalence ratios is shown in Fig. 6-13. The heat flux is the largest close to the top surface, and almost zero at the bottom surface at both equivalence ratios. This suggests that all the heat transferred from the gas to the plate from the top surface is transferred back to the gas from the side surface, conserving the total enthalpy. The thermal energy is recycled through the plate.

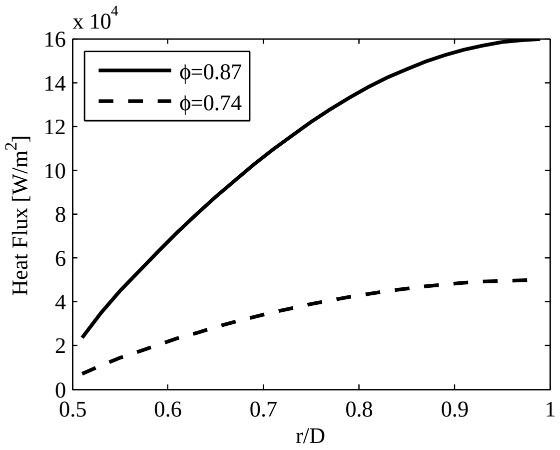

Figure 6-11: Heat flux from the gas to the perforated-plate top surface as a function of r/D at $\phi = 0.87$, and $\phi = 0.74$.

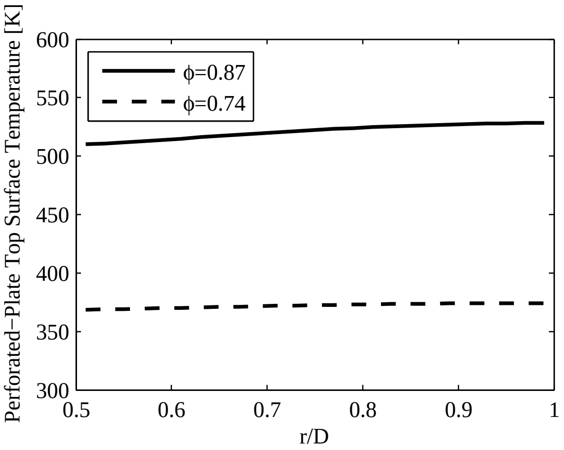

Figure 6-12: Perforated-plate top surface temperatures as a function of r/D at $\phi = 0.87$, and $\phi = 0.74$.

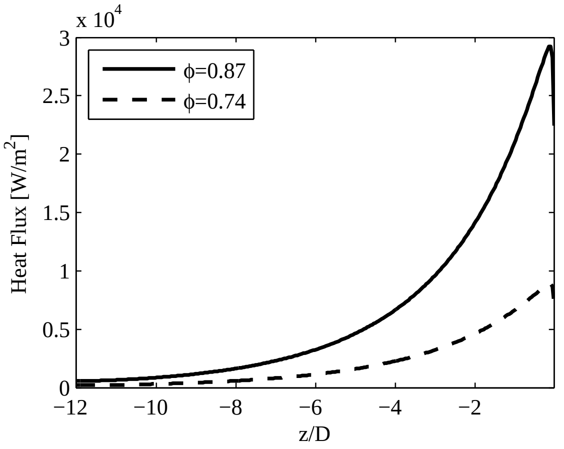

Figure 6-13: Heat flux from the perforated-plate side surface to the gas as a function of z/D at $\phi = 0.87$, and $\phi = 0.74$.

In Fig. 6-14, I plot the fuel mass fraction contours for the same cases shown in Fig. 6-10. The shape of the fuel mass fraction contours are significantly different than the shape of the temperature contours; the presence of heat transfer between the gas and the perforated-plate creates significant mismatch between the temperature and species profiles. As ϕ increases, this mismatch becomes more significant downstream of the plate surface due to higher heat transfer rate.

Figure 6-15 shows the contours of the volumetric heat-release rate and the velocity vectors. At both values of ϕ, the maximum value of the volumetric heat-release rate which is achieved near the flame tip is lower compared to the cases with adiabatic perforated-plate. However, the amount of reduction drops as ϕ decreases. Because the flame moves away from the plate, the temperature downstream of the plate is lower compared to the cases with an adiabatic plate, which allows a narrow recirculation zone to form.

In Table 6.2, I summarize the consumption speeds at the centerline, $S_{c,0}$ (at the flame tip), and along the z direction at $r/D = 1$, $S_{c,1}$. As shown in Table 6.2, the values of $S_{c,0}$ are lower than their baseline values, i.e. cases with an adiabatic plate. As ϕ decreases, the reduction in $S_{c,0}$ is less severe. The values of $S_{c,1}$ increase as ϕ decreases. As mentioned above, the heat transfer between the gas and the plate creates significant mismatch between the temperature and species profiles downstream of the plate surface. As ϕ is reduced, this mismatch is less significant due to lower heat loss rate. In fact, at $\phi = 0.74$ $S_{c,1} > S_{c,0}$, although the maximum value of the volumetric heat-release rate along the z direction at $r/D = 1$ is smaller than that at the centerline, suggesting that the large flame thickness downstream of the plate generates significant burning rate. These observations show that at an equivalence ratio in the range $0.74 < \phi < 0.87$, $S_{c,1} = S_{c,0}$, similar to the assumption of the theoretical model developed in the previous chapter. The structure and characteristics of the positively curved flame formed downstream of the plate should be investigated

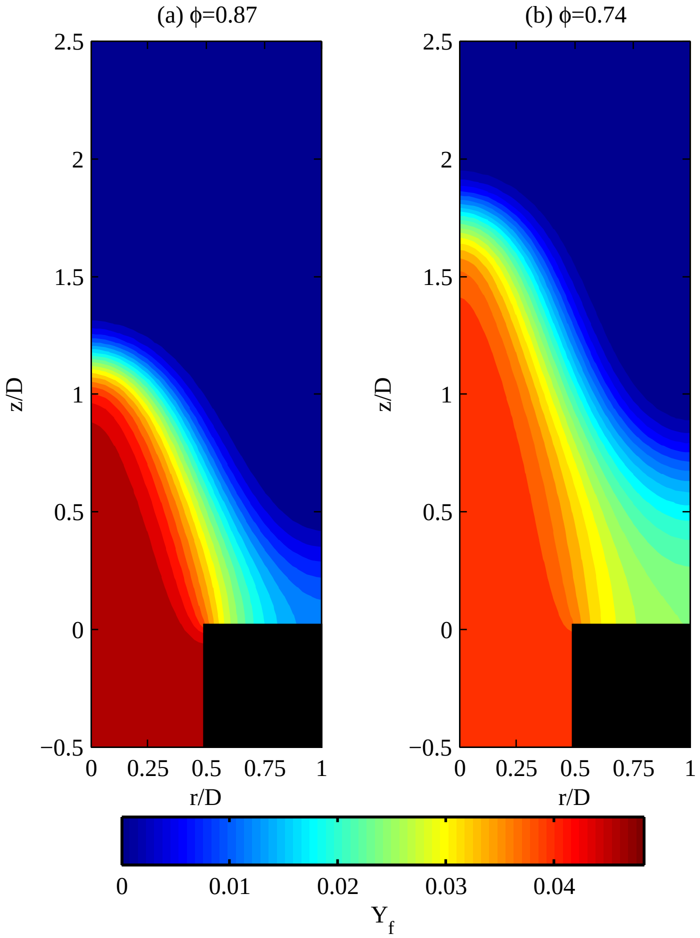

Figure 6-14: Fuel mass fraction contours of steady flames with conductive perforated-plate at (a) $\phi = 0.87$, and (b) $\phi = 0.74$.

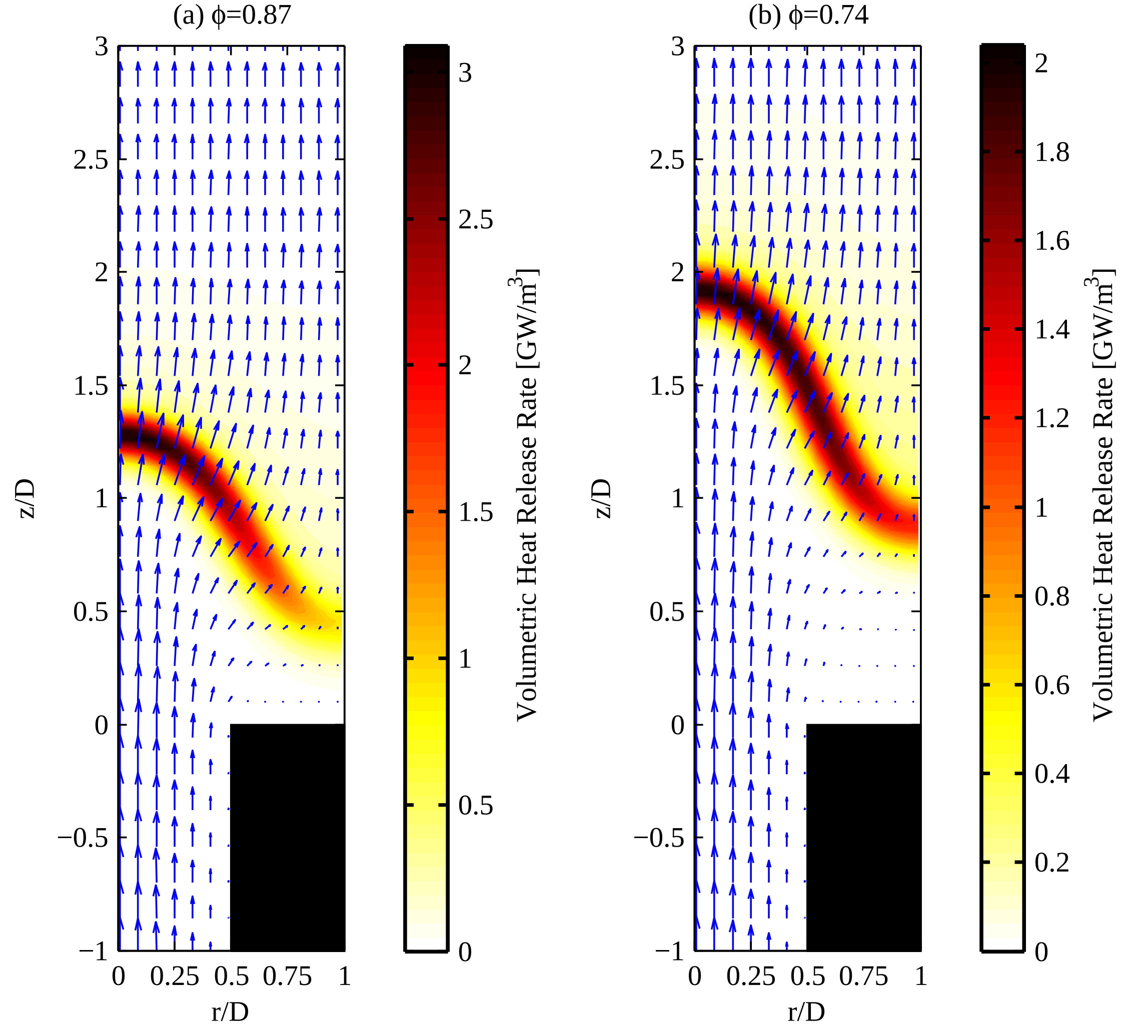

Figure 6-15: Contours of the volumetric heat-release rate and the velocity fields with conductive perforated-plate at (a) $\phi = 0.87$, and (b) $\phi = 0.74$.

in detail in the future.

	$\phi = 0.87$	$\phi = 0.74$
$S_{c,0}$ [cm/s]	26.4	21.1
$S_{c,1}$ [cm/s]	18.3	22.3

Table 6.2: The flame consumption speeds at the centerline and along the z direction at r/D=1 with conductive perforated-plate.

6.3.2 Unsteady Flame Dynamics

I force the mean inlet velocity sinusoidally, and investigate the unsteady flame dynamics. The forcing frequency is 200 Hz (higher than the resonant frequencies observed in the previous chapter), and the normalized forcing amplitudes are 10% or 70%. The simulations were performed both with the adiabatic and the conductive perforated-plates. I report the results only at $\phi = 0.74$.

Adiabatic Plate

First, the plate is adiabatic, i.e. $\lambda_{fh} = 0$. In Fig. 6-16, I plot the normalized heat-release rate, Q^*, mean inlet velocity, u^*_{in}, consumption speed at the centerline, $S^*_{c,0}$, and flame area, A^*_f, as a function of time during a representative cycle of oscillations when the forcing amplitude is 70%. Figure 6-17 shows the volumetric heat-release rate contours at the instants shown by markers on Fig. 6-16. In order to calculate the flame area, the flame is assumed to be located along the curve where the volumetric heat-release rate is at its maximum value. All the quantities are normalized with

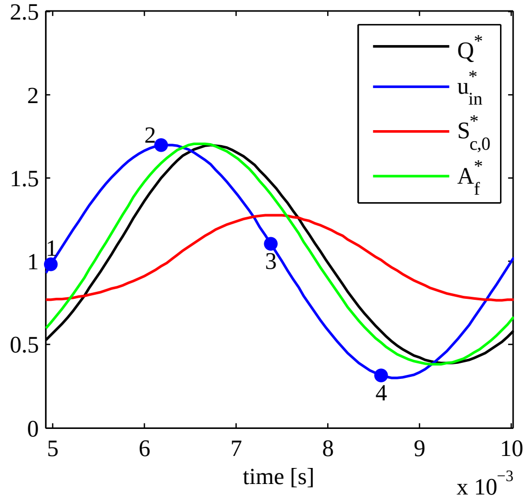

Figure 6-16: Normalized total heat-release rate, Q^*, mean inlet velocity, u^*_{in}, consumption speed at the centerline, $S^*_{c,0}$, and flame area, A^*_f, as a function of time during a representative cycle when the forcing frequency is 200 Hz, and the forcing amplitude is 70% of the mean velocity with adiabatic perforated-plate at $\phi = 0.74$.

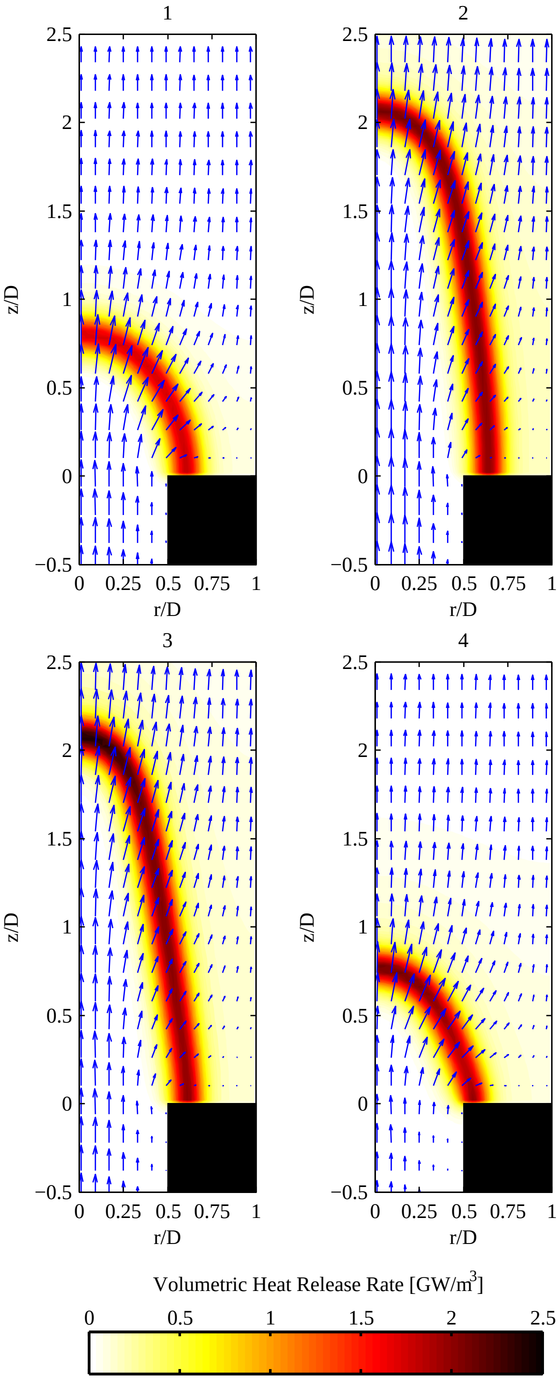

Figure 6-17: Sequential contours of the volumetric heat-release rate and the velocity fields with adiabatic perforated-plate at $\phi = 0.74$. The number on each image corresponds to the instant shown in Fig. 6-16.

their steady values.

The heat-release rate oscillations are in-phase with the flame-area oscillations, and lag the velocity by 25 degrees. The heat-release oscillation amplitude, the forcing amplitude, and the flame area amplitude match each other. This concludes that the heat-release rate oscillations arise as a result of the flame-area oscillations. The strong change in the flame area could be clearly observed in Fig. 6-17. The consumption speed at the centerline oscillates at lower amplitude, around 25% of its mean value and lags the velocity by 82 degrees. The consumption speed oscillates mainly as a result of the change in the flame tip curvature. As the inlet velocity increases, the flame tip moves downstream as shown in Fig. 6-17 causing the curvature of the flame tip to increase. As a result, the consumption speed increases, i.e. the volumetric heat-release rate contours get darker. Because the flame cannot adjust itself instantaneously to the changes in its curvature, the consumption speed oscillations lag the velocity oscillations.

Next, I repeated the simulations by reducing the forcing amplitude to 10% of the mean inlet velocity. Again, the overall dynamics are similar; the heat release response is governed by the flame area oscillations as shown in Fig. 6-18. This shows that the non-linear effects are not strong.

Conductive Plate

Now, I allow for the heat transfer between the gas and the plate. The specific heat and the density of the plate are taken as: c_{fh} =1070 J/kgK, and ρ_{fh} = 2400 kg/m^3 (porcelain properties).

In Fig. 6-19, I plot the normalized heat-release rate, Q^*, mean inlet velocity, u^*_{in}, consumption speed at the centerline, $S^*_{c,0}$, consumption speed at $r/D = 1$, $S^*_{c,1}$, and flame area, A^*_f, as a function of time during a representative cycle when the forcing amplitude is 70%. Figure 6-20 shows the volumetric heat-release rate contours at the

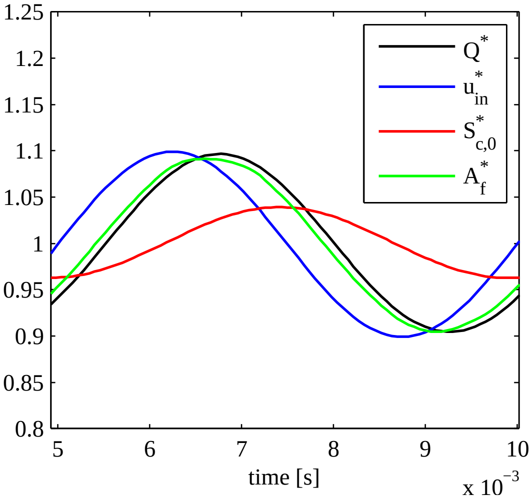

Figure 6-18: Normalized total heat-release rate, Q^*, mean inlet velocity, u^*_{in}, consumption speed at the centerline, $S^*_{c,0}$, and flame area, A^*_f, as a function of time during a representative cycle when the forcing frequency is 200 Hz, and the forcing amplitude is 10% of the mean velocity with adiabatic perforated-plate at $\phi = 0.74$.

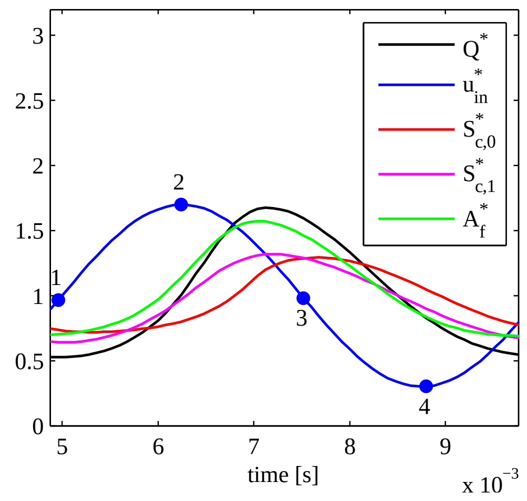

Figure 6-19: Normalized total heat-release rate, Q^*, mean inlet velocity, u^*_{in}, consumption speed at the centerline, $S^*_{c,0}$, consumption speed at $r/D = 1$, $S^*_{c,1}$, and flame area, A^*_f, as a function of time during a representative cycle when the forcing frequency is 200 Hz, and the forcing amplitude is 70% of the mean velocity with conductive perforated-plate at $\phi = 0.74$.

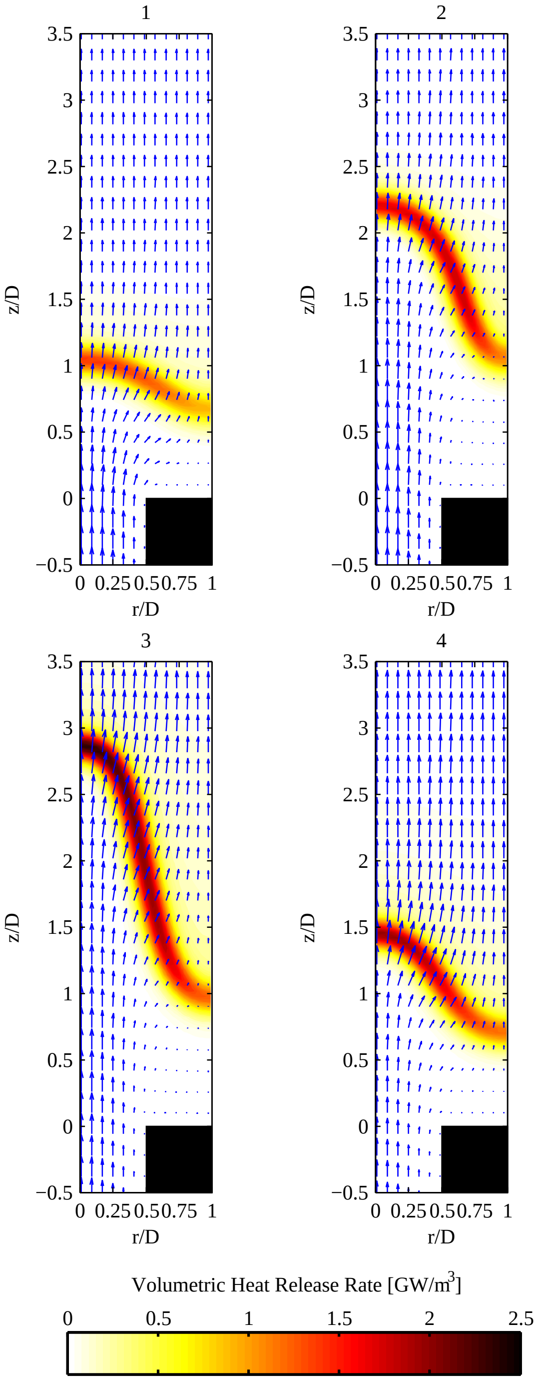

Figure 6-20: Sequential contours of the volumetric heat-release rate and the velocity fields with conductive perforated-plate at $\phi = 0.74$. The number on each image corresponds to the instant shown in Fig. 6-19.

instants shown by markers on Fig. 6-19.

Figure 6-19 shows that the heat-release rate is almost in-phase with the consumption speed at $r/D = 1$, and the flame area oscillations, while the consumption speed at the centerline lags them by approximately 35 degrees. The oscillation amplitude of the consumption speed at $r/D = 1$ is 25% and smaller than the oscillation amplitude of the flame area, which is around 55% of its mean value. At this operating condition with gas-plate heat transfer, the heat-release rate oscillations arise both by the consumption speed and the flame area oscillations; the effect of the flame area oscillations is more significant. The consumption speed at $r/D = 1$ oscillates as the positively curved flame downstream of the plate surface propagates towards/away from the perforated-plate as a result of the change in the amount of heat transferred to the plate. Similar to the baseline adiabatic plate cases, the consumption speed at the centerline oscillates primarily due to the changes in the flame tip curvature. The heat-release rate lags the inlet velocity by approximately 63 degrees, which is higher compared to the baseline case as a result of the additional impact of the consumption speed on the heat-release rate. As the forcing frequency approaches the resonant frequency (see Fig. 5-4), the consumption speed oscillations become very strong, causing the heat-release rate to oscillate at a larger amplitude than the forcing amplitude. In that case, if the acoustic frequencies of the burner system matches the frequencies at which this behavior occurs, strong self-sustained oscillations are generated. This is a characteristic behavior of the perforated-plate stabilized flames with heat transfer to the plate, originated from the consumption speed oscillations of the positively curved flame downstream of the plate [21, 22, 29, 86].

When the inlet velocity accelerates at its maximum value (instant 1), the flame is nearly flat and the total burning rate is small. Because the consumption speed at the centerline is near its minimum value, the flame tip moves downstream quickly as the inlet velocity increases, causing the flame area to increase. As the flame tip moves downstream, the consumption speed near the flame tip increases as a result of the increase in the flame tip curvature. The consumption speed of the positively curved flame downstream of the plate surface also increases, because it anchors further away from the plate surface, causing the heat loss to decrease. The inlet velocity reaches its maximum value at instant 2. As the inlet velocity drops from its maximum value, the positively curved flame moves towards the plate, its consumption speed drops. Although the inlet velocity drops, the flame tip propagates further downstream. The consumption speed of the flame tip increases due to the increase in its curvature.

In order to explain this phenomenon, in Fig. 6-21, I plot the streamwise velocity along the z direction at $r/D = 0.01$ at instants 2 and 3. Although the inlet velocity is lower, the velocity near the flame, and the velocity of the products are significantly higher at instant 3, compared to instant 2, causing the flame tip to move downstream.

When the inlet velocity decreases to its mean value (instant 3), the consumption speed at the centerline reaches its maximum value. As the velocity drops towards its minimum value, the flame tip with high consumption speed quickly propagates towards the plate, causing the flame area and the flame tip curvature to decrease. The positively curved flame continues to propagate towards the plate causing further

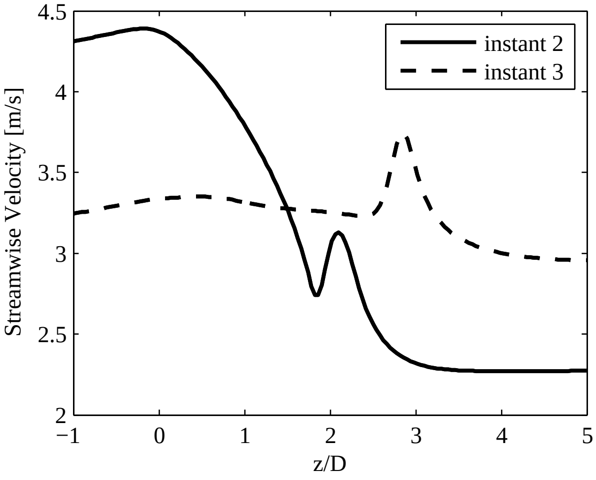

Figure 6-21: Streamwise velocity along the z direction at $r/D = 0.01$, at instants 2 and 3.

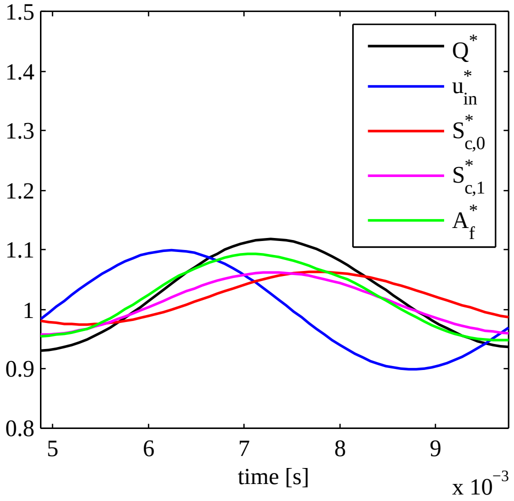

Figure 6-22: Normalized total heat-release rate, Q^*, mean inlet velocity, u^*_{in}, consumption speed at the centerline, $S^*_{c,0}$, consumption speed at $r/D = 1$, $S^*_{c,1}$, and flame area, A^*_f, as a function of time during a representative cycle when the forcing frequency is 200 Hz, and the forcing amplitude is 10% of the mean velocity with conductive perforated-plate at $\phi = 0.74$.

reduction in the consumption speed in that region. When the inlet velocity is at its minimum value (instant 4), the consumption speed at the centerline is smaller due to the decrease in the flame tip curvature. As the velocity recovers, the flame tip moves towards the plate although the inlet velocity increases, because the velocity near the flame is lower at instant 1 compared to instant 4. The consumption speed at the flame tip drops further as a result of the reduction in the flame tip curvature. When the inlet velocity reaches its mean value again, the entire flame is nearly flat with low burning rate. The velocity starts to increase towards its maximum value, and the cycle repeats.

Next, I repeated the simulations by reducing the forcing amplitude to 10%. As shown in Fig. 6-22, the overall dynamics are similar; the heat release response is governed by the consumption speed and the flame area oscillations, the latter being more significant. The similarity of the dynamics at two different amplitudes show that the the non-linear effects are not strong.

6.4 Summary

In this chapter, I performed two-dimensional simulations of laminar methane-air flames stabilized downstream of a perforated-plate using a reduced chemical kinetic mechanism for methane combustion in air. I solved for the temperature profile within the perforated-plate by allowing heat transfer between the gas mixture and the solid plate. The inlet velocity was either kept constant to examine the steady flame characteristics, or forced sinusoidally at 200 Hz to investigate the unsteady flame response to inlet velocity oscillations.

When the gas-plate heat transfer is neglected, a conical flame with negatively curved flame tip forms downstream of the holes, which is anchored near the edge of the plate. As the equivalence ratio decreases, the consumption speed of the flame drops, causing the flame tip to stabilize further away from the plate surface, which increases the total flame area. The consumption speed calculated at the centerline exceeds the laminar burning velocity of planar flames as a result of the curvature of the flame tip. When the inlet velocity is forced sinusoidally, the heat release dynamics are governed only by the flame-area oscillations.

When the gas-plate heat transfer is allowed, a positively curved flame forms downstream of the plate surface. As the equivalence ratio increases, the heat transfer to the plate rises, the flame moves closer to the perforated-plate, which increases the plate's surface temperature consistent with results of the theoretical model. As the equivalence ratio decreases, the burning velocity of the negatively curved flame tip decreases, while the burning velocity of the positively curved flame downstream of the plate increases. At a particular value of the equivalence ratio depending on the plate geometry and material, the burning velocity along the flame surface becomes uniform, which is the key assumption of the analytical model. When the inlet velocity is forced, the heat release dynamics are governed both by the burning velocity oscillations and the flame-area oscillations.

Chapter 7

Conclusions

In this thesis, I examined the combustion dynamics of wake-stabilized and perforated-plate stabilized flames.

The wake-stabilized flame dynamics were investigated experimentally in an atmospheric pressure, model backward-facing step combustor. I carried out a parametric study by varying the equivalence ratio, the Reynolds number, the inlet temperature, the fuel composition and the location of the fuel injector to examine the flame-vortex interactions and the equivalence ratio oscillations, and the relative contribution of these mechanisms on the dynamics.

When the fuel is injected far upstream from the step, the equivalence ratio arriving at the flame is steady; the dynamics are driven by the flame-vortex interaction mechanism alone. In that case, the effect of the Reynold number on the dynamics is negligible. Four distinct operating modes are observed depending on the inlet temperature, equivalence ratio and the fuel composition. At high but lean equivalence ratios, the combustor is unstable as a result of the strong interaction between the large unsteady wake vortex and the flame. The flame propagates upstream of the step during a part of the cycle. At intermediate equivalence ratios, the combustor operates in the quasi-stable mode with the flame staying attached to the step at all times. Near the blowout limit, long stable flames are observed. When the inlet temperature is atmospheric, the quasi-stable and the unstable flames couple with the 1/4 wavemode of the combustor. When the inlet temperature is increased, at high but lean equivalence ratios, the 5/4 wavemode of the combustor is excited, increasing the resonant frequency significantly. This operating mode is the high-frequency unstable mode, where the flame is more compact compared to the unstable case. Increasing the inlet temperature and hydrogen concentration shifts the response curves of the combustor towards lower equivalence ratios. As the inlet temperature is increased, the stable operating band becomes narrower. The vertical velocity of the large wake vortex is proportional to the heat release parameter, and controls the moment when the vortex reaches the upper wall of the combustor producing a heat release pulse. I demonstrated that the consumption speed of strained flames can be used to collapse the response curves describing the transitions among different dynamic modes onto a function of the heat release parameter alone. I predicted the critical values of the heat release parameter at which transitions between quasi-stable to unstable, and unstable to high-frequency unstable operating modes take place, which may provide significant benefits during the design stage of the combustors.

When the fuel is injected close to the step, the equivalence ratio arriving at the flame oscillates. In this case the equivalence ratio oscillations impact the combustion dynamics. I showed that independent of the phase between the equivalence ratio arriving at the flame and the pressure oscillations, the unsteady interactions between the flame and the vortex were still dominant, because the local equivalence ratio near the vortex during burning is large enough to drive the unstable dynamics. Therefore, the combustion dynamics is primarily governed by the flame-vortex interactions. However, the equivalence ratio oscillations have secondary effects on the dynamics: (i) When there is no flow reversal, the amplitude of the acoustic oscillations change in each cycle governed by the local flame blowout near the step;

(ii) When the equivalence ratio arriving at the flame is in-phase with the pressure oscillations, stronger heat-release rate oscillations are generated at the entire range of mean equivalence ratios, further contributing to the instability; and (iii) The mean equivalence ratio at the lean blowout limit is higher compared to the case when the dynamics are driven by the flame-vortex interactions alone. Therefore, the equivalence ratio oscillations are undesirable when the combustion dynamics are primarily governed by the flame-vortex interactions. In order to eliminate the equivalence ratio oscillations oxidizer-fuel premixing strategies allowing for longer mixing time or faster mixing rate should be developed.

A simple, instability mitigation strategy by injecting steady air flow near the flame anchoring zone in the cross-stream and the streamwise directions through choked micro-holes was proposed and tested. At operating conditions when the flame detaches from the step and flashes back into the upstream channel without air injection, when air was injected in the cross-stream direction, the flame anchors slightly upstream of the step in the "new, stable, aerodynamically created" intense recirculation zone formed near the upper wall of the combustor, instead of on the unsteady recirculation zone forming downstream of the step. As a result, the flame dynamics are stabilized. On the other hand, at operating conditions corresponding to the unstable and high-frequency unstable operating modes of the combustor without air injection, air injection in the cross-stream direction is ineffective in stabilizing the dynamics, which is still governed by the flame-vortex interactions. In these cases, the 3/4 wavemode of the combustor, in addition to the 1/4 and the 5/4 wavemodes is excited. When air is injected in the streamwise direction near the edge of step, both the unstable and the high-frequency unstable dynamics could be stabilized at an optimum secondary air flow rate which depends on the operating conditions. When effective, the secondary air flow suppresses the shedding of an unsteady vortex, and hence the flame-vortex interaction mechanism. Instead, a compact, stable flame is formed near the step. On the other hand, when air injection in the streamwise direction is ineffective, the flame blows out near the step; instead it anchors at the hot top wall of of the combustor. In this case, the flame is unsteady, the flame-vortex interactions are strong, and the dynamics are distinct compared to that at the unstable and high-frequency unstable modes. Therefore, suppression of the instability could only be achieved by blocking the interaction between the flame and the unsteady wake vortex, the primary mechanism creating the instability.

The perforated-plate stabilized flame dynamics were modeled analytically by considering the coupled unsteady heat release mechanisms of flame-acoustic wave interactions, and the flame-wall interactions. The dynamic planar flame models of perforated-plate stabilized flames were extended to account for the formation of the conical flame surfaces downstream of the perforated-plate holes in order to introduce the effect of flame-area fluctuations. As a result of the heat loss to the solid plate, the flame moves away / towards the plate surface, its burning velocity increases / decreases, amplifying the flame motion. At a particular resonant frequency, the flame propagates between the absolute minimum/maximum distances from the plate in one cycle, generating strong self-sustained heat-release rate oscillations. At low frequencies with respect to the resonant frequency, the contribution of flame-area oscillations to the net heat-release rate is weak compared to that of the burning velocity oscillations. At these frequencies, flame-area oscillations arise both due to the impact of inlet velocity and burning velocity oscillations. When the frequency is high with respect to the resonant frequency, only flame-area oscillations contribute to the net heat-release rate fluctuations, which arise as a result of the inlet velocity fluctuations. The conical flame surface area increases at high inlet velocity and low equivalence ratio, increasing the impact of the flame-area oscillations. When the heat transfer to the plate is significant, the burning velocity drops, the burner plate surface temperature rises and the resonant frequency increases. Thus, the flame-area oscillations impact the heat-release rate response at higher frequencies. This model could be extended further upon taking into account the effect of expansion velocity while modeling the conical flame surfaces, treating the heat transfer inside the burner in more detail, and using more realistic velocity profiles.

In order to include these effects, and verify some of the assumptions of this model, a two-dimensional code utilizing a detailed chemical kinetic mechanism was developed to simulate the steady flame characteristics and the dynamic response of the flame to inlet velocity oscillations. When the gas-plate heat transfer is neglected, a conical flame with negatively curved flame tip forms downstream of the holes, which is anchored near the edge of the plate. As equivalence ratio decreases, the burning velocity of the flame drops, causing the flame tip to stabilize further away from the plate surface, which increases the total flame area. The burning velocity of the flame calculated at the centerline exceeds the laminar burning velocity of planar unstretched flames as a result of the strong curvature of the flame tip. When the inlet velocity is forced sinusoidally at high frequency, the heat release dynamics are governed only by the flame-area oscillations.

When the gas-plate heat transfer is allowed, a positively curved flame forms downstream of the plate surface. As the equivalence ratio increases, the heat transfer to the plate increases, the positively curved flame moves closer to the perforated-plate, which increases the plate's surface temperature consistent with the assumptions of the theoretical model. As the equivalence ratio decreases, the burning velocity of the negatively curved flame tip decreases, while the burning velocity of the positively curved flame downstream of the plate increases. At a particular value of the equivalence ratio, depending on the plate geometry and material, the burning velocity along the flame surface becomes uniform, which is the key assumption of the analytical model. When the inlet velocity is forced at high frequency, the heat release dynamics are governed both by the burning velocity oscillations and the flame-area oscillations, the impact of the latter being more significant. As the forcing frequency is dropped close to the resonant frequency, the burning velocity oscillations become more significant; the heat-release rate oscillation amplitude exceeds the forcing amplitude, which makes the burner system susceptible to strong self-sustained oscillations. The range of operating conditions, the forcing frequencies and amplitudes should be expanded in future studies in order to determine the detailed heat release-inlet velocity transfer functions.

Bibliography

[1] L. Rayleigh. *The Theory of Sound*, volume 2, pages 224–234. Macmillan, London, 2nd edition, 1896.

[2] W. C. Strahle. On combustion generated noise. *Journal of Fluid Mechanics*, 49(2):399–414, 1971.

[3] A. P. Dowling. Instability in lean premixed combustors. *Proc, Inst. Mechanical Engineers*, 214(Part A):317–331, 2000.

[4] S. Ducruix, T. Schuller, D. Durox, and S. Candel. Combustion dynamics and instabilities: Elementary coupling and driving mechanisms. *Journal of Propulsion and Power*, 19(5):722–733, 2003.

[5] T. Lieuwen. Modeling premixed combustion-acoustic wave interactions: A review. *Journal of Propulsion and Power*, 19(5):765–781, 2003.

[6] K. K. Venkataraman, B. J. Lee, L. H. Preston, D. W. Simons, J. G. Lee, and D. A. Santavicca. Mechanism of combustion instability in a lean premixed dump combustor. *Journal of Propulsion and Power*, 15(6):909–918, 1999.

[7] D. Bernier, F. Lacas, and S. Candel. Instability mechanisms in a premixed prevaporized combustor. *Journal of Propulsion and Power*, 20(4):648–656, 2004.

[8] T. J. Poinsot, A. C. Trouve, D. Veynante, S. Candel, and E. Esposito. Vortex-

driven acoustically coupled combustion instabilities. *Journal of Fluid Mechanics*, 177:265–292, 1987.

[9] K. C. Schadow, E. Gutmark, T. P. Parr, D. M. Parr, K. J. Wilson, and J. E. Crump. Large-scale coherent structures as drivers of combustion instability. *Combustion Science and Technology*, 64:167–186, 1989.

[10] K. H. Yu, A. Trouve, and J. W. Daily. Low-frequency pressure oscillations in a model ramjet combustor. *Journal of Fluid Mechanics*, 232:47–72, 1991.

[11] H. N. Najm and A. F. Ghoniem. Coupling between vorticity and pressure oscillations in combustion instability. *Journal of Propulsion and Power*, 10(6):769–776, 1994.

[12] D. Thibaut and S. Candel. Numerical study of unsteady turbulent premixed combustion: Application to flashback simulation. *Combustion and Flame*, 113(1-2):53–65, 1998.

[13] C. Fureby. A computational study of combustion instabilities due to vortex shedding. *Proc. Combust. Inst.*, 28:783–791, 2000.

[14] Y. Huang, H. G. Sung, S. Y. Hsieh, and V. Yang. Large-eddy simulation of combustion dynamics of lean-premixed swirl-stabilized combustor. *Journal of Propulsion and Power*, 19(5):782–794, 2003.

[15] A. F. Ghoniem, A. Annaswamy, S. Park, and Z. C. Sobhani. Stability and emissions control using air injection and H_2 addition in premixed combustion. *Proceedings of the Combustion Institute*, 30:1765–1773, 2005.

[16] T. C. Lieuwen and V. Yang, editors. *Combustion instabilities in gas turbine engines*, volume 210. AIAA, 2005.

[17] J. P. Hathout, M. Fleifil, A. M. Annaswamy, and A. F. Ghoniem. Heat-release actuation for control of mixture-inhomogeneity-driven combustion instability. *Proc. Combust. Inst.*, 28:721–730, 2000.

[18] J. G. Lee, K. Kwanwoo, and D. A. Santavicca. Measurement of equivalence ratio fluctuation and its effect on heat release during unstable combustion. *Proc. Combust. Inst.*, 28:415–421, 2000.

[19] T. Lieuwen, H. Torres, C. Johnson, and B.T. Zinn. A mechanism of combustion instability in lean premixed gas turbine combustors. *Journal of Engineering for Gas Turbine and Power*, 123(1):182–189, 2001.

[20] H. Santosh, Shreekrishna, and T. Lieuwen. Premixed flame response to equivalence ratio perturbations. In *45th AIAA Aerospace Sciences Meeting*, January 2007. AIAA-2007-5656.

[21] D. Durox, T. Schuller, N. Noiray, and S. Candel. Experimental analysis of nonlinear flame transfer functions for different flame geometries. *Proc. Combust. Inst.*, 32:1391–1398, 2009.

[22] A. C. McIntosh and J. F. Clarke. 2nd order theory of unsteady burner-anchored flames with arbitrary lewis number. *Combustion Science and Technology*, 38(3-4):161–196, 1984.

[23] M. Fleifil, A. M. Annaswamy, Z. A. Ghoneim, and A. F. Ghoniem. Response of a laminar premixed flame to flow oscillations: A kinematic model and thermoacoustic instability results. *Combustion and Flame*, 106(4):487–510, 1996.

[24] S. Ducruix, D. Durox, and S. Candel. Theoretical, and experimental determinations of the transfer function of a laminar premixed flame. *Proc. Combust. Inst.*, 28:765–773, 2000.

[25] P. G. Mehta, M. C. Soteriou, and A. Banaszuk. Impact of exothermicity on steady and linearized response of a premixed ducted flame. *Combustion and Flame*, 141(4):392–405, 2005.

[26] A. C. McIntosh. On the cellular instability of flames near porous-plug burners. *Journal of Fluid Mechanics*, 161:43–75, 1985.

[27] A. C. McIntosh. On the effect of upstream acoustic forcing and feedback on the stability and resonance behavior of anchored flames. *Combustion Science and Technology*, 49(3-4):143–167, 1986.

[28] A. C. McIntosh. Combustion-acoustic interaction of a flat flame burner system, enclosed within an open tube. *Combustion Science and Technology*, 54(1-6):217–236, 1987.

[29] R. Rook, L. P. H. de Goey, L. M. T. Somers, K. R. A. M. Schreel, and R. Parchen. Response of burner-stabized flat flames to acoustic perturbation. *Combustion Theory and Modeling*, 6:223–219, 2002.

[30] R. Rook. *Acoustics in Burner Stabilized Flames*. PhD thesis, Eindhoven University of Technology, Eindhoven, The Netherlands, 2001. `www.tue.nl/bib/`.

[31] T. Yoshimura and V. G. McDonnell G. S. Samuelsen. Evaluation of hydrogen addition to natural gas on the stability and emissions behavior of a model gas turbine combustor. In *50th ASME Turbo Expo Conference*, June 2005. ASME Paper GT2005-68785.

[32] L. Figura, J. G. Lee, B. D. Quay, and D. A. Santavicca. The effects of fuel composition on flame structure and combustion dynamics in a lean premixed combustor. In *52nd ASME Turbo Expo Conference*, May 2007. ASME Paper GT2007-27298.

[33] D. M. Wicksall and A. K. Agrawal. Acoustic measurements in a lean premixed combustor operated on hydrogen/hydrocarbon mixtures. *International Journal of Hydrogen Energy*, 32:1103–1112, 2007.

[34] T. Lieuwen, V. McDonell, E. Petersen, and D. Santavicca. Fuel flexibility influences on premixed combustor blowout, flashback, autoignition and stability. *Journal of Engineering for Gas Turbines and Power*, 130(1), 2008.

[35] C. Uykur, P. F. Henshaw, D. S. K. Ting, and R. M. Barron. Effects of addition of electrolysis products on methane/air premixed laminar combustion. *International Journal of Hydrogen Energy*, 26:265–273, 2001.

[36] G. A. Karim, I. Wierzba, and Y. Al-Alousi. Methane–hydrogen mixtures as fuels. *International Journal of Hydrogen Energy*, 21(7):625–631, 1996.

[37] J. L. Gauducheau, B. Denet, and G. Searby. A numerical study of lean CH_4/H_2/air premixed flames at high pressure. *Combustion Science and Technology*, 137:81–99, 1998.

[38] G. S. Jackson, R. Sai, J. M. Plaia, C. M. Boggs, and K. T. Kiger. Influence of H_2 on the response of lean premixed CH_4 flames to high strained flows. *Combustion and Flame*, 132:503–511, 2003.

[39] M. Matalon and B. J. Matkowsky. Flames as gasdynamic discontinuities. *Journal of Fluid Mechanics*, 124:239–259, 1982.

[40] C. K. Law. Dynamics of stretched flames. *Proc. Combust. Inst.*, 22:1381–1402, 1988.

[41] S. M. Candel and T. J Poinsot. Flame stretch and the balance equation for the flame area. *Combustion Science and Technology*, 70:1–15, 1990.

[42] M.C. Janus, G. A. Richards, M. J. Yip, and E. H. Robey. Effects of ambient conditions and fuel composition on combustion stability. In *42nd ASME Turbo Expo Conference*, June 1997. ASME Paper GT97-266.

[43] D. Fritsche, M. Furi, and K. Boulouchos. An experimental investigation of thermoacoustic instabilities in a premixed swirl-stabilized flame. *Combustion and Flame*, 151(1-2):29–36, 2007.

[44] P. J. Langhorne, A. P. Dowling, and N. Hooper. Practical active control system for combustion oscillations. *Journal of Propulsion and Power*, 6(3):324–333, 1990.

[45] K. H. Yu, K. J. Wilson, and K. C. Schadow. Active combustion control in a liquid-fueled dump combustor. In *35th AIAA Aerospace Sciences Meeting*, January 1997. AIAA-97-0462.

[46] C. M. Jones, J. G. Lee, and D. A. Santavicca. Closed-loop active control of combustion instabilities using subharmonic secondary fuel injection. *Journal of Propulsion and Power*, 15(4):584–590, 1999.

[47] S. Sattinger, Neumeier Y, A. Nabi, B .T. Zinn, D. Amos, and D. Darling. Subscale demonstration of the active feedback control of gas-turbine combustion instabilities. *Journal of Enginnering for Gas Turbine and Power*, 122(2):262–268, 2000.

[48] J. M. Cohen, J. H. Stufflebeam, and W. Proscia. The effect of fuel/air mixing on actuation authority in an active combustion instability control system. *Journal of Enginnering for Gas Turbine and Power*, 123(3):537–542, 2001.

[49] A. Wachsman, S. Park, Z. C. Sobhani, A. M. Annaswamy, and A. F. Ghoniem. Simultaneous combustion instability and emissions control using air and fuel

modulation. In *42nd AIAA Aerospace Sciences Meeting*, January 2004. AIAA-2004-0633.

[50] A. J. Riley, S. Park, A. P. Dowling, S. Evesque, and A. M. Annaswamy. Advanced closed-loop control on an atmospheric gaseous lean-premixed combustor. *Journal of Enginnering for Gas Turbine and Power*, 126(4):708–716, 2004.

[51] S. Park, A. Wachsman, A. M. Annaswamy, and A. F. Ghoniem. Experimental study of pod-based control for combustion instability using a linear photodiode array. In *42nd AIAA Aerospace Sciences Meeting*, January 2004. AIAA-2004-0639.

[52] K. R. McManus, U. Vandsburger, and C. T. Bowman. Combustor performance enhancement through direct shear layer excitation. *Combustion and Flame*, 82(1):75–92, 1990.

[53] B. Higgins, M. Q. McQuay, F. Lacas, and S. Candel. An experimental study on the effect of pressure and strain rate on ch chemiluminescence of premixed fuel-lean methane/air flames. *Fuel*, 80:1583–1591, 2001.

[54] H. N. Najm, O. M. Knio, P.H. Paul, and P. S. Wyckoff. A study of flame observables in premixed methane-air flames. *Combustion Science and Technology*, 140:369–403, 1998.

[55] A. F. Ghoniem, S. Park, A. Wachsman, A. M. Annaswamy, D. Wee, and H. M. Altay. Mechanism of combustion dynamics in a backward-facing step stabilized premixed flame. *Proc. Combust. Inst.*, 30:1783–1790, 2005.

[56] A. P. Dowling and S. R. Stow. Acoustic analysis of gas turbine combustors. *Journal of Propulsion and Power*, 19(5):751–764, 2003.

[57] R. L. Speth and A. F. Ghoniem. Using a strained flame model to collapse dynamic mode data in a swirl-stabilized syngas combustor. *Proc. Combust. Inst.*, 32, 2008.

[58] D. G. Goodwin. Cantera: object-oriented software for reactign flows. Technical report. `http://www.cantera.org/`.

[59] Y. M. Marzouk, A. F. Ghoniem, and H. N. Najm. Toward a flame embedding model for turbulent combustion simulation. *AIAA Journal*, 41(4):641–652, 2003.

[60] R. L. Speth, Y. M. Marzouk, and A. F. Ghoniem. Impact of hydrogen addition on flame response to stretch and curvature. In *43rd Aerospace Sciences Meeting*. AIAA, 2005. AIAA-2005-143.

[61] M. V. Petrova and F. A. Williams. A small detailed chemical-kinetic mechanism for hydrocarbon combustion. *Combustion and Flame*, 144(3):526–544, 2006.

[62] R. L. Speth, H. M. Altay, D. E. Hudgins, A. M. Annaswamy, and A. F. Ghoniem. Vortex-driven combustion instabilities in step and swirl-stabilized combustors. In *46th AIAA Aerospace Sciences Meeting*, January 2008. AIAA-2008-1053.

[63] T. C. Lieuwen and V. Yang. *Combustion Instabilities in Gas Turbine Engines: Operational Experience, Fundamental Mechanisms, and Modeling*. AIAA, 2005.

[64] J. H. Uhm and S. Acharya. Control of combustion instability with a high-momentum air-jet. *Combustion and Flame*, 139(1-2):106–125, 2004.

[65] H. M. Altay, R. L. Speth, D. Snarheim, D. E. Hudgins, A. F. Ghoniem, and A. M. Annaswamy. Impact of microjet actuation on stability of a backward-facing step combustor. In *45th AIAA Aerospace Sciences Meeting*, January 2007. AIAA-2007-0563.

[66] J. H. Uhm and S. Acharya. Low-bandwidth open-loop control of combustion instability. *Combustion and Flame*, 142(4):348–363, 2005.

[67] H. M. Altay, R. L. Speth, D. E. Hudgins, and A. F. Ghoniem. Flame-vortex interaction driven combustion dynamics in a backward-facing step combustor. *Combustion and Flame*, 156(5):1111–1125, 2009.

[68] T. Lieuwen, V. McDonnell, E. Petersen, and D. Santavicca. Fuel flexibility influences on premixed combustor blowout, flashback, autoignition and stability. In *51st ASME Turbo Expo Conference*, May 2006. ASME Paper GT2006-90770.

[69] Y. M. Marzouk and A. F. Ghoniem. Vorticity structure and evolution in a transverse jet. *Journal of Fluid Mechanics*, 575:267–305, 2007.

[70] J. H. Uhm and S. Acharya. Role of low-bandwidth open-loop control of combustion instability using a high-momentum air jet - mechanistic details. *Combustion and Flame*, 147(1-2):22–31, 2006.

[71] T. Schuller, S. Ducruix, D. Durox, and S. Candel. Modeling tools for the prediction of premixed flame transfer functions. *Proc. Combust. Inst.*, 29:107–113, 2002.

[72] K. R. A. M. Schreel, R. Rook, and L. P. H. de Goey. The acoustic response of burner-stabilized flat flames. *Proc. Combust. Inst.*, 29:115–122, 2002.

[73] R. B. Price, I. R. Hurle, and T. M. Sugden. *Proc. Combust. Inst.*, 12:1093–1102, 1968.

[74] N. Noiray, D. Durox, T. Schuller, and S. Candel. Self-induced instabilities of premixed flames in a multiple injection configuration. *Combustion and Flame*, 145:435–446, 2006.

[75] A. C. McIntosh and J. F. Clarke. A review of theories currently being used to model steady plane flameson flame-holders. *Combustion Science and Technology*, 37(3-4):201–219, 1984.

[76] G. Joulin and P. Clavin. Linear-stability analysis of non-adiabatic flames: Diffusional-thermal model. *Combustion and Flame*, 35(2):139–153, 1979.

[77] G. M. Abu-Off and R. S. Cant. Reaction rate modeling for premixed turbulent methane-air flames. In *Proceedings of the Joint Meeting of Spanish, Portuguese, Swedish and British Sections of the Combustion Institute*, 1996.

[78] Robert J. Kee, Michael E. Coltrin, and Peter Glarborg. *Chemically reacting flow: theory and practice.* John Wiley and Sons, Inc., 2003.

[79] P. N. Brown, G. D. Byrne, and A. C. Hindmarsh. Vode: a variable-coefficient ode solver. *SIAM Journal of Scientific Computing*, 10(5):1039–1051, 1989.

[80] H. N. Najm and P. S. Wyckoff. Premixed flame response to unsteady strain rate and curvature. *Combustion and Flame*, 110:92–112, 1997.

[81] H. N. Najm, P. S. Wyckoff, and O. M. Knio. A semi-implicit numerical scheme for reacting flow. *Journal of Computational Physics*, 143:381–402, 1998.

[82] G. P. Smith, D. M. Golden, M. Frenklach, N. W. Moriarty, B. Eiteneer, M. Goldenberg, C. T. Bowman, R. K. Hanson, S. Song, Jr. W. C. Gardiner, V. V. Lissianski, and Z. Qin. Gri-mech 3.0. `http://www.me.berkeley.edu/gri_mech/`.

[83] O. M. Knio, H. N. Najm, and P. S. Wyckoff. A semi-implicit numerical scheme for reacting flow, ii. stiff, operator-split formulation. *Journal of Computational Physics*, 154:428–467, 1999.

[84] S. H. Chung and C. K. Law. An invariant derivation of flame stretch. *Combustion and Flame*, 55:123–125, 1984.

[85] T. Echekki and J. H. Ferziger. Studies of curvature effects on laminar premixed flames: Stationary cylindrical flames. *Combustion Science and Technology*, 90:231–252, 1993.

[86] H. M. Altay, S. Park, D. Wu, D. Wee, A. M. Annaswamy, and A. F. Ghoniem. Modeling the dynamic response of a laminar perforated-plate stabilized flame. *Proc. Combust. Inst.*, 32:1359–1366, 2009.